UNIVERSITY OF CALIFORNIA,
IRVINE

Biomedical Applications of Perturbation Monte Carlo Methods

DISSERTATION

submitted in partial satisfaction of the requirements
for the degree of

DOCTOR OF PHILOSOPHY

in Biomedical Engineering

by

Jennifer Nguyen

Dissertation Committee:
Professor Vasan Venugopalan, Chair
Researcher Jerome Spanier
Professor Zoran Nenadic

2017

TABLE OF CONTENTS

List of Figures

List of Tables

ACKNOWLEDGMENTS

First, I would like to express my sincere gratitude to my advisor Prof. Spanier for the continuous support of my Ph.D study and related research, for his patience, motivation, compassion, and immense knowledge. His guidance helped me in all the time of research and writing of this thesis. I could not have imagined having a better advisor and mentor for my Ph.D study. I would also like to thank Prof. Venguopalan and Dr. Carole Hayakawa who pushed me to improve and offered me invaluable guidance and advice.

I would also like to thank the result of my thesis committee, Dr. Nenadic. Thank you for helpful feedback.

My sincere thanks also goes to Dr. Mourant, who provided me this opportunity and for the immense effort and feedback during my first paper. Without her support, this project would not have been possible.

Last but not the least, I would like to thank my family: my mother and grandmother for supporting me spiritually throughout writing this thesis and my life in general.

CURRICULUM VITAE

Jennifer Nguyen

EDUCATION

Master of Science in Biomedical Engineering **2012**
University of California, Irvine *Irvine, California*

Bachelor of Science in Biomedical Engineering **2009**
University of California, Irvine *Irvine, California*

RESEARCH EXPERIENCE

Graduate Research Assistant **2010–2017**
University of California, Irvine *Irvine, California*

TEACHING EXPERIENCE

Teaching Assistant **2014–2015**
University of California, Irvine *Irvine, California*

REFEREED JOURNAL PUBLICATIONS

Perturbation Monte Carlo Methods for tissue structure alterations **2013**
Biomedical Optics Express

Development of perturbation Monte Carlo methods for polarized light transport in a discrete particle **2016**
Biomedical Optics Express

SOFTWARE

pMC-1.2 `\https://bitbucket.org/hayakawa/montecarlo/src/`
Perturbation Monte Carlo method applied to Judith Mourant's tissue scattering model in C++ and Fortran77. Note: to obtain all source files for this code click on the subfolder "Mourant" after going to the listed site.

ABSTRACT OF THE DISSERTATION

Biomedical Applications of Perturbation Monte Carlo Methods

By

Jennifer Nguyen

Doctor of Philosophy in Biomedical Engineering

University of California, Irvine, 2017

Professor Vasan Venugopalan, Chair

This dissertation is an exploration of a new phase function and polarization sensitive perturbation Monte Carlo (pMC) method applied to a realistic tissue scattering model. This project is motivated by the need to improve upon previous methods that screen for early dysplastic tissue changes by optically probing suspicious regions. The majority of early dysplastic changes occur in the epithelial layer of tissue. Common strategies for increasing collection of photons that have probed shallow depths involve using short source-detector separations or using angled detector fibers. Tracking the degree of depolarization is also helpful in differentiating between photons that have probed deeper depths from others that have only probed shallow depths. Conventional Monte Carlo simulations are often employed to solve the Radiative Transport Equation (RTE) and estimate measured signals in problems with short source-detector separations or other atypical optical probe geometries.

In the pMC method, one conventional Monte Carlo simulation is run with baseline optical properties. This results in a database of photon biographies which are then subjected to pMC equations that allow for quick signal estimates to be obtained at perturbed model parameter values, bypassing the need for another conventional Monte Carlo simulation to be run. Doing this eliminates the need to do another Monte Carlo simulation to obtain reflectance estimates at slightly different optical properties. In addition to the increase in computational efficiency, this method has other

advantages that may be useful to researchers interested using optical probes to identify dysplasia such as the ability to track polarization and the ability to account for changes in phase function. This is useful since polarization is employed in several optical probes designed for detection of dysplasia and the polarization state of collected photons is useful in obtaining additional information on the medium and the nature of the light-tissue interactions of collected photons. The ability to account for changes in phase function is also useful since changes in scatterer shape are associated with changes in phase function. Together, this new pMC algorithm is fine-tuned to enable other researchers to model reflectance changes for typical optical probe geometries optimized for detection of dysplasia.

Chapter 1

Introduction

Non-invasive (optical) quantification (or characterization) cell and tissue microstructure is a critical field of research that enables characterization of biological processes such as tumorigenesis and clinical diagnosis of cancer. Although the Papanikolaou Smear (Pap Smear) has long been considered the gold standard procedure for cervical cancer diagnosis, there are a considerable number of practical problems related to this procedure. The Pap Smear involves collection of cells from the cervix followed by staining, creation of a smear of cervical cells, and inspection of the collected cells under microscope. The anatomy of the area of cells to be sampled means that consistent and reliable sampling is not guaranteed. Furthermore, colposcopically normal-appearing regions of tissue may contain abnormal high-grade squamous intraepithelial lesions (HSILs). A possible solution would be to take biopsies at several random locations, however this would increase patient discomfort considerably while maintaining a low yield of HSILs.

Optical biopsy techniques, which utilize knowledge of tissue optical properties and non-ionizing light to enable the operator to identify suspicious lesions, provide significant advantages over the Pap Smear procedure. First, optical biopsy methods are non-invasive and utilize non-ionizing radiation. This means that measurements can be repeated as many times as needed without increasing

the risk of exposure or increasing patient discomfort. Second, these techniques may reduce the complexity of measurement which can allow for a quick turnaround for a diagnosis. After a Pap Smear, patients are required to return for a follow-up examinations and treatments; up to 70% of inner city patients fail to return for the follow-up examination, so simplification of the screening process can lead to improvements in patient care outcomes. Finally, these techniques allow for quantification of both *in vivo* and *in vitro* biological samples, which enables a clinican to obtain accurate information on a region of interest in the tissue in its pristine state.

Many groups have worked towards improving the optical biopsy to increase its adoption in clinical practices. The Backman group developed the method of partial wave spectroscopy (PWS), which provides insights into the statistical properties of the nanoscale architecture of biological cells beyond what conventional microscopy, whose resolution is limited by diffraction of light, can resolve [32]. PWS couples light transport theory with detection of back-scattered light from a focused wave of broadband low-spatially coherent light. A statistical parameter L_d, which has been shown to have high correlation to areas with suspicious lesions, is calculated from the image of the backscattered light at each group of pixels. Backman's group has tested this technique on *in vitro* samples of colon, pancreas, and lung cells [33] as well as *in vivo* samples [9] and showed that their constructed statistical parameter was significantly higher in tissue regions with cancerous lesions. Backman has also developed a polarization-sensitive technique to differentiate between photons of greater depth penetration (> 200 μm) and shallow depth penetration (~ 100 - 150 μm) [10].

Wax's group has developed a method that uses angle-resolved scattering interferometric measurements to resolve the size and shape of scatterers. This method has been tested in a polydimethylsiloxane and polystyrene optical sample [36] and demonstrated in an *in vivo* study focused on diagnosis of Barrett's Esophagus [34]. Sokolov's group has developed a method that combines detection of polarized light with angular and distal resolution to determine scatterer size characteristics of size-dependent scattering at a specific depth within the epithelium. Analysis of the

scattering signal by use of Mie theory allows the extraction of scatterer size and key size distribution parameters for precancer detection.

The project that is discussed here is the result of a collaboration with Judith Mourant of Los Alamos National Labs, a researcher interested detecting changes in subcellular microstructure related to dysplasia and correlating those to changes in reflectance/transmittance spectra. Like other researchers in this field, she has employed probe geometries with small source-detector separation, angled probe fibers, and employed light polarization in order to better characterize cellular microstructures and their reflectance signatures [21, 22, 19]. The use of these exotic probe geometries precludes the use of the Standard Diffusion Approximation and other computationally inexpensive methods for modeling light-tissue interactions due to the short source-detector separations involved and the asymmetrical geometry caused by the angled detector fibers. Because of this, Mourant's and other groups in this field have traditionally employed conventional Monte Carlo methods in order to properly model light tissue interactions at this length scale [21, 18, 10, 24], a computationally expensive task. The motivation for this project is to develop an algorithm that is computationally efficient, accurate, and with useful features for other researchers in this field.

1.1 Objectives

In order to address the need for a computationally efficient yet accurate method of estimating reflectance, we introduce a novel method that applies perturbation Monte Carlo methods to the problem of predicting changes in reflectance measurements given changes in medium or tissue optical properties. The perturbation Monte Carlo (pMC) method is well-established and has been applied to a wide range of biomedical optics problems including: determination of layered tissue optical properties [11, 29], tissue image reconstruction [35], optical tomography [15], and time-resolved functional imaging [6, 7]. There are several features that are unique to the author's implementation of the pMC method, which may be useful to researchers interested in probing changes microarchi-

tectural changes in tissue. First, this implementation of the pMC method is the first to be intimately connected to subcellular microstructure and the concentrations of groups of scatterers in cells. Previous implementations of pMC have traditionally used bulk optical properties of the medium as input parameters. The pMC method discussed in this dissertation is therefore capable of providing insights into the light scattering mechanisms behind reflectance changes due to dysplasia or other cellular processes. Second, the author's implementation of perturbation Monte Carlo method is the first pMC method that accounts for phase function differences as well as the first that allows for the use of polarized light. The addition of polarization tracking and accounting of phase function alterations can be useful for researchers interested in detecting dysplasia since changes in scatterer sizes in tissue lead to changes in the phase function and/or changes in how the scatterers interact with polarized light. Finally, the pMC method in this dissertation is formulated generally. This means that other phase functions (e.g. Mie, T-matrix, Henyey-Greenstein) of interest can be employed. Together, these unique features of this dissertation's pMC method provide a compelling package for researchers interested in modeling dysplastic tissue changes, although there may be many more applications that can benefit from the use of pMC.

1.2 Chapter Breakdown of Thesis

In chapter 2, the link between the solution to the radiative transport equation, conventional Monte Carlo simulations, and the perturbation Monte Carlo method is explained. The scattering model that describes distributions of scatterers present in tissue is also discussed as well as our treatment of light polarization.

Chapter 3 of this thesis focuses on comparisons that were made between conventional Monte Carlo and perturbation Monte Carlo predictions of reflectance. A standard for computational efficiency is used to assess the computational gains made by perturbation Monte Carlo in estimates of reflectance. We also discuss the limitations of the perturbation Monte Carlo method.

Chapter 4 of this thesis then focuses on our development of the differential Monte Carlo (dMC) method to this problem. In order to test out dMC's capabilities, we did a comparison between finite difference methods for estimating the sensitivity of reflectance to parameters of interest, that we call d-cMC, and dMC. We assess the limitations of the dMC method as well as determine factors that affect dMC's efficiency and the variance of its estimates.

Using the dMC estimates of sensitivity to guide our analysis, we then test dMC performance in an inverse problem-solving setting in Chapter 5. Inverse problem solving, in this dissertation, is defined as determining the values of certain parameters of interest (in our case, the mean radii and number density of scatterer distributions) from a given set of measurements. We test the method's capabilities to optimize parameters given unpolarized reflectance measurements and polarized reflectance measurements. Our measurement set up is modeled after real life measurements performed by our collaborator at Los Alamos National Labs. We also explore limitations of our method in terms of parameter optimization.

Chapter 2

Problem Definition and Perturbation Monte Carlo Formulation

2.1 Light scattering model

We develop a perturbation Monte Carlo (pMC) computational framework for a tissue representation that models optical scattering using three log-normal distributions to represent the polydispersity of the scattering medium[25, 18, 2, 27]. The pMC method introduced here can accommodate any number (m) of scatterer groups with arbitrary distributions of scatterer size. The total scattering coefficient of the ith distribution, $\mu_{s,i}$, is calculated using $\mu_{s,i} = \int Q_{scat}(t) N_{a,i}(t) L_i(\bar{r}_i, t) dt$ where Q_{scat} is the scattering efficiency, $N_{a,i}$ is the product of number density and the scattering cross-section of the particle, t is a particle radius, and L_i is the ith log-normal distribution characterized by its mean radius $\bar{r}_i$ and standard deviation, σ_i: $L_i(\bar{r}_i, t) = \exp\left\{-(\ln t - \ln \bar{r}_i)^2/(2\sigma_i^2)\right\}/(t\sigma_i\sqrt{2\pi})$. The scattering coefficient of the medium $\bar{\mu}_s$ can be calculated by summing the contribution of each distribution to the scattering coefficient $\bar{\mu}_s = \sum_{i=1}^{m} \mu_{s,i}$ [28]. The phase function of each scatterer population is calculated by integrating across radius values and using the log-normal distribution to

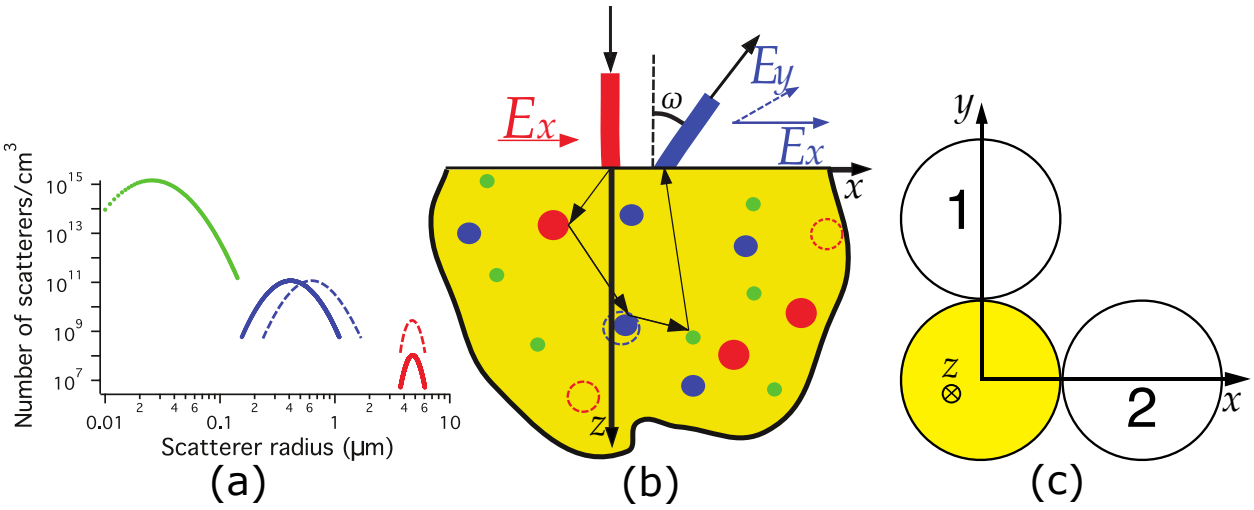

Figure 2.1: A conceptual diagram of the pMC application to the light scattering model used in this study. (a) Depiction of the light scattering model composed of three distinct distributions of scatterers. The dotted blue and red plots represent perturbations in mean radius and number density while solid green, blue and red plots represent "baseline" parameter values. (b) A schematic diagram of the source-detector configuration. (c) The top-down view of the probe. The yellow circle represents the source and the circles with numbers inside represent the two detectors. See Section 2.2 for probe details.

properly weight the phase functions that Mie Theory provides: $f_i(\theta) = \frac{1}{\mu_{s,i}} \int f_{Mie}(t,\theta) Q_{scat}(t) N_{a,i}(t) dt$ where f_i is the phase function of the ith distribution of scatterers, f_{Mie} is the phase function of a mono-dispersed distribution of scatterers, and θ is the scattering angle. We approximate these integrals for $\mu_{s,i}$ and f_i using trapezoid rule integration with uniform grid spacing with the width of the bin set at 0.001 μm for all three distributions.

Table 2.1 provides scattering parameters that approximate the contributions of protein complexes, organelles, and nuclei present in epithelial cervical tissues based on previous experimental results [18, 25]. These parameter values serve as baseline values in the pMC results presented in this dissertation and are meant to model a class of problems (similar to the problem in [25]) in which pMC application could potentially benefit forward and inverse radiative transport solutions.

Table 2.1: Distributions of scatter sizes in the tissue model

i	Average Size, $\bar{r}_i \pm \sigma$ (μm)	Number Density, $N_{s,i}$ (cm^{-3})	n_{medium}	$n_{scatterer}$
1	0.03 ± 0.4	4×10^{13}	1.33	1.46
2	0.45 ± 0.3	5×10^{10}	1.35	1.40
3	4.8 ± 0.1	5×10^{7}	1.37	1.49

2.2 Measurement geometry

In this study we consider a probe with two detectors placed equidistant from a central source fiber which detects either unpolarized or polarized reflectance. A probe schematic is shown in Fig. 2.1(c). All detector fibers are angled at $\omega = 20^\circ$ relative to the outward pointing surface normal and towards the source fiber. The distance from the center of any detector fiber to the center of the source fiber is 550 μm and all the fibers are 480 μm in diameter. All fibers have a light cone detection half angle of 21.7°. The close source-detector separation and the angling of the detector fibers towards the source fibers promotes photon trajectories that interact with scatterers located at shallow depths.

2.3 The Connection Between the RTE and Monte Carlo Simulations

In this section, we provide a brief exposition of several topics that establish a rigorous foundation for the methods of this dissertation. A comprehensive discussion of this material can be found in Section 3.3 of [31]. In biophotonics problems, the Radiative Transport Equation (RTE) is commonly used to describe interactions of light with tissue. Derivation of pMC equations requires an understanding of the equivalence between the equation-based analytic model that describes the physics and the probabilistic model that describes how to generate photon random walks and uses

them to estimate the measurements desired.

Our initial objective is to connect the analytic/physical model that describes light transport in tissue with the stochastic simulation model on which Monte Carlo methods are based. The time-independent Radiative Transport Equation (RTE) is used to describe the interaction of unpolarized light with tissue: We begin with the time-independent integro-differential form of the RTE:

$$\nabla\Phi(r,\omega)\cdot\omega = -\mu_t\Phi(r,\omega) + \mu_s\int_{4\pi}\Phi(r,\omega')f(r',\omega'\rightarrow\omega)d\omega' + Q(r,\omega) \tag{2.1}$$

where Φ is the photon radiance (*#/area/sr*), r is position, ω is a unit direction vector, μ_t is the optical interaction coefficient, μ_s is the optical scattering coefficient, f is the single-scattering phase function that scatters photons from ω' to ω at r', and Q is the volumetric source.

It is useful to convert the integro-differential RTE to the integral equation form when setting up for the Monte Carlo (probabilistic) mode. The integral equation for the particle collision density is [31]:

$$\Psi(P) = \int_{\Gamma}K(P,P')\Psi(P')dP' + S(P) \tag{2.2}$$

where $P = (r,\omega)$ is a point in the phase space Γ and the collision density is:

$$\Psi(r,\omega) = \mu_t(r)\Phi(r,\omega) \tag{2.3}$$

The kernel, K, describes both the positional and directional changes involved in scattering and transporting photons at r' with direction ω' to r with direction ω. It is composed of the probability density for scattering from ω' to ω, $f(\omega'\cdot\omega)$, the probability $\mu_s(r\prime)/\mu_t(r\prime)$ of scattering (rather than absorption) at r', and the transport kernel T.

$$K(r',\omega'\rightarrow r,\omega) = f(\omega'\cdot\omega)\frac{\mu_s(r')}{\mu_t(r')}T(r'\rightarrow r,\omega') \tag{2.4}$$

The transport kernel, T, in Eq. (2.4) describes transport of photons in the direction ω' from r' to r:

.

$$T(r' \to r, \omega) = \mu_t(r') \exp\left[-\int_0^{\omega' \cdot ||r-r'||} \mu_t(r' + s\omega')ds\right] \tag{2.5}$$

This formula for T allows for the optical coefficient, μ_t, to depend continuously along the path from r' to r, but if μ_t is regionwise constant, the integrals in the exponent simplify to $d \times \mu_t$, where d is the distance from r' to r. The function S is the density of first collisions and Eq. (2.6) shows that S is obtained by transporting each photon along its initial direction ω from the physical source Q to its collision location r:

$$S(r, \omega) = \int T(r' \to r, \omega) Q(r', \omega) dr'. \tag{2.6}$$

Researchers are often interested in the reflectance or transmittance rather than the full RTE solution; this can be expressed as the integral:

$$I = \int_\Gamma g(P)\Psi(P)dP \tag{2.7}$$

where g is a "detector function" that describes the spatial locations and the unit direction vectors that characterize the physical detector, including its numerical aperture. For fiber-optic detectors placed on the tissue surface at D :

$$g(P) = \int_\Gamma |\omega \cdot \omega_n| \, \Xi_D(r) \Xi_{N(D)}(\omega) dr d\omega \tag{2.8}$$

where P is a particle state characterized by the particle's position and direction $P = (r, \omega)$ and ω_n is the unit outward normal vector on D. The Ξ functions are indicator functions that restrict the integration to $r \in D$ and $\omega \in N(D)$, the numerical aperture of the detector, respectively. Together, Eqs. (2.2) – (2.7) form the analytic model of the problem.

2.4 Random Walk Processes and Monte Carlo Methods

Monte Carlo methods constitute a broad class of algorithms that are characterized by the property that they all involve drawing random samples from probability distributions. Statistical data are collected from these samples and used to draw inferences about one or more problems under investigation. These problems may arise from a naturally stochastic process (as in the case of photon transport through tissue) or not. Some examples of problems whose formulations are completely deterministic are: 1. solve the matrix equation $Ax = b$ where A is an $n \times n$ matrix, b is a known n-vector; 2. estimate the value of the integral $I = \int_V f(x)dx$ where $f(x)$ is a known function of s variables and V is a volume in $\mathbb{R}^s$.

Our interest here is only in the naturally stochastic case of the interaction of light with tissue, as described by the Eqs. $(2.2) - (2.7)$. In fact, the prototype problem here is to estimate the value of the integral I in Eq. (2.7), where the detector function g is known but the function Ψ is only known to satisfy the transport equation (2.2). To this end we now describe the stochastic, or probabilistic model needed to address such problems. For us, such a model will arise through a *random walk process.*

2.4.1 Random Walk Processes and Model Equivalence

A *random walk process* provides the probability density functions that are used to launch photon biographies, transport them from position to position and from one unit direction to another, and terminate them. We define a random walk process using two sets of functions: $\{f_n, p_n\}$. The function $f_n(P_1, ..., P_n)$ is the probability density of a random walk chain with the steps $(P_1, P_2, ..., P_n)$; f_1 can also be thought of as a source function. $p_n(P_1, ..., P_n)$ is the probability of terminating the chain. The simplest such random walk process is the one that mimics the microscopic laws that are implicit in the coefficients of the RTE (Eq. (2.2)): we call this the *analog random walk* process.

The functions $\{f_n, p_n\}$ that characterize the analog random walk process are:

$$f_1(P) = \frac{S(P)}{\int_\Gamma S(P')dP'} \tag{2.9}$$

$$f_n(P_1,...,P_n) = \Pi_{i=2}^{n}\left[\frac{K(P_i,P_{i-1})}{\int_\Gamma K((P_i,P_{i-1})dP_i}\right] S(P_1) \quad n \geq 2 \tag{2.10}$$

and

$$p_n(P_1,...,P_n) = p(P_n) = \mu_a(P_n)/\mu_t(P_n) \tag{2.11}$$

We see that the analog random walk process makes use of a normalized version of the source function S (Eq. (2.6)) to identify the first collision point. At each collision point $P = (r,\omega)$ it decides between absorption (with probability $\mu_a(r)/\mu_t(r)$), and scattering (with probability $\mu_s(r)/\mu_t(r)$). In the event of scattering at a collision point, a new direction is selected from the pdf f and the biography continues to a next collision making use of the transport kernel, T (Eq. (2.5)). This process of alternately generating new collision locations, r, and new unit directions ω continues until each biography terminates, either by absorption at some location or by permanently exiting the physical region of interest. We introduce the sample space, B, whose elelements describe each possible photon biography, from "birth" to termination, either by absorption or by escaping the region of interest permanently. It can be shown [30] that every random walk process induces a probability measure M on the space B of all photon biographies $b \in B$. The space B has a very useful decomposition:

$$\mathcal{B} = \cup_{k=1}^{\infty}\Lambda_k + \overline{\Lambda}_\infty \tag{2.12}$$

where Λ_k is the set of all histories that terminate after k collisions. Provided that the linear integral operator $\mathcal{K}$ is contractive ($\|\mathcal{K}\|_1 = \sup_{\|\Psi\|_1 \neq 0} \frac{\|\mathcal{K}\Psi\|_1}{\|\Psi\|_1} < 1$), it can be shown [31] that $M(\lambda_\infty) = 0$. So that:

$$\sum_{k=1}^{\infty} M(\Lambda_k) = 1. \tag{2.13}$$

where

$$M(\Lambda_k) = \int_\Gamma ... \int_\Gamma f_k(P_1, ..., P_k) \prod_{i=1}^{k-1} q_i(P_1, ..., P_i) p_k(P_1, ..., P_k) dP_1 ... dP_k \tag{2.14}$$

and where q_i is defined as 1-p_i. There are several random walk processes that one may choose from including: continuous absorption weighting, discrete absorption weighting, analog random walk process. One may choose one random walk process over the other to obtain lower variance estimates of I, and/or shorter simulation run times. More information on the various random walk processes can be found in [14]. All the numerical experiments shown in this dissertation use continuous absorption weighting, so we will discuss this in detail next. For continuous absorption weighting,

$$f_1(P) = \frac{S(P)}{\int_\Gamma S(P_1) dP_1} \tag{2.15}$$

$$f_n(P_1, ..., P_n) = \prod_{l=1}^{n-1} \left[\frac{K(P_l, P_{l+1})}{exp\left[-\int_{P_l}^{P_{l+1}} \mu_a(s) ds \right]} \right] \tag{2.16}$$

$$p_n(P_1, ..., P_n) = p(P_n) = 0. \tag{2.17}$$

These equations indicate that each photon is treated as a packet of photons and is assigned an initial weight W=1. To account for absorption, this packet is continuously de-weighted by a factor of $exp\left[-\int_{P_l}^{P_{l+1}} \mu_a(s) ds \right]$ along its trajectory; absorption in continuous absorption weighting is forbidden. Continuous absorption weighting can also be interpreted as an application of Beer's Law to a packet of photons. Eq. (2.13) means that the number of collisions is finite with probability 1 and

that calculations of infinite sums arising from the RTE converge. One such infinite sum that plays a critical role in the theoretical analysis of RTE's is the Neumann Series. In order to estimate the integral

$$I = \int_{\Gamma} g(P)\Psi(P)dP \tag{2.18}$$

where g is a "detector function" that describes the spatial locations and the unit direction vectors that characterize the physical detector, including its numerical aperture. For fiber-optic detectors placed on the tissue surface at D :

$$g(P) = \int_{\Gamma} |\omega \cdot \omega_n| \, \Xi_D(r)\Xi_{N(D)}(\omega)drd\omega \tag{2.19}$$

where P is a particle state characterized by the particle's position and direction $P = (r, \omega)$ and ω_n is the unit outward normal vector on D. The Ξ functions are indicator functions that restrict the integration to $r \in D$ and $\omega \in N(D)$, the numerical aperture of the detector, respectively. Together, Eqs. (2.2) – (2.7) form the analytic model of the problem. The probability model consists of three elements: the sample space, B, the probability measure M induced on B by the random walk process $\{f_n, p_n\}$, and a random variable $\xi : B \to R$. This random variable designates the contribution of every $b \in B$ to the estimate of the integral (2.7). This contribution is commonly referred to as the *tally*, or *score* associated with b. In the cases for which each biography b has a weight, its tally is often taken as this weight. An example of a useful random variable is the binomial estimator, ξ whose value on the photon biographies, $b \in \mathcal{B}$, is:

$$\xi(b) = \begin{cases} 1 \text{ if } b \text{ results in a detected photon} \\ 0 \text{ otherwise} \end{cases} \tag{2.20}$$

For these analog choices of the measure M and unbiased estimator, ξ, it is intuitively clear (and rigorously shown in [31]) that

$$I = \int_{\Gamma} g(P)\Psi(P)dP = \int_{\mathcal{B}} \xi dM. \tag{2.21}$$

The importance of Eq. (2.21) is that it establishes the equivalence of the analytic model, Eqs. (2.2) – (2.7), and the probabilistic model ($\mathcal{B}$, M, ξ). Eq. (2.21) may also be written

$$I = \lim_{k\to\infty} \frac{1}{N} \sum_{i=1}^{N} \xi(C_i) dM(C_i) = \int_{\mathcal{B}} \xi dM \tag{2.22}$$

where N the number of photon biographies that are generated. Using the expected value operator E, we re-write the above equation as:

$$I = E\left[\xi\right] = \int_{\mathcal{B}} \xi dM \tag{2.23}$$

where M is the probability measure induced by the random walk process and $\mathcal{B}$ is the sample space of all photon biographies

2.5 Perturbation Monte Carlo

The primrary idea behind perturbation Monte Carlo, pMC, is to generate a single set of photon biographies according to the probability measure M and then define a new estimator that can be used to estimate collected light intensity *using the same photon biographies* for different (perturbed) conditions. For the perturbed conditions, Eq. (2.22) becomes Eq. (2.24)

$$\widehat{I} = \lim_{k\to\infty} \frac{1}{N} \sum_{i=1}^{N} \xi(C_i) d\widehat{M}(C_i) = \int \xi d\widehat{M} \tag{2.24}$$

A new estimator, $\widehat{\xi}(b_i)$ is then defined by

$$\widehat{\xi}(bf) = \xi(b)\frac{\widehat{dM}(b)}{dM(b)} \tag{2.25}$$

provided that the Radon-Nikodym derivative exists. This means that sets of M measure 0 also have $\widehat{M}$ measure 0. Then

$$\widehat{I} = \lim_{N\to\infty}\frac{1}{N}\sum_{i=1}^{N}\widehat{\xi}(C_i)d\widehat{M}(C_i) = \int \xi\frac{d\widehat{M}}{dM}dM \tag{2.26}$$

The interpretation of (2.24) is that the expected value of $\widehat{\xi}$ with respect to the baseline measure M is identical to the expected value of the original variable ξ with respect to the modified measure $\widehat{M}$., i.e. $\widehat{I} = I$. It should also be noted that the quantity $\frac{d\widehat{M}}{dM}$ is the Radon-Nikodym derivative. Here, the application of the Radon-Nikodym theorem allows us to reweight the tally ξ in such a way that we move from the model (ξ, M) to the equivalent model ($\widehat{\xi}$ $\widehat{M}$). Here we want to draw attention to the benefits of using pMC to estimate detection in a physical system that has been perturbed - for example cancerous tissue or precancerous tissue. The conventional way to do this is to generate a new set of photon biographies in the system partially or entirely of tumor. Since the sampling functions depend on the optical properties, the measure $\widehat{M}$ that is used to generate the biographies in the tumorogenic system is different from the measure M used to generate the biographies in the homogeneous system. If one is interested in estimating the detection in a family M_α of such perturbed tissue systems one would need to generate a different set of biographies for each member of the family. Calculating the photon trajectories for each precancerous and cancerous condition could be a prohibitively costly process. Instead, with pMC a single set of biographies is generated using the baseline measure M, and for each tumor condition the pMC estimator in Eq. (2.25) is used to estimate the collected intensity, Eq. (2.26). The measure, M, is composed of the source term multiplied by a kernel term for every collision, i.e. $S(P_1)K(P_1 \to P_2)K(P_2 \to P_3)...$ When the source does not change, Eq. (2.27) holds, where j is the number of collisions undergone by a

collected photon.

$$\frac{\widehat{M}_\alpha}{M} = \left(\frac{\widehat{K}_\alpha}{K}\right)^j \tag{2.27}$$

For example, if M is the analog measure based on generating photon biographies by using the source S and the kernel K, the simplest random variable ξ to use is the binomial estimator defined in Eq. (2.20) that tallies 1 for every random walk w that is detected and 0 for all random walks that are not. The transformation (2.20) can be thought of as reweighting of the tally for each random walk w by multiplying the binomial baseline estimator, ξ, by $\frac{d\widehat{M}_\alpha}{dM}$. This means assigning an altered weight when the analog random walk leads to detection, and 0 otherwise. $\frac{dM_\alpha}{dM}$ is easily calculated using the source S_α and kernel K_α that characterize the measure M_α :

$$\xi_\alpha = \xi\frac{dM_\alpha}{dM} = \begin{cases} \frac{S_\alpha}{S}\prod_{l=1}^{j}\frac{K_\alpha}{K} & \text{if random walk leads to detection} \\ 0 & \text{otherwise} \end{cases} \tag{2.28}$$

This reweighting can be performed by a postprocessing algorithm that is quite inexpensive compared to the cost of generating different photon biographies for each set of tissue conditions. Explicit formulas will be given in the next two sections that make these ideas concrete.

2.5.1 Distribution Selection Scattering Method vs. Composite Phase Function Scattering Method

For the studies shown in this dissertation, we developed two different methods to simulate the phenomenon of scattering. These two methods of simulating scattering have different likelihood functions and ultimately produce different estimators for the perturbed weight and sensitivity. One of the scattering methods is called the Distribution Selection Scattering Method. In this method, each photon only interacts with a single distribution of scatterers at each interaction. The probability of interacting with the ith scatterer population is proportional to that distribution's contribution

to the scattering coefficient, i.e., $P(Y = i) = \mu_{s,i}/\overline{\mu}_s$, where Y is a random variable that selects the population for the scattering event. Given that the ith scatterer population is selected, the phase function of the ith scattering distribution, f_i, is then sampled for a scattering angle. A composite scattering phase function is not constructed in this method. In the Composite Phase Function Scattering Method, an overall phase function is constructed by calculating the weighted average of the phase functions of each scatterer population, where the weights are based on each distribution's contribution to the scattering coefficient

$$\overline{f} = \sum_{i=1}^{m} \frac{\mu_{s,i}}{\overline{\mu}_s} f_i \tag{2.29}$$

where $\overline{f}$ is the composite phase function, f_i is the phase function of the ith distribution, $\mu_{s,i}$ is ith scatterer distribution's contribution to the scattering coefficient and $\overline{\mu}_s$ is the scattering coefficient of the entire medium and is the sum of the scattering coefficient contributions of all distributions. This composite phase function is then sampled for scattering angles. While these two scattering methods produce equivalent distributions of azimuthal scattering angles (as shown in the appendix), the advantage of the distribution selection scattering method is that the calculations involved with differential Monte Carlo are much simpler to execute. More detailed arguments for using one scattering method over another scattering method are shown in the Appendix.

2.5.2 Perturbation Monte Carlo Method and Distribution Selection Scattering Method

In pMC, a set of photon biographies is generated by making use of the random walk process that is designated for this purpose. As we explained in Section 2.2, a baseline set of Monte Carlo biographies is a dataset consisting of the locations and unit incoming directions of each biography at every collision point. The biography weights arriving at each collision point are also saved. The probability measure, M_{CAW}, on the space $\mathcal{B}$ of biographies is induced by the probability density

functions that launch photons, transport them from collision to collision, and terminate them by eventual exit from the tissue volume of interest. The biography weights account for the use of the intercollision density. This measure is composed of the source term multiplied by the RTE kernel inside the medium. In turn, the transport kernel is comprised of a product of the probability of scattering, the phase function, and the intercollision density function. In the application of pMC, each collision in the medium is reweighted at each scattering event to account for a change in the medium's optical parameters

$$\widehat{\xi} = \xi \frac{\widehat{M}(\beta)}{M(\beta)}. \tag{2.30}$$

Here $\widehat{\xi}$ is the perturbed weight, ξ, is the estimator or photon weight, $\widehat{M}(\beta)$ is the perturbed probability measure on biography β and $M(\beta)$ is the unperturbed probability measure on that same biography. All hatted quantities in this paper are the perturbed versions of the unhatted quantities.

$$\frac{\widehat{M}(\beta_n)}{M(\beta_n)} = \frac{\widehat{T}}{T} \prod_{l=1}^{j} \frac{\widehat{K}_l}{K_l} \tag{2.31}$$

Here, K_l is the RTE kernel at the lth interaction with the medium, T is the transport kernel, and ξ is an estimator which is typically associated with photon weight. The continuous absorption weighting (CAW) random walk process is employed in all MC simulations in this study. In continuous absorption weighting, photon termination by way of absorption is forbidden, the photon is deweighted by the factor $\exp(-\mu_a s)$, and intercollision distances are sampled from $\overline{\mu}_s \exp(-\overline{\mu}_s s)$ where s is the pathlength between one collision and the next. As stated in a previous section, a special scattering algorithm is employed in conjunction with CAW; the photon has a probability of $\frac{\mu_{s,i}}{\overline{\mu}_s}$ to interact with particles of the ith scattering distribution. Modifying the RTE kernel for CAW from [14] to account for our new scattering algorithm, we obtain the RTE kernel

$$K = \frac{\mu_{s,i}}{\overline{\mu}_s} f_i(\omega' \to \omega) \exp(-\mu_a s) \overline{\mu}_s \exp(-\overline{\mu}_s s) \tag{2.32}$$

Combining (2.30), (2.31), and (2.32), produces

$$\widehat{\xi} = \xi \left(\frac{\widehat{\mu}_{s,1}}{\mu_{s,1}}\right)^{j_1} \left(\frac{\widehat{\mu}_{s,2}}{\mu_{s,2}}\right)^{j_2} ... \left(\frac{\widehat{\mu}_{s,m}}{\mu_{s,m}}\right)^{j_m} \exp\left[-(\widehat{\overline{\mu}}_s - \overline{\mu}_s)L\right] \exp\left[-(\widehat{\mu}_a - \mu_a)L\right] \prod_{l_1=1}^{j_1} \frac{\widehat{f}_{l_1}}{f_{l_1}} \prod_{l_2=1}^{j_2} \frac{\widehat{f}_{l_2}}{f_{l_2}} ... \prod_{l_m=1}^{j_m} \frac{\widehat{f}_{lm}}{f_{l_m}} \quad (2.33)$$

where j_1 is the total number of collisions experienced by the photon with respect to the first scattering distribution, j_2 is the total number of collisions experienced by the photon with respect to the second scattering distribution, and so on... j_m is the total number of collisions experienced by the photon with respect to the last (the mth) scattering distribution of the light scattering model and L is the total pathlength travelled by the photon in the medium.

2.5.3 Perturbation Monte Carlo Method and Composite Phase Function Scattering Method

In application of pMC to simulations that involve the Composite Phase Function scattering method, both the scattering coefficient and the phase function are perturbed. So, the corresponding K and $\widehat{K}$ are:

$$K = f(\omega' \to \omega)\mu_s \exp(-\mu_t l) \quad (2.34)$$

$$\widehat{K} = \widehat{f}(\omega' \to \omega)\widehat{\mu}_s \exp(-\widehat{\mu}_t l) \quad (2.35)$$

Using Eqs. 2.26 and 2.27, the following estimator for the perturbed weight is derived:

$$\widehat{\xi} = \xi \left(\frac{\widehat{\mu}_s}{\mu_s}\right)^{j+1} \exp\left[-\left(\widehat{\mu}_t - \mu_t\right) L\right] \prod_{l=0}^{j} \left(\frac{\widehat{\overline{f}_l}}{\overline{f}_l}\right) \quad (2.36)$$

where j is the number of collisions inside the medium, L is the total pathlength and $\widehat{f}$ is the perturbed phase function. The phase functions, f and $\widehat{f}$ are functions of scattering angles θ and ϕ. The exponent, $j+1$, accounts for the fact that the initial entrance into the medium is governed by the transport kernel and by the probability of scattering rather than absorption $\mu_s(r')/\mu_t(r')$. Eq. (2.36) is correct for transport within the medium. However, when the last step is partly out of the scattering medium, then Eq. (2.36) must be modified. The very last step of a photon transport Monte Carlo simulation is different than the others in that the photon does not go from a point to the detector surface, but rather from a point to any point on or *inside* the detector. Therefore the transport kernel must be modified by a term, L_s, the distance from last scattering event in the medium to the detector. Consequently, Eq. (2.36) becomes Eq. (2.37) where L is the distance traveled from an entrance point on the scattering medium surface to an exit point on the scattering medium surface.

$$\widehat{\xi} = \xi \left(\frac{\widehat{\mu}_s}{\mu_s}\right)^j \exp\left[-\left(\widehat{\mu}_t - \mu_t\right) L\right] \prod_{l=0}^{j} \left(\frac{\widehat{f}_l}{f_l}\right) \tag{2.37}$$

2.6 Polarization

This section outlines the necessary steps in accounting for polarization changes in a per photon basis during our conventional Monte Carlo simulations. Polarization is handled in our simulations using the stokes vector method. Polarized light transport is based on [1]. The polarization of the photon is specified by a Stokes vector.

$$\begin{bmatrix} S_0 \\ S_1 \\ S_2 \\ S_3 \end{bmatrix} \tag{2.38}$$

The local coordinate system in which the Stoke's vector is defined, is defined by the three vectors, *u prel*, and *b*. These vectors are immediately rotated so that u points along the direction of the photon entry. For a scattering event, defined by angles θ and ψ, the Stokes vector must first be rotated into the scattering plane:

$$\begin{bmatrix} S_{0s} \\ S_{1s} \\ S_{2s} \\ S_{3s} \end{bmatrix} = \begin{bmatrix} 1 & 0 & 0 & 0 \\ 0 & cos(2\Psi) & sin(2\Psi) & 0 \\ 0 & -sin(2\Psi) & cos(2\Psi) & 0 \\ 0 & 0 & 0 & 1 \end{bmatrix} \begin{bmatrix} S_0 \\ S_1 \\ S_2 \\ S_3 \end{bmatrix} \tag{2.39}$$

where ψ is the angle of rotation. After a scattering event defined by scattering angles θ and ψ, the new direction of photon travel in the reference frame defined by *u*, *b*, *p* is:

$$\begin{aligned} u'_b &= sin(\theta)sin(\Psi) \\ u'_p &= -sin(\theta)cos(\Psi) \\ u'_u &= cos(\theta) \end{aligned} \tag{2.40}$$

New *p* and *b* vectors are also calculated. First a rotation through ψ is performed which makes b' perpendicular to the scattering plane. Finally the axes are rotated through θ, which results in

$$\begin{aligned} p'_b &= -cos(\theta)sin(\Psi) \\ p'_p &= cos(\theta)cos(\Psi) \\ p'_u &= sin(\theta) \end{aligned} \tag{2.41}$$

The axes are then rotated through θ which results in:

$$\begin{aligned} b'_b &= cos(\Psi) \\ b'_p &= sin(\Psi) \\ b'_u &= 0 \end{aligned} \tag{2.42}$$

Finally, the vectors b', p' and u' must now be transformed to the Monte Carlo coordinate system. For example:

$$\begin{aligned} u'_x &= u'_b b_x + u'_p p_x + u'_u u_x \\ u'_y &= u'_b b_y + u'_p p_y + u'_u u_y \\ u'_z &= u'_b b_z + u'_p p_z + u'_u u_z \end{aligned} \tag{2.43}$$

2.6.1 Phase Function Evaluations used by Perturbation Monte Carlo

For photon collection, three rotations are needed. First rotate through an angle psi so that b is in the x-y plane. For pMC phase function evaluations during on photon biographies that followed polarized light transport, we followed Ramella-Roman's method of evaluating the phase function:

$$f(\theta) = s_{11}(\theta). \tag{2.44}$$

For the polarized phase function:

$$f(\theta, \psi) = s_{11}(\theta) I_o + s12 \left[Q_o cos(2\psi) + U_o sin(2\psi) \right]. \tag{2.45}$$

Here, s_{11} and s_{12} are elements of the Mueller Matrix obtained using the Mie scattering method or some other method. During conventional Monte Carlo simulations, this phase function is rejection sampled to obtain values of θ and ψ at each light-tissue interaction.

Chapter 3

Forward Problem

3.1 Testing the pMC method

In this section, we examine the application of the phase function generalization of pMC to two problems that feature spherical scatterers with no absorption. In the first, simpler problem, concentration, radius, and incident light wavelength is varied for a suspension of single size scatterers. In the second problem, parameters of the tissue model in Table 2.1 are altered. In both cases reflectance obtained from a series of classical Monte Carlo simulations (cMC) are compared to results obtained by pMC calculations using trajectories from a baseline MC simulation. To perform the most stringent test of the range of parameters over which pMC is accurate, the whole tissue is perturbed rather than just a small tumorigenic region. The scattering medium is assumed to be semi-infinite with source and detector fibers, as described in Section 2.2, on top.

For all simulations, the Bohren and Huffman [3] implementation of Mie theory, which uses the indices of refraction of the medium and the scatterers, the radius of the scatterers, and the wavelength of light as inputs, was used to generate tables for the phase functions, $f(\theta)$ and $\widehat{f}(\theta)$ for the full range of θ values. These tables of 720 elements are used for rapid sampling of the phase function

both in the cMC simulations and the pMC calculations. The pMC calculation uses unperturbed as well as the perturbed scattering parameters These parameters as well as the saved trajectories are used according to Eq. (2.37) to reweight the photons. A separate set of trajectories is used for each collection fiber. Therefore, there are effectively four replicates of each pMC calculation.

The computers used for the simulations were: 1) 2 $\times$ 2.66 GHz Quad-Core Intel Xenon processors and 16 GB 1066MHz DDR3 RAM running Mac OS X 10.6.2; 2) 6 $\times$ 3.33 GHz Quad-Core Intel Xenon processors and 32 GB 1333 MHz DDR3 RAM running Mac OS X 10.8.2; and all code was compiled using gcc-4.2.

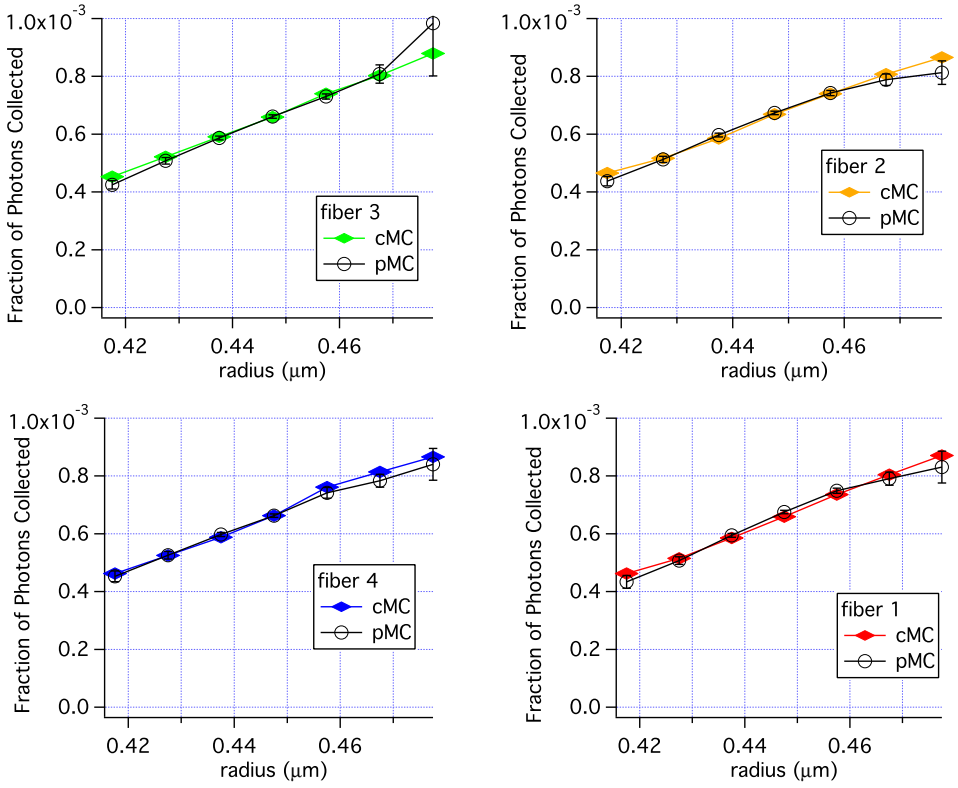

Figure 3.1: Comparison of pMC estimates of reflectance with estimates of reflectance obtained from independent cMC simulations when the *radius of a single size distribution* is perturbed. Error bars are standard errors of the mean.

3.2 Results

3.2.1 The Simpler Problem: One Size of Scatterers

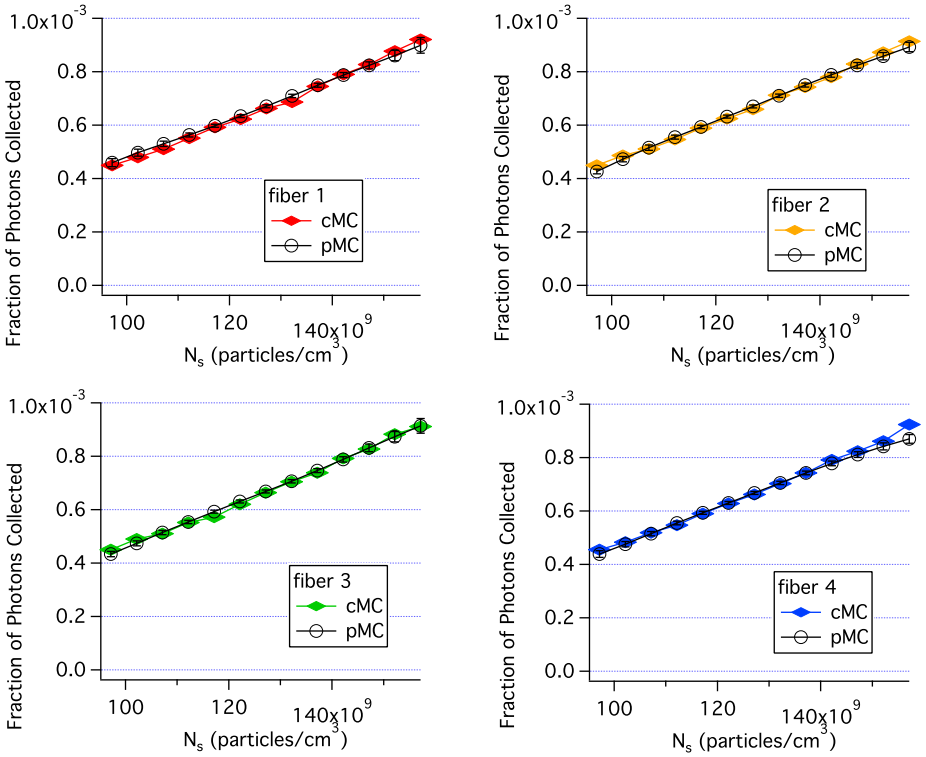

Figure 3.2: Comparison of pMC estimates of reflectance with independent cMC simulations results when the *concentration of single size scatterers* is perturbed. Each panel is for a different collection fiber shown in Fig. 2.1. Error bars are standard errors of the mean.

Fig. 3.2 compares pMC and cMC results when the concentration of single size scatterers is perturbed. The parameter values for the baseline simulation were: the radius of the scatterers, r = 0.4475μm, the number density, $N_s = 1.27 \times 10^{12}$ particles/cm^3, the wavelength, λ = 620 nm, the index of the medium was 1.332, the index of the scatterers was 1.390 and 20 million photons were incident through the delivery fiber. Particle concentration was perturbed by $\pm$25% for the pMC calculations. Each cMC simulation took 10 min. and the pMC calculations took a total of $\sim$1 min using computer 2. Consequently, the pMC results were obtained in 11 min., much shorter than the 130 min. needed for the cMC calculations. The agreement between cMC and pMC results

is quite good as seen in Fig. 3.2. By varying the concentration, the sensitivity of the perturbed reflectance to the weight factors described in Eq. (2.37) are determined without the phase function contribution.

Varying the radius, r, will vary the phase function along with μ_s. Fig. 3.1 shows the results of varying r using the same baseline simulation used for Fig. 3.2. There is good agreement from 0.4175 to 0.4775 μm, with some variation in the pMC results at $r = 0.4775$ μm.

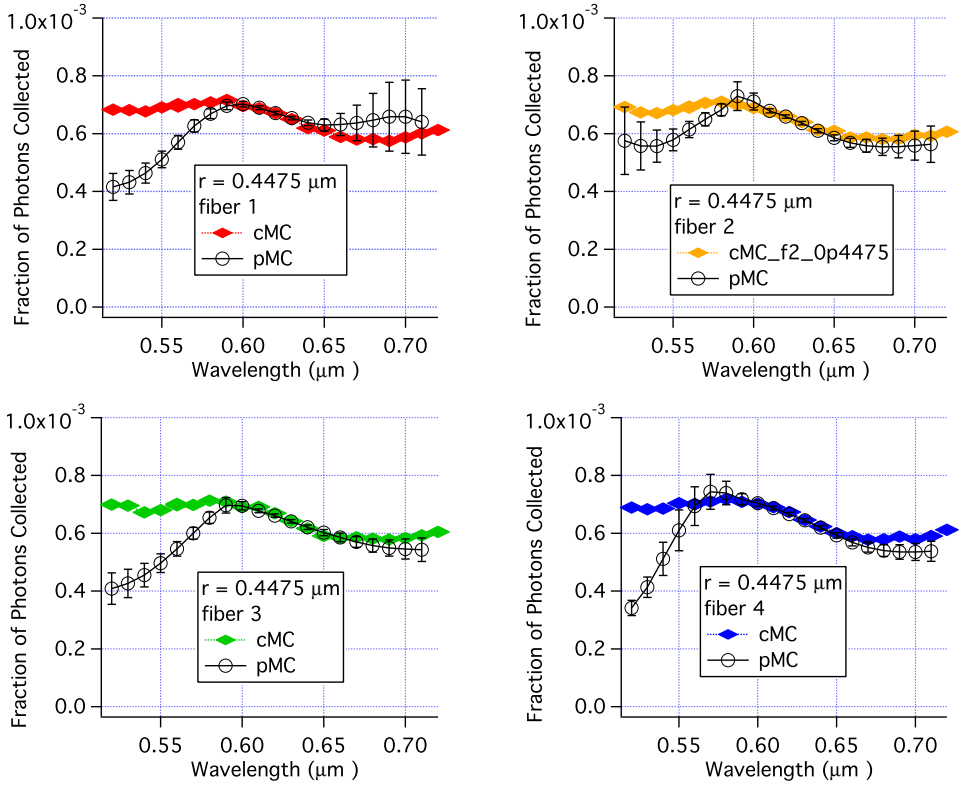

Figure 3.3: Comparison of pMC estimates of reflectance with independent cMC simulations results when *wavelength* is perturbed. The scattering particles had a radius of 447.5 nm. Each panel is for a different collection fiber shown in Fig. 2.1. Error bars are standard errors of the mean.

Similar to varying the radius, varying the wavelength changes both the phase function and μ_s, because the phase function and μ_s depend on the size parameter which is a function of wavelength as shown in Eq. (3.1). In Fig. 3.3, pMC and cMC results are compared for varying values of wavelength and constant values for other parameters. The parameters for the baseline simulation

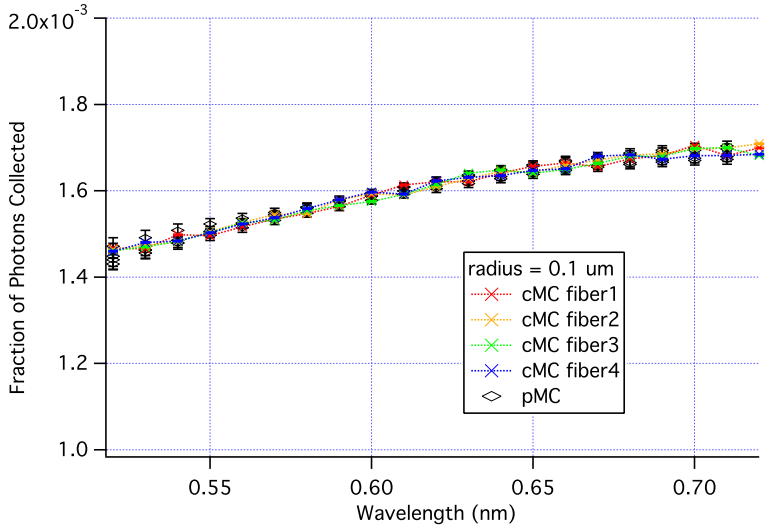

Figure 3.4: Comparison of pMC estimates of reflectance with independent cMC simulations results when *wavelength* is perturbed. The scattering particles had a radius of 100 nm.

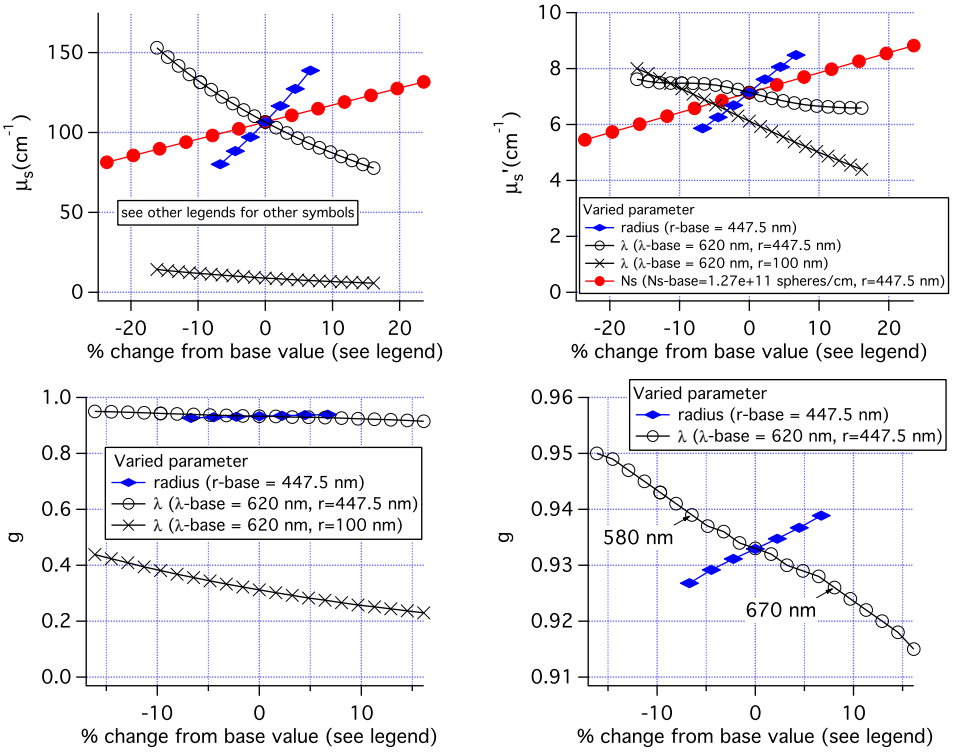

Figure 3.5: Scattering parameters used in the MC simulations using only one scatterer size. Top left: μ_s. Top right: $\mu_s^{'}$. Bottom left: anisotropy coefficient g, Bottom right: g on an expanded scale.

are the same as for Figs. 3.2 and 3.1. The agreement between pMC and cMC is excellent over the range 580 nm to 650 nm. However, for wavelengths of 550 nm and below, the pMC calculations underestimate the reflectance. Interestingly, large standard errors of the mean are not found in all cases, e.g. the results for fiber 4 at 520 nm. At wavelengths above 650 nm pMC results for one fiber overestimate reflectance while pMC results for the the other three collection fibers under estimate the reflectance. Nonetheless, in most cases the standard error of the mean overlaps with the cMC result. The cMC results are nearly the identical for each fiber. (When plotted on the same plot, the symbols overlap.) The pMC results, however, show a different trend for each fiber in Fig. 3.3 as a function of wavelength. The different trends for each fiber are due to the fact the pMC calculations for each fiber use a different base set of trajectories.

$$\text{size parameter} = 2\pi r n_{medium}/\lambda \tag{3.1}$$

To investigate further the effects of the phase function on the accuracy of pMC, simulations varying lambda were run with scatterers of 100 nm in radius. Excellent agreement between cMC and pMC was obtained as shown in Fig. 3.4. The baseline simulation used r = 0.100μm, $N_s = 1.83 \times 10^{10}$ particles/cm^3, λ = 620 nm, $n_{medium} = 1.332$ and $n_{scatterer} = 1.390$. Twenty million photons were incident for the baseline and cMC simulations.

The results of Figs. 3.2, 3.1, 3.3, and 3.4 can be placed in a broader context by examination of the scattering parameters used in the simulations. Fig. 3.5 shows these scattering parameters plotted versus the percent change in the varied parameter. When three sets of pMC simulations use the same baseline simulation such as the simulations varying N_s, radius, and λ of the 447.5 nm radius spheres, the parameters all overlap at the 0% point as in the top left graph for μ_s.

The reflectance results when N_s and radius were varied are quite similar as shown in Figs. 3.2,

and 3.1. This similarity is because the scattering parameters for the two sets of simulations were nearly the same. The range of μ_s values shown in the top left panel of Fig. 3.5 is nearly the same. The anisotropy factor, g was 0.933 when N_s was varied from 0.927 to 0.939. Given these similarities in scattering parameters it is not surprising that the results in Figs. 3.2 and 3.1 are similar.

When λ is varied with r = 447.5 nm, the range of scattering coefficients, 78-153 cm^{-1} is slightly larger than when radius is varied, 80-139 cm^{-1}. If only wavelengths from 550 nm to 710 nm are considered when λ is varied, then the variation in μ_s is slightly less than when radius is varied. However, Fig. 3.3 shows that pMC and cMC results are not the same over theis range. Examination of the bottom right panel shows that g is varying more when lambda is varied than when radius is varied even when only the range 550 to 710 nm is considered. Not until the wavelength range is reduced to 580 to 670 nm is the variation in g the same. This corresponds to the same range of wavelengths over which good agreement is found between the cMC and pMC results in Fig. 3.3. Clearly, the variation in g reduces the accuracy of the pMC results when g is large. However, if g is smaller, a much bigger variation in g can be tolerated as can be seen for the results using 100nm radius spheres in Fig. 3.4 and the bottom left panel of Fig. 3.5. Lastly, we note that variations in μ_s' are not a good predictor of the accuracy of pMC for this geometry where delivery and collection fibers are close together. The top right panel shows that varying lambda resulted in the smallest variation in μ_s', while varying the concentration resulted in the largest variation of μ_s'.

3.2.2 A More Complex Problem: Three Lognormal Distributions of Radii

The tissue model described in Section 2.1 is used for these simulations, with the parameters for the baseline simulation given in Table 2.1. As was done with the single size scatterers, concentration, radii, and wavelength are varied. However, rather than varying the concentration and mean radius of the entire suspension, the concentrations and mean radii of each distribution in Table 2.1 are

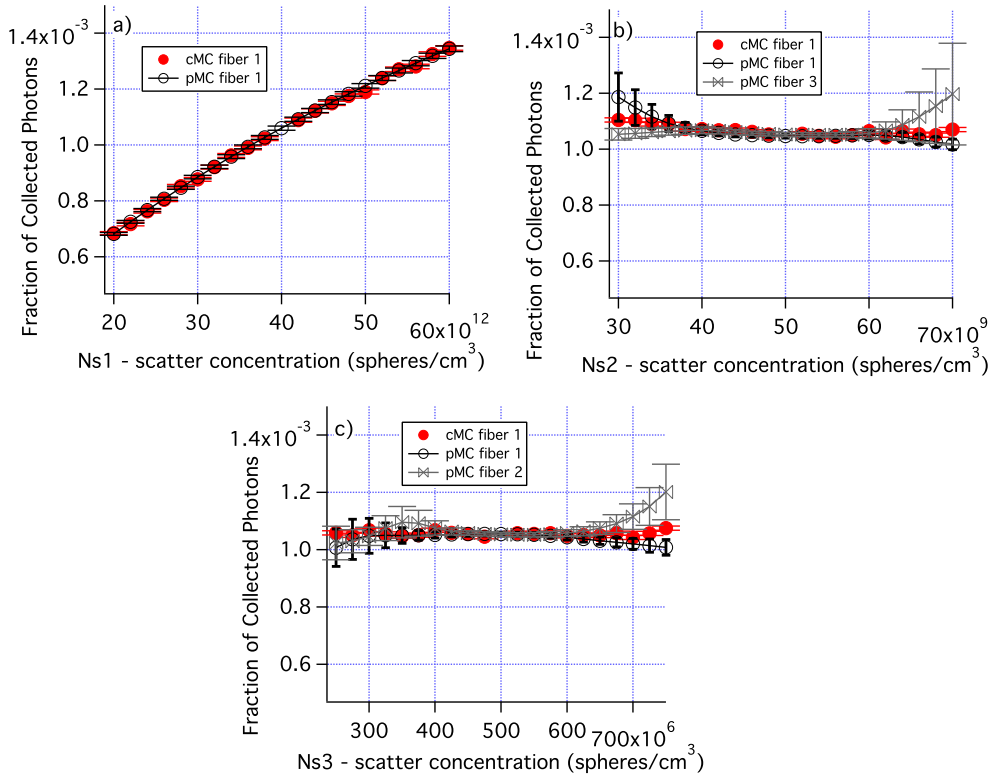

Figure 3.6: The number density of each of the distributions in Table 2.1 is varied. a) N_s for the smallest size distribution is varied. b) N_s for the middle size distribution is varied. c) N_s for the large size distribution is varied. Errors are standard error of the mean. Only cMC results for fiber 1 are shown for clarity. Similarly, only pMC results for one or two fibers are shown.

varied. Consequently all perturbations in parameters modified the phase function.

Fig. 3.6 shows how varying the number density of each distribution affects the fraction of collected photons as well as the accuracy of the pMC results. Fig. 3.6a demonstrates that when the concentration of the smallest distribution is varied by $\pm$ 50%, there is a large change in photon collection efficiency and the pMC results are very accurate. When the concentrations of distributions 2 and 3 are varied, there is very little change in photon collection efficiency. For larger changes in concentration, the standard errors of the mean increase for pMC. pMC results are shown for two fibers which are representative of the range of results obtained.

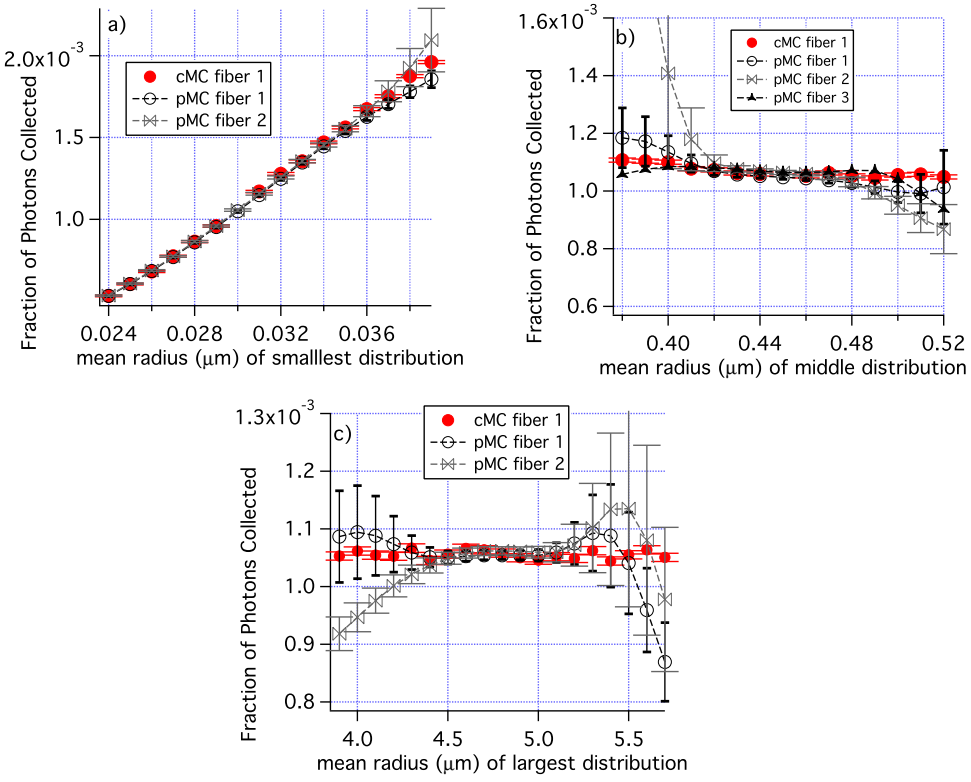

Figure 3.7: The mean radii of individual groups of scatterers are perturbed; a) distribution 1, b) distribution 2, and c) distribution 3 in Table 2.1. Only cMC results for fiber 1 are shown for clarity. Similarly, pMC results are shown for only some fibers. The range of the "Fraction of Photons Collected" is different in panel a) from all other graphs of "Fraction of Photons Collected". The error bars are standard errors of the mean.

In Fig. 3.7, the mean radii of each individual distribution was varied. Fig. 3.7a shows results

for the variation of the smallest radius from a baseline value of 0.030 μm. The pMC and cMC results overlap for all radii and results are quite accurate at the smallest radius used, r = 0.024 μm. Fig. 3.7b are results when the mean radius of the middle size distribution is varied from the baseline value of 0.045 μm. The pMC and cMC results agree well from about 0.42 μm to 0.49 μm, but the pMC results differ greatly from the cMC results in one case. Similar results were obtained when the radius of the largest distribution was varied, Fig. 3.7c.

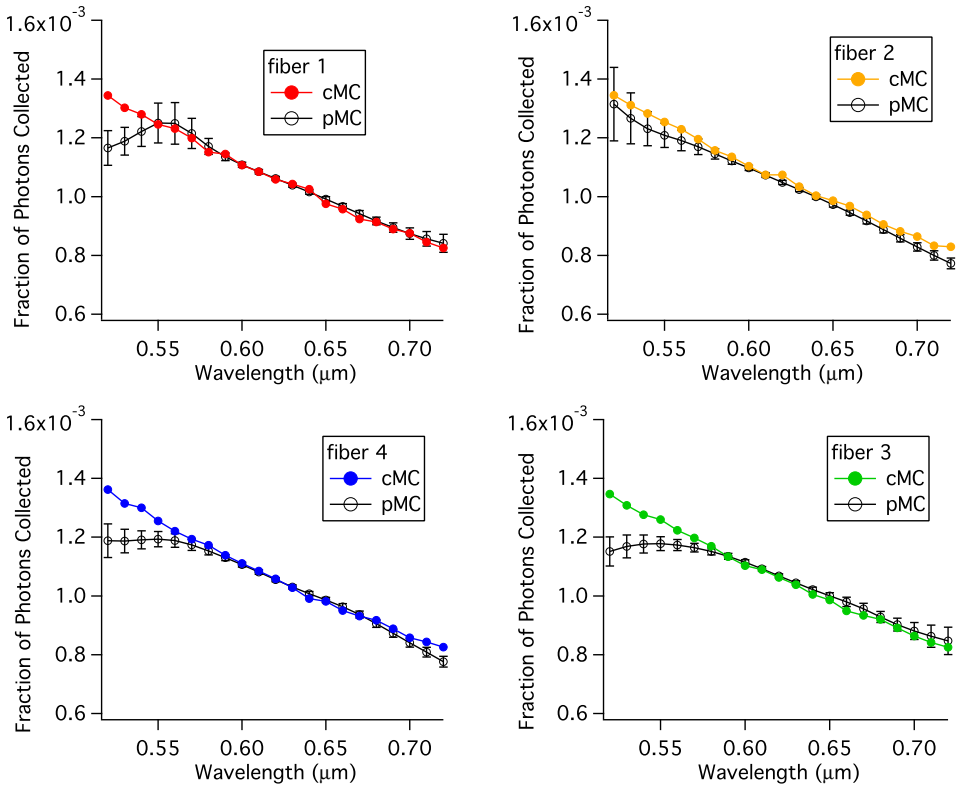

Figure 3.8: Comparison of pMC estimates of reflectance across wavelengths with calculations of reflectance obtained from independent cMC simulations of tissue.

Fig. 3.8 compares pMC and cMC results when the wavelength is perturbed from a baseline value of 620 nm. From 580 to 720 nm all of the pMC and cMC results are the same within errors. And for 3 of the 4 replicates, the agreement extends down to 560 nm.

Fig. 3.9 shows the parameters used in the MC simulations of tissue. Combining these data with those in Fig. 3.5 for single size scatterers, 4 classes of simulations can be examined; 1) μ_s varies,

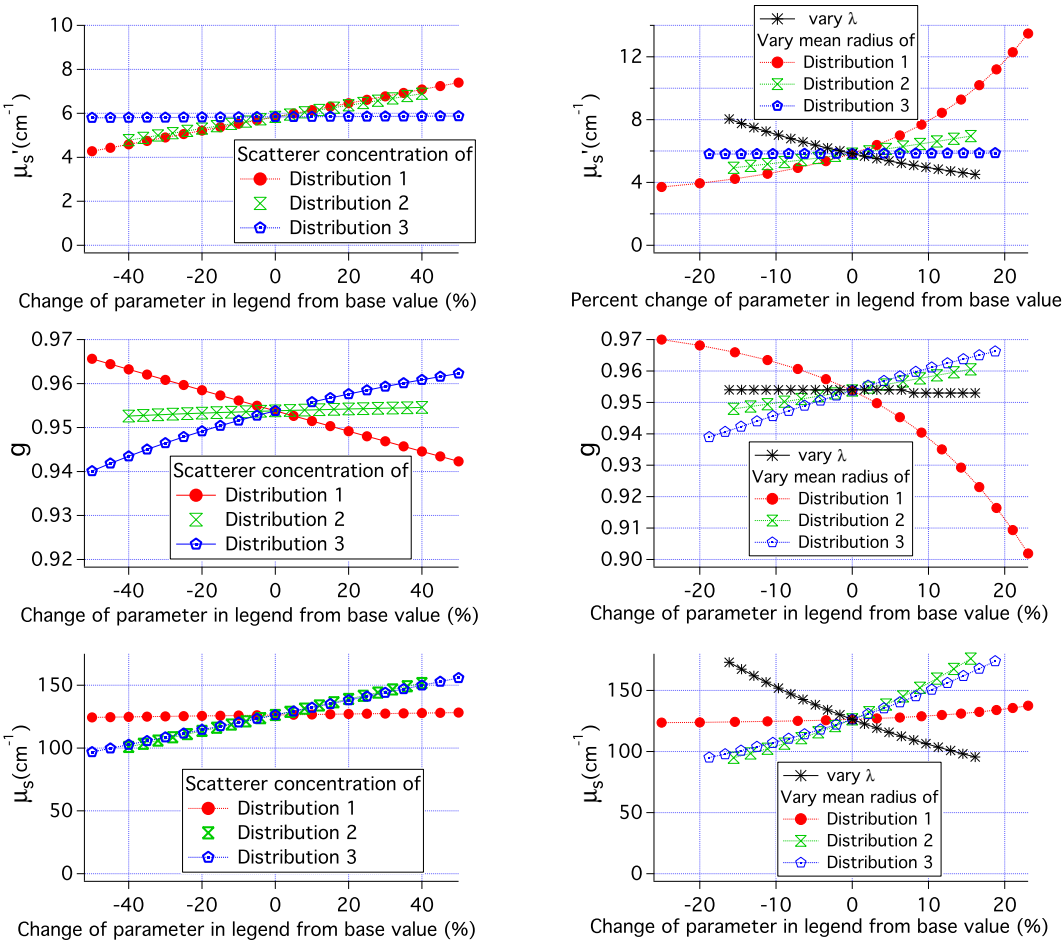

Figure 3.9: Scattering parameters for the simulation results shown in Figs. 3.6, 3.7 and 3.8.

while g is constant or nearly constant, 2) g varies while μ_s is nearly constant, 3) both g and μ_s vary for nearly constant μ_s', and 4) g, μ_s and μ_s' all vary. For each of these classes, there are 2 or 3 relevant simulations. By examining the pMC results for these simulations we can determine the range of scattering parameters over which the pMC and cMC results agree to within 1% of the cMC results, the results of Table 3.1 were obtained. When only μ_s varied, pMC results are accurate over a range of $\pm$15% the original value of μ_s. When only g varied, pMC results are accurate over a range of $\pm$25% the original value of (1-g). When both g and μ_s varied, then the variation of $\mu_s + 0.5(1-g)$ can be $\pm$20% when μ_s' is constant and slightly less if μ_s' varies.

Table 3.1: Range of parameter variation for $<1\%$ error in pMC reflectance calculation

	simulation types			
variation of	only μ_s varies	only g varies	only g and μ_s	g, μ_s and μ_s' vary
μ_s	$\pm 15\%$	NA	–	–
$(1-g)$	NA	$\pm 25\%$	–	–
$\mu_s + 0.5(1-g)$	NA	NA	$\pm 20\%$	$\pm 18\%$

3.3 Forward Problems with Polarization

This section shows the results we obtained when testing the performance of pMC reflectance estimates when polarization is taken into account. To test pMC performance, pMC reflectance estimates were compared to those obtained using cMC. cMC reflectance estimates were obtained by launching 20 million photons in a tissue representation characterized by a combination of the parameter values in Table 3.2 and parameter baseline values in Table 2.1. The ranges in Table 3.2 were chosen with the intent of modeling the length scales over which the index of refraction changes in epithelial cells. pMC estimates were obtained by launching 20 million photons in a single Monte Carlo simulation at the baseline parameter values in Table 2.1 and calculating the sample averages of the estimator $\widehat{\xi}$ to obtain perturbed reflectance values. Error bars shown on the plots represent the standard deviation of the sample means. All photon biographies were obtained from a modified version of the conventional Monte Carlo simulation code outlined in [5].

cMC and pMC calculations were performed on the High Performance Cluster at University of California, Irvine and a single private computer, respectively. The cluster runs CentOS 6.6 and code on the cluster was compiled using gcc$-$4.8.2. The private computer has 2 $\times$ 1.33 GHz Quad-Core AMD processors and 8 GB 1333 MHz DDR2 RAM running Ubuntu 10.04.4 LTS and our code was compiled using gcc$-$4.1.3. Benchmark tests were performed to ensure similar performance across the two settings.

Both polarized and unpolarized simulations were performed using the same optical properties and

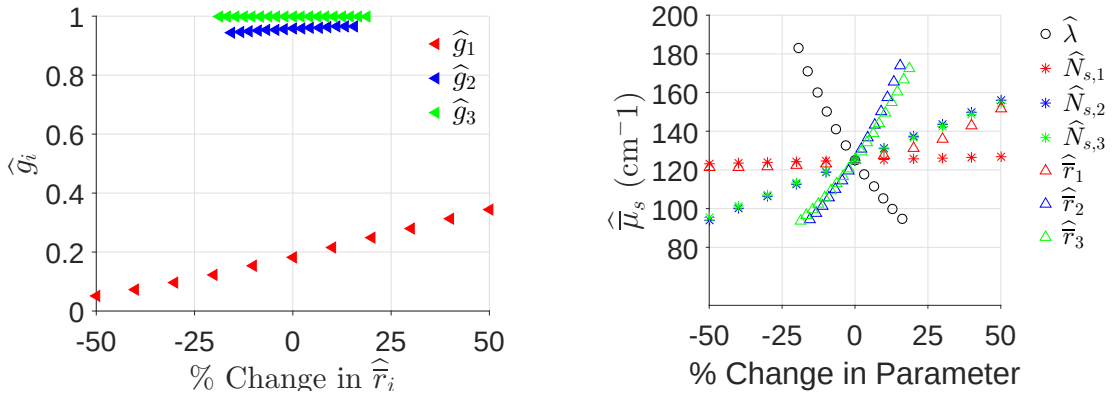

Figure 3.10: (a) Changes in the mean radii and how they relate to g_i. (b) Changes in the ensemble scattering coefficient for all perturbations.

probe geometry. Each cMC unpolarized light simulation launching 20 million photons took 22 – 45 minutes to run while the cMC simulations for polarized light transport took 6.7–18.9 hours. The post-processing module generating pMC reflectance estimates requires only ∼7 seconds and ∼13 seconds for unpolarized and polarized cases, respectively. Table 3.2 provides the perturbations used for the pMC tests we performed by applying perturbations in mean radii $\widehat{\overline{r}}_i$ and number densities $\widehat{N_{s,i}}$. Our model has three distributions of scatterers and each distribution has an associated anisotropy factor. We refer to the anisotropy factor of the ith distribution as g_i and the ensemble anisotropy factor of the medium as $\overline{g}$. Fig.3.10 shows how μ_s and g change as these parameters are changed with the parameter perturbation.

Table 3.2: Range of parameters examined in pMC calculations. Baseline $\overline{\mu}_s$ = 125 cm^{-1} and $\overline{g}$ = 0.9534.

Baseline Value, α	Perturbed Parameter, $\widehat{\alpha}$	g ranges	$\widehat{\overline{\mu}}_s$ ranges (cm^{-1})
λ = 620 nm	500 – 720 nm	$\overline{g}$ = 0.952 – 0.953	94.5 – 183
$N_{s,1}$= 4.00 ×10^{13} cm^{-3}	2.00 – 6.00 ×10^{13}cm^{-3}	g_1 = 0.183	123 – 127
$N_{s,2}$= 5.00 ×10^{10} cm^{-3}	2.5 – 7.5 ×10^{10}cm^{-3}	g_2 = 0.958	93.9 – 156
$N_{s,3}$= 5.00 ×10^{7} cm^{-3}	2.5 – 7.5 ×10^{7}cm^{-3}	g_3 = 0.999	95.5 – 154
$\overline{r}_1$=0.030 µm	0.015–0.045 µm	$\widehat{g}_1$ = 0.0502 – 0.345	121 – 152
$\overline{r}_2$=0.45µm	0.38 – 0.52 µm	$\widehat{g}_2$ = 0.945 – 0.966	94.2 – 174
$\overline{r}_3$=4.8 µm	3.9 – 5.7 µm	$\widehat{g}_3$ = 0.998 – 0.999	93.8 – 173

In both cMC and pMC simulations, we treat the source fiber center as the origin of our coordinate system. The center of Detector 1 in Fig. 2.1(c) resides along the y-axis and the center of Detector 2 resides along the x-axis of the coordinate system. Our pMC implementation requires the biographies of detected photons generated by an initial baseline cMC simulation.

In the case of polarized light transport, polarization is tracked by rotating the Stokes vector as outlined in [26]. All photons initially enter the medium linearly polarized and with polarization parallel to the x-axis. Each scattering event is characterized by polar and azimuthal angles, θ and ϕ, which are sampled from the phase function through a rejection sampling method used by Bartel and Hielscher [1]. Once the photon exits the medium, the Stokes vector is used to calculate the components of the photon weight that are, respectively, parallel and perpendicular to the x-axis.

3.3.1 Scattering model parameter perturbations

First, we investigate the ability of our pMC method to predict changes in reflectance produced by perturbations in the mean radii and/or number density of one of the three particle populations. Figs. 3.12 & 3.11 show a comparison between cMC and pMC reflectance estimates for Detector 1, which tallies photon weights with parallel or perpendicular polarization relative to the source. Figs. 3.11(a) – (f) provide a comparison of pMC and cMC reflectance resulting from perturbations in number density for each of the three scattering particle populations, whereas Figs. 3.12(a) – (f) compare pMC and cMC reflectance estimates for perturbations in mean radii.

The agreement between pMC and cMC estimates in Fig. 3.12 is linked to the range in which $\widehat{\overline{\mu}}_s$ is perturbed and the degree in which $\widehat{g}_i$ is perturbed. For perturbations of the scattering model parameters, the two largest ranges in $\widehat{\overline{\mu}}_s$ occur when the second and third mean radii are perturbed, as seen in Table 3.2. Although perturbations in the second and third mean radii produce similar $\widehat{\overline{\mu}}_s$ ranges, the perturbations in the second mean radii coincides with a larger perturbation in anisotropy factor which causes a more pronounced disagreement between pMC and cMC. As shown in Table 3.2,

we explored a perturbation range for mean radius that spans a larger range of ensemble $\widehat{\overline{\mu}}_s$ values as compared to perturbations in the number density. For example, perturbations we examined for number density of the first particle distribution $\widehat{N}_{s,1}$ result in a range of ensemble scattering coefficients $\widehat{\overline{\mu}}_s$ = 123–127 cm^{-1}, whereas perturbations we examined for first mean radius in the range $\widehat{\overline{r}}_1$ result in a broader range of $\widehat{\overline{\mu}}_s$ = 121–152 cm^{-1}. Similar observations can be made for the second and third populations. Because number density perturbations do not result in perturbation of the phase function and because of the smaller changes in $\widehat{\overline{\mu}}_s$, these pMC reflectance estimates have smaller variance than when perturbing mean radii. From this, we conclude that pMC performance is a function of the magnitude of $\widehat{\overline{\mu}}_s$ changes as well as the changes in the phase function which can be characterized by the change in g.

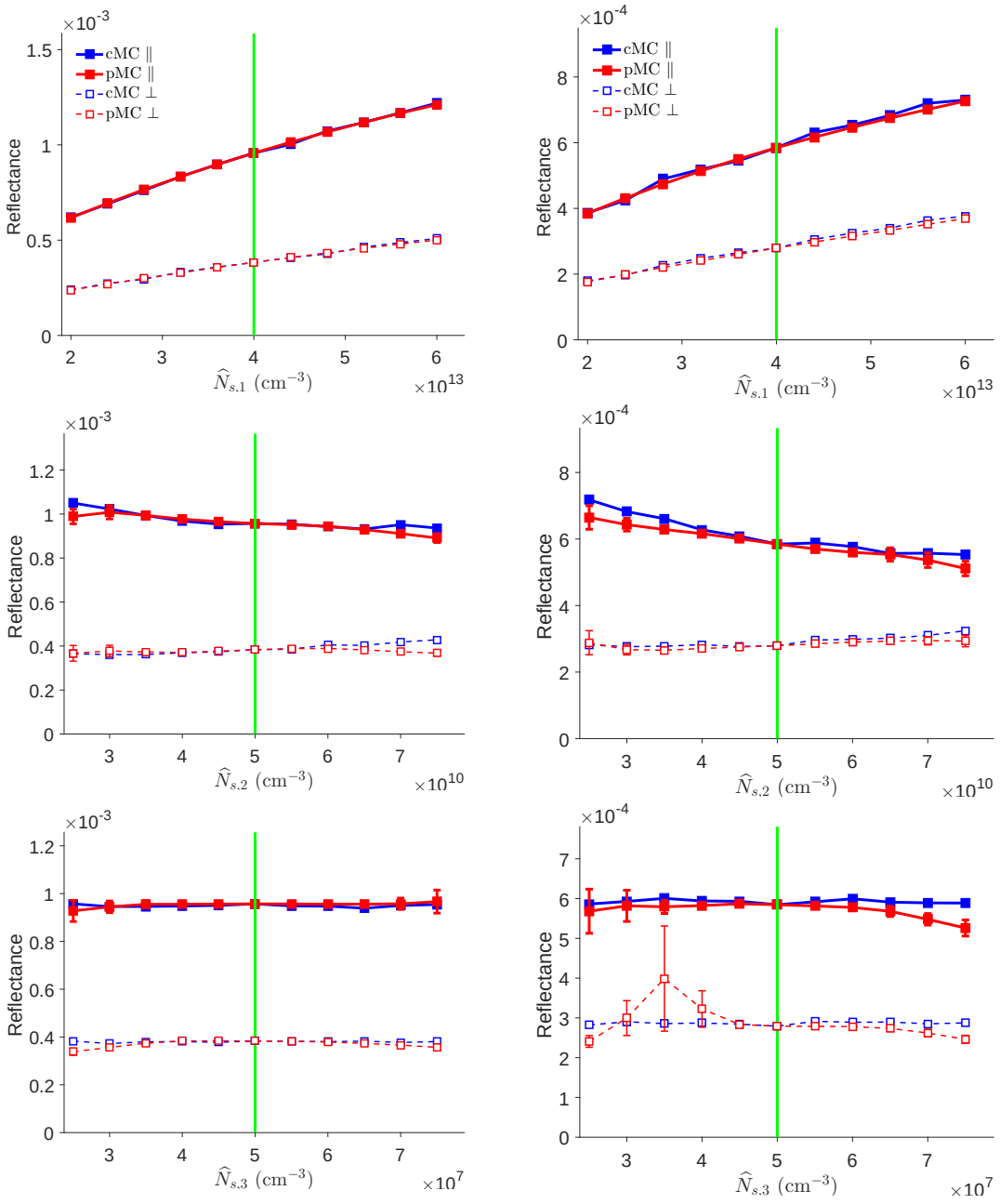

Figure 3.11: pMC and cMC estimates of reflectance of parallel and perpendicular polarization in Detector 1 for perturbations in number density ((a), (c), and (e)) and mean radii ((b), (d), and (f)). Solid lines display the trend for parallel reflectance estimates and dashed lines display the trend for perpendicular reflectance estimates.

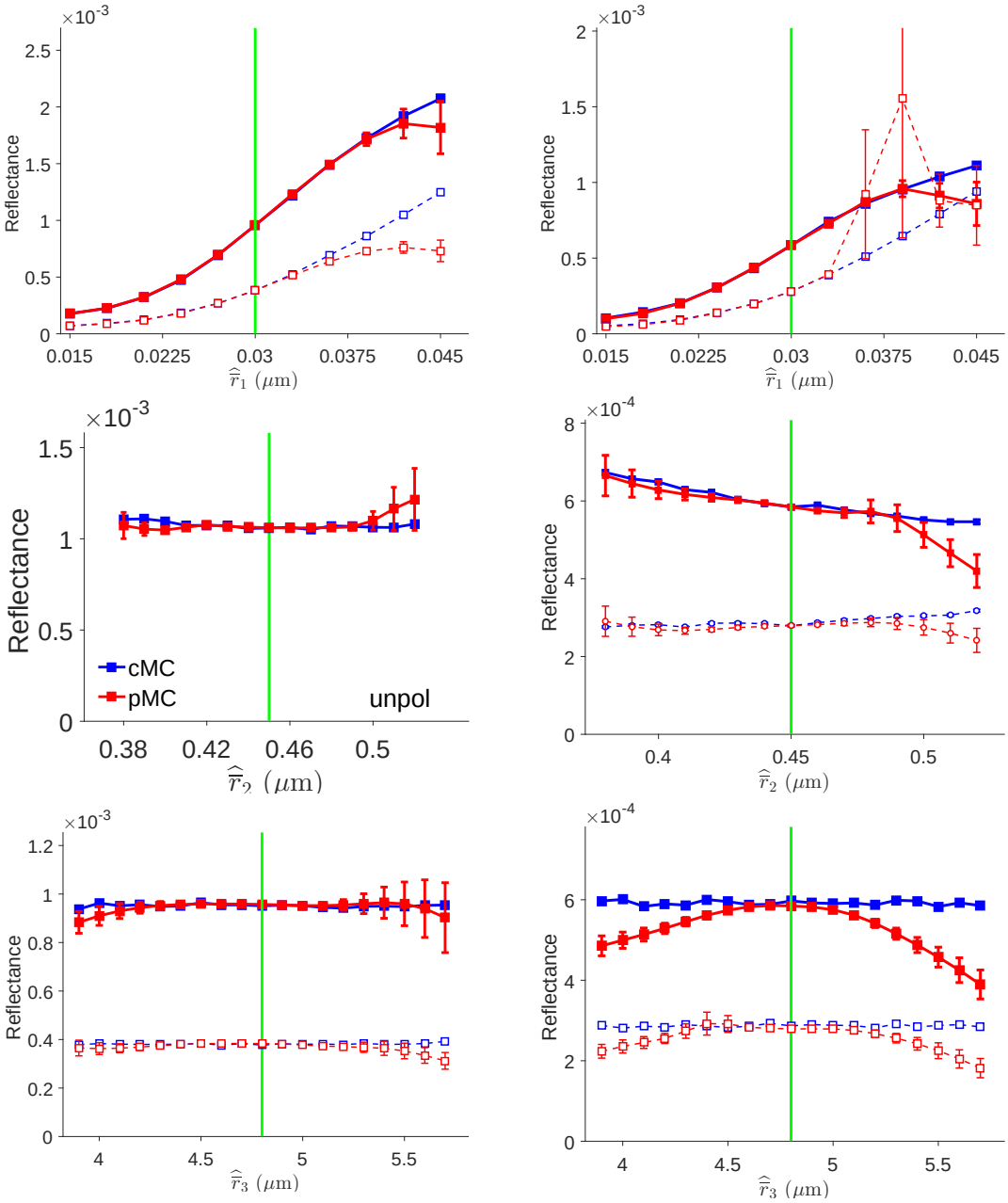

Figure 3.12: pMC and cMC estimates of reflectance of parallel and perpendicular polarization in Detector 1 for perturbations in number density ((a), (c), and (e)) and mean radii ((b), (d), and (f)). Solid lines display the trend for parallel reflectance estimates and dashed lines display the trend for perpendicular reflectance estimates.

Interestingly, Figs. 3.12 and 3.11 reveal that reflectance is highly sensitive to changes in the first distribution since the slopes of the plots in Figs. 3.12(a) and 3.12(b) are much greater than those

in Fig. 3.12(c)–(f). The sensitivity to the parameters of the first distribution can be explained by the low anisotropy factor of the associated phase function, which heavily promotes backscattering (See Table 3.2). This probe's bias toward detecting photons that have undergone backscattering is connected to the geometry of the probe which features angled detector fibers and a small source-detector separation. Based on $\mu_{s,i}/\overline{\mu}_s$ ratios, we would expect that 3.0%, 49.8%, and 47.2% of all scattering interactions would be with the first, second, and third distributions, respectively. However, analysis of the collected photons reveal that 4.7%, 48.8%, 46.4% of the scattering interactions are with the particles from the first, second, and third distribution, respectively. This represents a 54% increase in the number of interactions that the detected photons have with particles from the first population over the expected number of interactions. This is evidence that collected photons have enriched sensitivity toward changes to parameters associated with the first particle distribution.

Another important observation from the results in Fig. 3.12 is that the polarization-sensitive measurements provide sensitivity to parameters of the second particle distribution. This result differs from findings in [23] where we saw sensitivity to only parameters of the first distribution with unpolarized reflectance estimates. Changes in the first and second scattering populations, which represent protein complexes and organelles, are associated with dysplasia [25] and sensitivity to parameters of both first and second scattering populations may be helpful. Fig. 3.13 provides a comparison between pMC reflectance estimates for perturbations in the second mean radii for the cases of unpolarized and polarized light propagation and is intended to supplement the results in Fig. 3.12(d). In Fig. 3.13(a) and Fig. 3.13(b), the change in reflectance across $\widehat{\overline{r}}_2$ values are observable where as in Fig. 3.13(c), the changes in reflectance are not discernible from the noise in pMC and cMC reflectance estimates.

Although pMC's reflectance estimates are particularly poor for Detector 2 with perpendicular polarization, pMC accurately captures the 6% change in reflectance at $\widehat{\overline{r}}_2 = 0.41 - 0.47$ μm for Detector 2 with perpendicular polarization. The differences between pMC reflectance estimates in the

two detectors and polarizations will be further addressed in §3.3.2.

In Fig. 3.14, we explore the ability of pMC to reproduce spectral reflectance measurements. The baseline wavelength is $\lambda = 620\,\text{nm}$ and the wavelength perturbations are performed in the range of λ = 500–720 nm. Alteration of the wavelength requires modification of both the scattering coefficients and phase functions for all three scatterer distributions. The spectral asymmetry in Fig. 3.14 of pMC's performance relative to the baseline wavelength can be explained by the more rapid increase of the scattering coefficient as the wavelength decreases, as shown in Table 3.2. We also see that larger wavelength perturbations away from the baseline value of λ = 620nm result in larger standard deviations of the resulting pMC estimates. Perturbations from the baseline wavelength result in perturbations in both the ensemble scattering coefficient and the anisotropy factors, both of which drive increases in the variance of the estimator $\widehat{\xi}$.

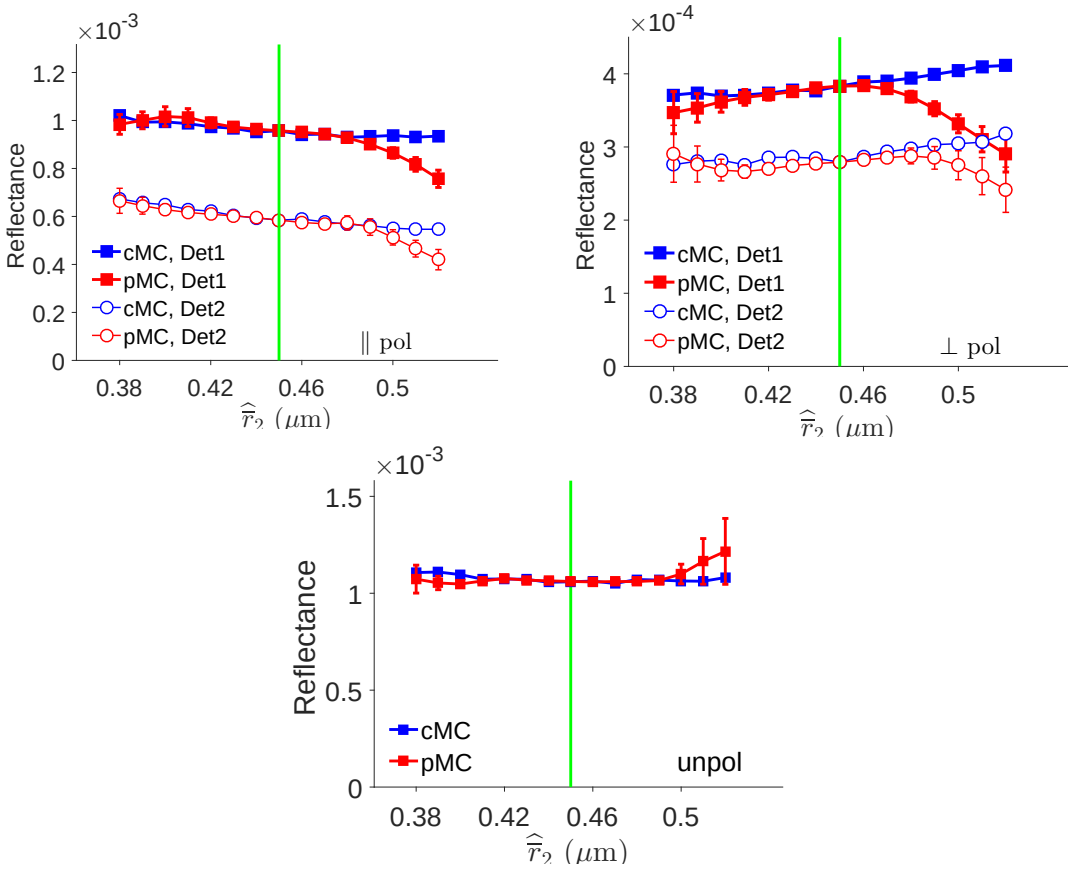

Figure 3.13: pMC estimates for perturbation in second mean radius in cases of (a) parallel polarization (b) perpendicular polarization and (c) unpolarized detection.

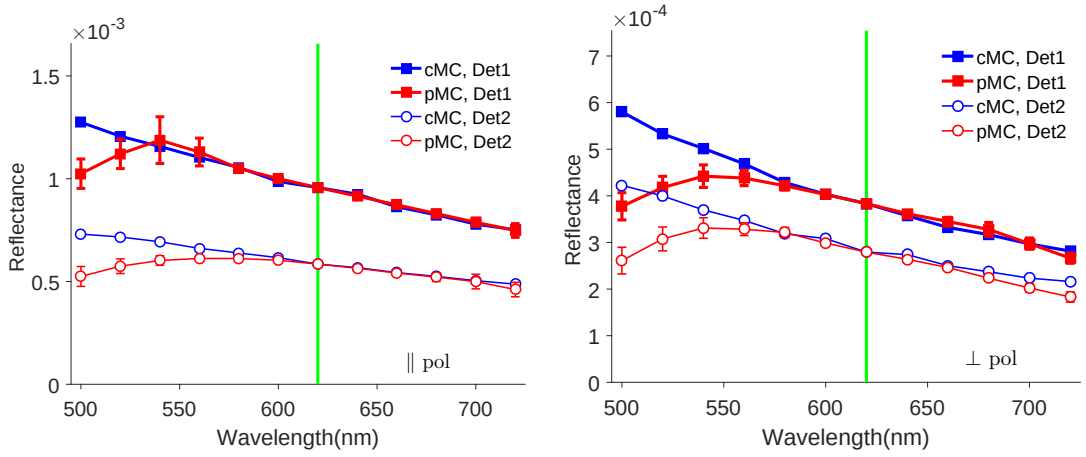

Figure 3.14: pMC and cMC estimates of reflectance across wavelength perturbations for polarized light propagation.

To summarize, we find that pMC's performance is negatively affected by: (1) increasing perturbations in the scattering coefficient and (2) extreme changes in the phase function which can be characterized by anisotropy factor perturbation. We have also demonstrated the utility of our method by showing that turning on polarization can add sensitivity to some parameters and by showing the accuracy of our method in the problem of perturbing across wavelength.

3.3.2 pMC performance and conventional Monte Carlo relative error

Second, we examine the relative performance of pMC reflectance estimates for parallel and perpendicular polarization as shown in Figs. 3.12 – 3.14. The top part of Table 3.3 shows the parameter ranges in which pMC estimates are within 5% of cMC reflectance estimates. The elements in the top part of Table 3.3 have a lower bound followed by an upper bound for the parameter values. These bounds are recorded as percentage changes from the baseline value for that parameter. For example, in the column Detector 1, $\parallel$ and in the row r_1, the parameter range is listed as -50%, $+40\%$. This means that pMC reflectance estimates for Detector 1 with parallel polarization were within 5% of cMC reflectance estimates for the range $r_1 = 0.015$ – 0.042 μm since the baseline value for r_1 is 0.03 μm. In the bottom part of Table 3.3, we compare the relative errors, which is defined as the standard deviation of the estimate divided by the mean, of pMC estimates at baseline parameter values.

The parameter ranges for accurate pMC estimates are governed by (a) the inherent noise of the baseline cMC simulation and (b) the size of the perturbation characterized by the changes in $\widehat{\overline{\mu}}_s$, $\widehat{g}_i$, and $\widehat{\mu}_{s,i}$. The effect of the inherent noise of the baseline cMC simulation can be determined through the comparison of the pMC reflectance estimates between Detector 1, $\parallel$ and Detector 1, $\perp$. This is because reflectance estimates use the exact same photon biographies and the differences between pMC performance can be attributed to the final weights. The fact that Detector 1, $\perp$ provides accurate pMC reflectance estimates over smaller parameter ranges than Detector 1, $\parallel$ can

be explained by the larger relative error in the baseline cMC simulation for Detector 1, $\perp$. Similar arguments can be made for the range of accuracy of the pMC estimates for Detector 2, $\parallel$ and Detector 2, $\perp$. The accuracy range reported for $N_{s,1}$ in Table 3.3 is the full range of parameter values for $N_{s,1}$ in this study; the true limit of pMC's performance lies beyond the range listed for $N_{s,1}$.

Table 3.3: Relative error and parameter ranges for polarized pMC reflectance estimates that are within 5% of cMC reflectance estimates for each detector.

Parameter	Detector 1, $\parallel$	Detector 1, $\perp$	Detector 2, $\parallel$	Detector 2, $\perp$
λ	-12.9%, $+16.1\%$	-6.4%, $+12.9\%$	-6.4%, $+12.9\%$	-6.4%, $+6.4\%$
r_1	-50%, $+40\%$	-30%, $+30\%$	-30%, $+10\%$	-20%, $+10\%$
r_2	-15.6%, $+8.9\%$	-15.6%, $+8.9\%$	-11.1%, $+6.7\%$	-13.3%, $+6.7\%$
r_3	-14.6%, $+16.7\%$	-6.25%, $+4.2\%$	-14.6%, $+10.4\%$	-8.3%, $+8.3\%$
$N_{s,1}$	-50%, $+50\%$	-50%, $+50\%$	-50%, $+50\%$	-50%, $+50\%$
$N_{s,2}$	-40%, $+50\%$	-30%, $+40\%$	-50%, $+20\%$	-50%, $+30\%$
$N_{s,3}$	-50%, $+50\%$	-50%, $+30\%$	-40%, $+40\%$	-10%, $+20\%$
	Detector 1, $\parallel$	Detector, 1 $\perp$	Detector 2, $\parallel$	Detector 2, $\perp$
rel. err.	6.74×10^{-3}	9.39×10^{-3}	8.53×10^{-3}	1.11×10^{-2}

The observed disparity between the relative errors of reflectance estimates for Detectors 1 and 2 is consistent with prior experimental work [25, 22, 16] and is consistent with the underlying physics of our model problem, which causes Detector 1 to detect a larger reflectance polarized parallel to the x-axis than Detector 2. This asymmetry in photon collection can be explained by a simple model outlined in [16] for a similar optical probe geometry. This model uses three assumptions: (1) photons undergo only 2 scattering interactions before entering a detector, (2) photons that are collected by Detector 1 have scattering events in the Y-Z plane and photons that are collected by Detector 2 have scattering events in the X-Z plane and (3) photons enter the medium with a

trajectory parallel to the z-axis. Fig. 3.15 shows plots of $|s_1(\theta)|^2$ and $|s_2(\theta)|^2$, where s_1 and s_2 are elements of the scattering amplitude matrix yielded by Mie Theory. The plot of $|s_1(\theta)|^2$ (blue) is the scattered irradiance per unit incident irradiance given that the incident light is polarized perpendicular to the scattering plane and the plot of $|s_2(\theta)|^2$ (red) is the scattered irradiance per unit incident irradiance given that the incident light is polarized parallel to the scattering plane [3]. Since each photon initially starts with polarization parallel to the x-axis, $|s_1(\theta)|^2$ can be interpreted as the phase function of scattering events in the Y-Z plane and $|s_2(\theta)|^2$ can be interpreted as the phase function of scattering events in the X-Z plane in the context of this three assumption model. The greatest difference between $|s_1(\theta)|^2$ and $|s_2(\theta)|^2$ occurs at a scattering angle of around 90°. In the event that a photon scatters at two 90° angles before entering the detector, then the implication of Fig. 3.15 is that a photon will end up in the Y-Z plane more frequently.

In this section, we have shown that there is a link between the noise of the baseline cMC simulation and the subsequent pMC performance. This link is helpful in understanding the difference in performance between the pMC reflectance estimates for parallel and perpendicular polarizations. Furthermore, to ensure better pMC performance, it is critical to keep the relative error of the baseline cMC simulation as low as possible.

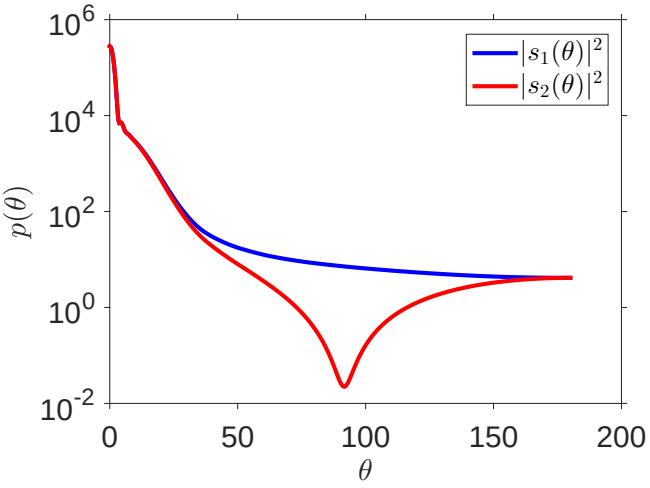

Figure 3.15: A plot of the s_1 and s_2 components produced by the Mie Scattering Method.

3.3.3 pMC and cMC computational efficiency comparisons

To examine the computational advantage provided by pMC over cMC, we examine their relative computational efficiencies, η, defined as

$$\eta = \frac{\overline{R}^2}{\sigma^2 T} \tag{3.2}$$

where $\overline{R}$ is the mean of the estimate, σ^2 is the variance, and T is the time required for the calculation [4]. This figure of merit allows for both characterization of the performance of the estimator and the amount of computational resources by combining the relative error of the estimator and the computational time. Furthermore, this figure of merit is dimensionless since relative error is proportional to $1/\sqrt{N}$ where N is the number of photons launched and T is proportional to N; this lack of dimensionality then allows for comparison across different algorithms or estimators. Figs. 3.16(a) and 3.16(b) plots the computational efficiency for perturbations in wavelength, mean radii, and number densities. Both plots feature a relatively constant computational efficiency value for cMC estimates, while pMC estimates have the highest computational efficiency when the change in the ensemble scattering coefficient is zero. The gain in computational efficiency for pMC estimates degrades as the perturbation in the ensemble scattering coefficient increases, which results from an increase in standard deviation of the estimates. In Fig. 3.16(a), plots of the computational efficiency are shown for perturbations in the mean radii whereas in Fig. 3.16(b), plots of the computational efficiency are shown for perturbations in the number density. A comparison of the pMC computational efficiency plots in Fig. 3.16(a) and 3.16(b), reveals that changes in $\widehat{\overline{r}}_1$ degrade the computational efficiency even though the range in $\widehat{\overline{\mu}}_s$ is much smaller than perturbations for $\widehat{\overline{r}}_2$ and $\widehat{\overline{r}}_3$. This degradation is the result of increases in the size of the standard deviation of the estimate, which is caused by the extreme perturbation in anisotropy factor of the phase function of the first population.

Recall that pMC is a true perturbation method; that is it works best if the perturbations are "small".

The pMC estimator is unbiased for *ALL* perturbations, but the larger the perturbation, the larger the statistical error it incurs. (When we say that the pMC estimator is unbiased we mean that on average the estimator will not tend to over-estimate or under-estimate the true value of the parameter.) Thus, in the limit of very large perturbations, it is more efficient computationally to examine independent Monte Carlo simulations of the baseline pMC and at the perturbed values of parameters of interest. As the size of the perturbation shrinks to zero, the advantage of pMC over independent conventional simulations tends to increase.

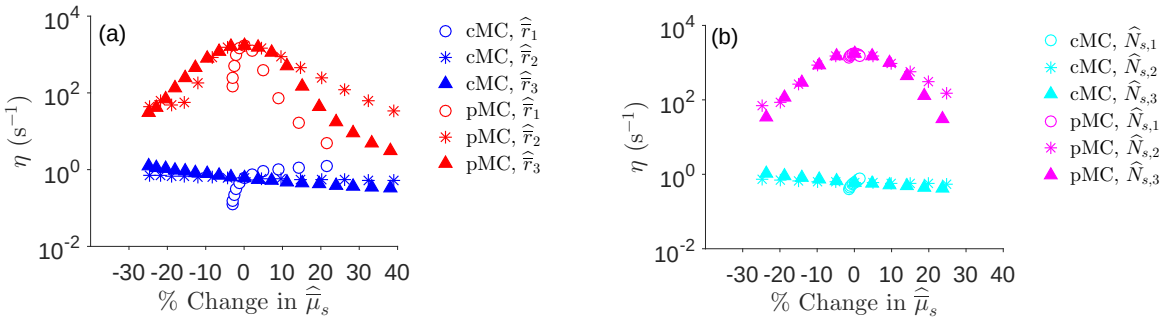

Figure 3.16: A comparison of the computational efficiency of pMC and cMC estimates for (a) perturbations in $\widehat{\bar{r}}_i$ and (b) perturbations in $\widehat{N}_{s,i}$. The pink and red symbols show the computational efficiency of pMC estimates. The blue and light blue symbols in the plot above are for the computational efficiencies of cMC estimates.

Chapter 4

Differential Monte Carlo

4.1 Differential Monte Carlo

This chapter explores the application of derivatives to the pMC estimator for our problem. The idea of obtaining derivatives based on MC simulations of neutron transport problems has previously been explored by Dejonghe, Rief, and Hall. This technique is useful in performing sensitivity analyses in forward MC simulations and may be used to drive inverse problem-solving via gradient-based optimization algorithms [11, 13]. It has also been shown that differentiation of the pMC estimator produces a new estimator whose sample means converge to the pMC derivative [12]. The equations can be used to estimate these sensitivities (i.e., rates of change) of photon weights with respect to parameters of interest are called differential Monte Carlo (dMC), terminology first used in [11]. Below, we show the equations that are used for each differential Monte Carlo calculation for our problem.

$$E\left[\frac{\partial \xi}{\partial \delta \mu_a}\right] = \frac{\partial R}{\partial \delta \mu_a} \tag{4.1}$$

The derivatives of the reflectance with respect to μ_s and higher order derivatives are found in a similar manner.

In order to calculate the sensitivity of reflectance to some parameter, the sensitivity of each photon biography to that parameter of interest must be calculated. If we take the derivative with respect to the parameter of interest, we find that

$$\frac{\partial \widehat{R}}{\partial \widehat{\alpha}} = \frac{1}{N} \sum_{n=1}^{N} \frac{\partial \widehat{\xi}_n}{\partial \widehat{\alpha}}. \tag{4.2}$$

The parameters for our particular problem are the mean radius of scatterers and the number density of scatterers and are represented with α in the above equation. The derivatives $\frac{\partial \widehat{\xi}}{\partial \alpha}$ can both be obtained through an application of the chain rule as shown below.

$$\frac{\partial \widehat{\xi}}{\partial \widehat{\alpha}_i} = \left(\frac{\partial \widehat{\xi}}{\partial \widehat{\mu}_{s,i}} \right) \left(\frac{\partial \widehat{\mu}_{s,i}}{\partial \widehat{\alpha}_i} \right). \tag{4.3}$$

Since calculation of the estimator $\widehat{\xi}$ varies with how scattering is simulated, the estimator for $\frac{\partial \widehat{\xi}}{\partial \widehat{\mu}_{s,i}}$ is also dependent on the scattering method used. Below, we show how to calculate $\frac{\partial \widehat{\xi}}{\partial \widehat{\mu}_{s,i}}$ for both the Distribution Selection Scattering Method and the Composite Phase Function Scattering Method.

4.1.1 Composite Phase Function Scattering Method

Now, we will show the equations involved with dMC calculations for the Composite Phase Function Scattering Method. Using the Composite Phase Function Scattering Method, the perturbed

weight would be

$$\begin{aligned}
\widehat{\xi}_n &= A_n * B_n * C_n \\
A_n &= \xi_n \left(\frac{\widehat{\overline{\mu}}_s}{\overline{\mu}_s}\right)^j \exp\left[-(\widehat{\mu}_a - \mu_a)L\right] \\
B_n &= \exp\left[-(\widehat{\overline{\mu}}_s - \overline{\mu}_s)L\right] \\
C_n &= \prod_{k=1}^{j} \left[\frac{\widehat{\overline{f}}_k}{\overline{f}_k}\right]
\end{aligned} \tag{4.4}$$

where $\overline{f}_k = \frac{\mu_{s,1}}{\overline{\mu}_s} f_{k,1} + \frac{\mu_{s,2}}{\overline{\mu}_s} f_{k,2} + ... + \frac{\mu_{s,m}}{\overline{\mu}_s} f_{k,m}$ and $\widehat{\overline{f}}_k = \frac{\widehat{\mu}_{s,1}}{\widehat{\overline{\mu}}_s} \widehat{f}_{k,1} + \frac{\widehat{\mu}_{s,2}}{\widehat{\overline{\mu}}_s} \widehat{f}_{k,2} + ... + \frac{\widehat{\mu}_{s,m}}{\widehat{\overline{\mu}}_s} \widehat{f}_{k,m}$. Here, j is the total number of interactions the nth collected photon has with the medium. For the case of a composite phase function, $\frac{\partial C_n}{\partial \widehat{\mu}_{s,i}}$ is calculated in the following way:

$$\begin{aligned}
\frac{\partial C}{\partial \widehat{\mu}_{s,i}} &= \frac{\partial}{\partial \mu_{s,i}} \left[\prod_{m=0}^{j} \frac{\widehat{f}(\theta_m)}{f(\theta_m)}\right] \\
&= \frac{\partial f(\theta_1)}{\partial \widehat{\mu}_{s,i}} \frac{1}{f(\theta_1)} \prod_{m=0}^{j} \frac{\widehat{f}(\theta_m)}{f(\theta_m)} + \frac{\partial f(\theta_2)}{\partial \widehat{\mu}_{s,i}} \frac{1}{f(\theta_2)} \prod_{m=0}^{j} \frac{\widehat{f}(\theta_m)}{f(\theta_m)} + ... + \frac{\partial f(\theta_j)}{\partial \widehat{\mu}_{s,i}} \frac{1}{f(\theta_m)} \prod_{m=0}^{j} \frac{\widehat{f}(\theta_m)}{f(\theta_m)} \\
&= \sum_{k=0}^{j} \frac{\partial f(\theta_k)}{\partial \mu_{s,i}} \frac{1}{f(\theta_k)} \frac{f(\theta_j)}{\widehat{f}(\theta_j)} \prod_{m=0}^{j} \frac{\widehat{f}(\theta_m)}{f(\theta_m)}.
\end{aligned} \tag{4.5}$$

$\frac{\partial \widehat{\overline{f}}_k}{\partial \widehat{\mu}_{s,i}}$ is dependent on the number of distributions of scatterers in the medium. If the medium has three groups of scatterers, the value of $\frac{\partial \widehat{\overline{f}}_k}{\partial \widehat{\mu}_{s,i}}$ is:

$$\frac{\partial \widehat{\overline{f}}_k}{\partial \widehat{\mu}_{s,i}} = \frac{\widehat{f}_{k,i}(\widehat{\overline{\mu}}_s - \widehat{\mu}_{s,i}) - \widehat{f}_{k,i'}\widehat{\mu}_{s,i'} - \widehat{f}_{k,i''}\widehat{\mu}_{s,i''}}{\left(\widehat{\overline{\mu}}_s\right)^2}. \tag{4.6}$$

As one can see, calculation of the term $\frac{\partial C_n}{\partial \widehat{\mu}_{s,i}}$ is simpler for the case of the Distribution Selection Scattering Method. The processing of performing dMC calculations for each photon results in

75% fewer calculations per photon biography under the Distribution Selection Scattering Method.

4.1.2 Differential Monte Carlo for Distribution Selection Scattering Method

Before showing how to calculate $\frac{\partial\widehat{\xi}}{\partial\widehat{\mu}_{s,i}}$ in the Distribution Selection Scattering Method, we will first reproduce the estimator $\widehat{\xi}$ below and break up the estimator into three different factors:

$$\begin{aligned}
\widehat{\xi} &= A*B*C \qquad (4.7)\\
A &= \xi\left(\frac{\widehat{\mu}_{s,1}}{\mu_{s,1}}\right)^{j_1}\left(\frac{\widehat{\mu}_{s,2}}{\mu_{s,2}}\right)^{j_2}\ldots\left(\frac{\widehat{\mu}_{s,m}}{\mu_{s,m}}\right)^{j_m}\exp\left[-(\widehat{\mu}_a-\mu_a)L\right]\\
B &= \exp\left[-(\widehat{\overline{\mu}}_s-\overline{\mu}_s)L\right]\\
C &= \prod_{l_1=1}^{j_1}\left[\frac{\widehat{f}_{l_1,1}}{f_{l_1,1}}\right]\prod_{l_2=1}^{j_2}\left[\frac{\widehat{f}_{l_2,2}}{f_{l_2,2}}\right]\ldots\prod_{l_m=1}^{j_m}\left[\frac{\widehat{f}_{l_m,m}}{f_{l_m,m}}\right].
\end{aligned}$$

The derivative $\frac{\partial\widehat{\xi}_n}{\partial\widehat{\mu}_{s,i}}$can be calculated in the following manner.

$$\frac{\partial\widehat{\xi}}{\partial\widehat{\mu}_{s,i}} = \frac{\partial A}{\partial\widehat{\mu}_{s,i}}BC + A\frac{\partial B}{\partial\widehat{\mu}_{s,i}}C + AB\frac{\partial C}{\partial\widehat{\mu}_{s,i}} \qquad (4.8)$$

where

$$\begin{aligned}
\frac{\partial A}{\partial\widehat{\mu}_{s,i}} &= \frac{j_i\xi}{\mu_{s,i}}\left(\frac{\widehat{\mu}_{s,1}}{\mu_{s,1}}\right)^{j_1}\ldots\left(\frac{\widehat{\mu}_{s,i}}{\mu_{s,i}}\right)^{j_i-1}\ldots\left(\frac{\widehat{\mu}_{s,m}}{\mu_{s,m}}\right)^{j_m}\exp\left[-(\widehat{\overline{\mu}}_a-\overline{\mu}_a)L\right] \qquad (4.9)\\
&= \frac{j_i}{\widehat{\mu}_{s,i}}\frac{\mu_{s,i}}{\widehat{\mu}_{s,i}}A
\end{aligned}$$

and

$$\frac{\partial B_n}{\partial \widehat{\mu}_{s,i}} = -L\exp\left[-(\widehat{\overline{\mu}}_s - \overline{\mu}_s)L\right] \tag{4.10}$$

$$= -LB_n. \tag{4.11}$$

and

$$\frac{dC}{\partial \widehat{\mu}_{s,i}} = 0. \tag{4.12}$$

4.1.3 Further differential Monte Carlo Calculations

Once the estimate for $\frac{\partial \widehat{\xi}}{\partial \widehat{\mu}_{s,i}}$ is calculated, this algorithm then proceeds to calculate the derivative $\frac{\partial \widehat{\mu}_{s,i}}{\partial \widehat{\alpha}_i}$, where α is a parameter of interest. For this tissue model, the parameters of interest are: number density, $N_{s,i}$, and mean radius, $\widehat{\overline{r}}_i$. Remember that mean radius is related to the scattering coefficient, μ_s by:

$$\widehat{\mu}_{s,i} = \int_{a(r)}^{b(r)} Q_{scat,i}(r) N_{a,i}(r) dr \tag{4.13}$$

where

$$N_{a,i}(\overline{r}_i, t) = conc(\overline{r}_i, t) N_{s,i} \pi t^2 \tag{4.14}$$

and Q_{scat} is the effective scattering cross section obtained by Mie calculations, and *conc* is the probability distribution function that describes the scatterer population. For the case of lognormally

distributed scatterer radii,

$$conc_i(\bar{r}_i,t) = \frac{1}{norm_i}\frac{1}{t}exp\left(\frac{-[log(t)-log(\bar{r}_i)]^2}{2\sigma_i^2}\right). \tag{4.15}$$

In Eq. (4.16), the value $norm_i$ is a normalization factor which is calculated by taking the integral of Eq. (4.16) from $-\infty$ to ∞.

$$norm_i(\bar{r}_i,t) = \int_{-\infty}^{\infty}\frac{1}{t}exp\left(\frac{-[log(t)-log(\bar{r}_i)]^2}{2\sigma_i^2}\right)dt. \tag{4.16}$$

In silica, we perform this calculation by allowing the user to set the upper and lower limits for this integration as well as the width of trapezoids for a trapezoid sum integration. Taking the derivative of Eq. (4.13) with respect to the scattering coefficient contribution of the ith distribution, we get:

$$\frac{\partial\mu_{s,i}}{\partial N_{s,i}} = \int_{a(r)}^{b(r)} Q_{scat,i}(r)\frac{\partial N_{a,i}}{\partial N_{s,i}}dr \tag{4.17}$$

where

$$\frac{\partial N_a}{\partial N_{s,i}} = conc_i(\bar{r}_i,t)\pi t^2. \tag{4.18}$$

$$\frac{\partial\mu_{s,i}}{\partial\bar{r}_i} = \int_{a(r)}^{b(r)} Q_{scat,i}(r)\frac{\partial}{\partial\bar{r}_i}N_{a,i}(t)dr \tag{4.19}$$

where

$$\frac{\partial N_{a,i}}{\partial \bar{r}_i} = N_{s,i} \frac{\partial conc_i(\bar{r}_i,t)}{\partial \bar{r}_i} \pi t^2 \tag{4.20}$$

where

$$\frac{\partial conc_i(\bar{r}_i,t)}{\partial \bar{r}_i} = \frac{log(t) - log(\bar{r}_i)}{rt\sigma^2 norm_i} exp\left[\frac{-(log(t) - log(\bar{r}_i))^2}{2\sigma^2}\right] - \frac{1}{tnorm_i^2} exp\left[\frac{-(log(t) - log(\bar{r}_i))^2}{2\sigma^2}\right] \int_{a(r)}^{b(r)} \frac{log(t) - log(\bar{r}_i)}{t\bar{r}\sigma^2} exp\left(\frac{-(log(t) - log(\bar{r}_i))^2}{2\sigma^2}\right) dt \tag{4.21}$$

4.1.4 Finite Difference and dMC Comparisons

To test the dMC method, we compared estimates of the sensitivity to reflectance with the estimates of those derivatives obtained through finite difference. Although, theoretically, dMC estimates of sensitivity should be more accurate than Finite Difference (FD) estimates, this early test was performed to ensure that dMC was coded correctly; this author at least expected the magnitudes of all FD estimates and dMC estimates to agree. For our tests, we ran a mother Monte Carlo simulation for polarized light transport and launched 20 million photons at a wavelength of 520 nm for each case. The probe geometry shown in Fig. 2.1c was used in these simulations. Collected photon biographies were then submitted to differential Monte Carlo equations. For the finite difference method, Monte Carlo simulations were launched at slightly perturbed optical properties and the finite difference was taken between the reflectance generated by the MC simulation with perturbed properties and the reflectance generated by the MC simulation with baseline properties. The list of slightly perturbed properties and the ”baseline“ properties are shown in the table below.

Using the values from the table above, we can see that dMC estimates for $\frac{\partial \widehat{R}}{\partial \widehat{r}_1}$ deviate from finite difference estimates by 42.2%. $\frac{\partial \widehat{R}}{\partial \widehat{N}_{s,1}}$ by 1.50% $\frac{\partial \widehat{R}}{\partial c_{oxyHb}}$ by 0.642% and $\frac{\partial \widehat{R}}{\partial c_{deoxyHb}}$ by 1.86%. The es-

Table 4.1: Parameter variation used in Finite Difference calculation

$\widehat{r}_1$	$\widehat{N}_{s,1}$	Wavelength (nm)	oxyHb Concentration (mM)	deoxyHb Concentration (mM)
0.611 25 µm	2.0066 $\times 10^{10}$	520	0.01	0.002
0.610 25 µm	2.0066 $\times 10^{10}$	520	0.01	0.002
0.611 25 µm	2.0166 $\times 10^{10}$	520	0.01	0.002
0.611 25 µm	2.0066 $\times 10^{10}$	520	0.0101	0.002

Table 4.2: Finite Difference and dMC comparison

Finite Difference Estimates				
Det.	$\frac{\partial \widehat{R}}{\partial \widehat{r}_1}$	$\frac{\partial \widehat{R}}{\partial \widehat{N}_{s,1}}$	$\frac{\partial \widehat{R}}{\partial c_{oxyHb}}$	$\frac{\partial \widehat{R}}{\partial c_{deoxyHb}}$
1, $\parallel$	0.000393967	4.27603×10^{-15}	-8.7×10^{-5}	-0.0001
1, $\perp$	0.000329344	4.42556×10^{-15}	-7.1×10^{-5}	-8×10^{-5}
2, $\parallel$	-0.000219967	-1.41654×10^{-15}	-7.6×10^{-5}	-8.5×10^{-5}
2, $\perp$	0.000169852	4.22021×10^{-15}	-9.5×10^{-5}	-0.000105
dMC Estimates				
Det.	$\frac{\partial \widehat{R}}{\partial \widehat{r}_1}$	$\frac{\partial \widehat{R}}{\partial \widehat{N}_{s,1}}$	$\frac{\partial \widehat{R}}{\partial c_{oxyHb}}$	$\frac{\partial \widehat{R}}{\partial c_{deoxyHb}}$
1, $\parallel$	3.45×10^{-4}	4.21×10^{-15}	-8.61×10^{-5}	-9.55×10^{-5}
1, $\perp$	3.63×10^{-4}	4.42×10^{-15}	-7.12×10^{-5}	-7.90×10^{-5}
2, $\parallel$	-1.14×10^{-4}	-1.38×10^{-15}	-7.56×10^{-5}	-8.39×10^{-5}
2, $\perp$	3.53×10^{-4}	4.29×10^{-15}	-9.43×10^{-5}	-1.05×10^{-4}

timates for the $\frac{\partial \widehat{R}}{\partial \widehat{r}}$ values may be less accurate than dMC estimates for $\frac{\partial \widehat{R}}{\partial \widehat{N}_{s,1}}$ or $\frac{\partial \widehat{R}}{\partial c_{oxyHb}}$ or $\frac{\partial \widehat{R}}{\partial c_{deoxyHb}}$. This is because obtaining the scattering coefficient from the mean radius requires integration (see Eq. 4.13). The integration in that equation is performed using a trapezoidal rule integration in which the user must set the uniform partition sizes. This is the only parameter affected by the partition size of an integral. If the step size chosen for the finite difference estimate was much smaller than the partition size used for the trapezoidal rule integration in Eq. 4.13, then the perturbed scattering coefficient may not change as much as it should, resulting in inaccurate values for the reflectance estimates. The strength of dMC sensitivity estimates over finite difference approximations is further supported by the fact that similar experiments were run to the ones shown

in Subsection 4.1.5, but with finite difference values instead of dMC derivative estimates used to drive the Levenberg-Marquardt Algorithm no optimizations converged.

4.1.5 dMC results Performance with Unpolarized Light

This section involves our analysis of the performance of the dMC calculations. The computer used for these simulations had an AMD Phenom II 1045T Six-Core Processor and 8GB of DDR2 RAM running Ubuntu 10.04.3 LTS and all code was compiled using gcc-4.2. Our analysis involves a comparison of two types of sensitivity estimates which we call dMC and d-cMC. For all dMC results, 2 billion photons were launched in a medium which contained the three scatterer populations described in Table 2.1. Next, using the biographies of collected photons and the dMC calculations outlined in Eqs. (4.8) – (4.21) estimates for the sensitivity of the reflectance to parameters of interest were then calculated at various optical properties listed in Table 4.3. These dMC estimates for the sensitivity are then obtained at a non-zero perturbation from the baseline optical properties. For the d-cMC estimates of sensitivity, 20 million photons are launched in a Monte Carlo simulation. The photons propagate through a The range of optical properties of the medium in which the photons propagate is listed Table 4.3. No perturbation in the optical properties of the medium is applied when performing dMC calculations (The perturbed "hatted" values were always equal to their unperturbed "unhatted" values in Eqs. (4.8) – (4.21)) to get d-cMC estimates of the sensitivity. As a side note, we adopt the terms "dMC" and "d-cMC" to draw a parallel to our previous comparison between pMC and cMC reflectance estimates. In the previous section, pMC reflectance estimates were obtained by using pMC equations to calculate reflectance estimates at some perturbation away from the baseline optical properties where as in cMC, the reflectance estimates are always calculated at the same optical properties of the original Monte Carlo simulation in which the sample of photon biographies was taken. When we compared pMC and cMC estimates together, our objective was to characterize what controlled the accuracy and variance of pMC estimates and how far pMC could perturb parameters while obtaining reflectance estimates

that agree with cMC reflectance estimates. Similarly, the motivation to compare dMC sensitivity estimates and d-cMC estimates is to characterize what controls the variance of dMC estimates and how far the user can perturb optical properties and still obtain accurate sensitivity estimates.

Table 4.3: Additional perturbations for dMC.

Baseline Value, α	Perturbed Parameter, $\hat{\alpha}$	Increment of Perturbed Parameter
$\bar{r}_2$=0.45 μm	$\hat{\bar{r}}_2$=0.44-0.46 μm	0.002 μm
$\bar{r}_3$=4.8 μm	$\hat{\bar{r}}_3$=4.7-4.9 μm	0.02 μm
$N_{s,2}$= 5.00 $\times 10^{10}$	$\widehat{N}_{s,2}$= 4.5 $\times 10^{10}$-5.5 $\times 10^{10}$cm^{-3}	1.0 $\times 10^{9}$cm^{-3}
$N_{s,3}$= 5.00 $\times 10^{8}$	$\widehat{N}_{s,3}$= 4.5 $\times 10^{7}$-5.5 $\times 10^{7}$cm^{-3}	1.0 $\times 10^{6}$cm^{-3}

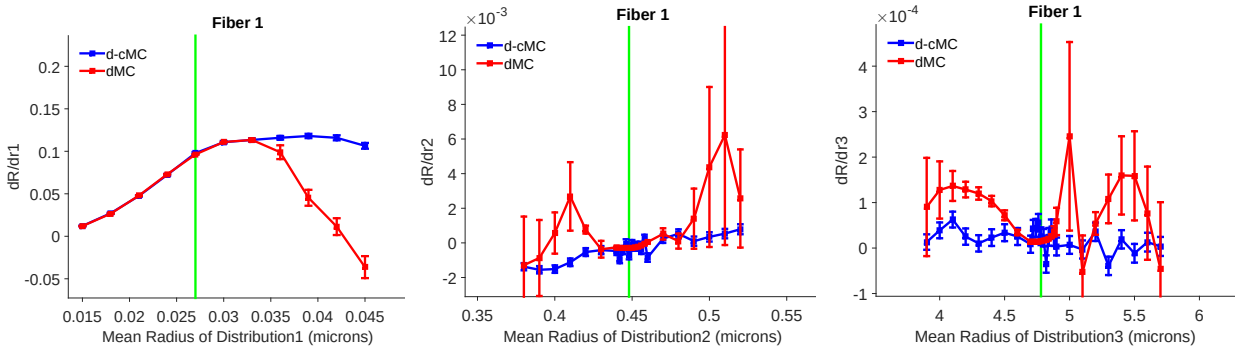

Figure 4.1: d-cMC and dMC comparisons across radii perturbations for unpolarized light simulations.

Figure 4.1 shows estimates of the sensitivity of the reflectance with respect to each of the three mean radii for the case of unpolarized light. The plots in Fig. 4.1 show a comparison between dMC and d-cMC data points. Since d-cMC data points represent calculations of the derivative with no perturbation applied and dMC data points represent calculations of the derivative with a non-zero perturbation, d-cMC estimates should be more accurate than dMC estimates. Similar to the vertical green lines in Fig. 3.12, the vertical green lines in Fig. 4.1 mark the baseline mean radius value of all dMC points in that particular plot. For the perturbations of the mean radii of the second and third distributions in fig. 4.1, the estimates of the derivative with respect to the mean radii are smaller than or approximately equal to the size of the standard error of the estimate for d-cMC and dMC calculations. This indicates that the derivative values for reflectance with respect

to the mean radii of the second and third distributions are effectively zero and that this virtual probe is not sensitive to these distributions, a result that parallels the rates of change of reflectance in Fig. 3.7. Furthermore, the estimate of the derivative obtained through dMC conforms to dMC estimates of the derivative for $\widehat{\bar{r}}_1$ between 0.015 - 0.033 microns, for $\widehat{\bar{r}}_2$ between 0.43 - 0.48 microns and $\widehat{\bar{r}}_3$ between 4.6 - 4.9 microns**.**

Comparing the Fig. 4.1 and Fig. 3.7 together, it appears that the size of the confidence interval of pMC's estimate for any particular perturbation is roughly proportional to the size of the confidence interval for dMC's estimate. It is interesting to note that we found that the difference between the magnitude of the standard deviation of pMC and the magnitude of the expected value of pMC was always about one magnitude greater than the difference between the standard deviation of dMC and the magnitude of the expected value of dMC for the same perturbation and the same photon biography. In other words, however "noisy" the estimate of pMC was, we could reliably expect the estimate of dMC to be about one magnitude "noisier." We found this relationship to be upheld for all perturbations, without exception. This can likely be explained by the fact that dMC equations are the derivatives of pMC equations and that taking the derivative tends to make noisy signals even noisier.

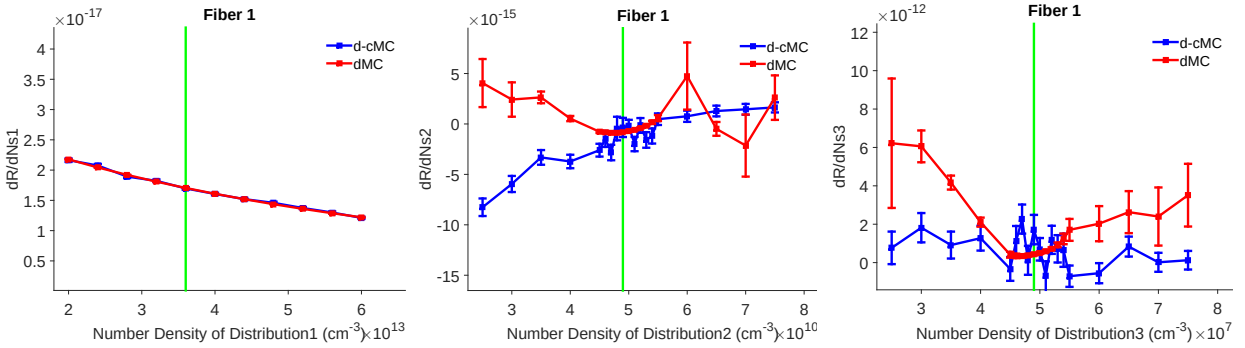

Figure 4.2: d-cMC and dMC comparisons across number density perturbations for unpolarized light simulations.

Figure 4.2 shows a comparison between dMC and d-cMC estimates of reflectance for perturbations in the number density. Perturbations in number density do not result in a change in the phase

function and do not result in a change in the aniostropy factor. These plots show high sensitivity to the first number dneisty, but relatively low sensitivity to the other distributions. The estimate of the derivative obtained through dMC agrees with d-cMC estimates of the derivative for $\widehat{N}_{s,1}$ $=2\times10^{13}-6\times10^{13}$ cm^{-3}, for $\widehat{N}_{s,2}$ $=4.5\times10^{10}-5.5\times10^{10}$ cm^{-3} and $\widehat{N}_{s,3}$ $=4.5\times10^{7}-5.5\times10^{7}$ cm^{-3}.

4.1.6 dMC results Performance with Polarized Light

Figure 4.3 and 4.4 show dMC estimates alongside with d-cMC estimates of the derivatives dR/dr_1 and dR/dr_2. Agreement between dMC and d-cMC is strong for $\widehat{\bar{r}}_1$ between 0.015 – 0.033 microns and $\widehat{\bar{r}}_2$ between 0.44 – 0.47 microns for all detectors. The range for accurate dMC estimates for the derivative when using polarized light are similar to the range of accurate dMC estimates of the derivative when using unpolarized light. An interesting thing to note from the plots in Fig. 4.4 is that the polarized reflectance appears to be sensitive to the second mean radius. This matches previous results in Chapter 3 that indicate that polarized reflectance may be sensitive to the parameters involving the second distribution and is an encouraging result, since changes in the second distribution are associated with dysplasia [20]. Furthermore, sensitivity estimates for perpendicular polarization appears to consistently have larger error bars for the same detector and at the same perturbation; this appears to be an artifact of the poorer relative errors the perpendicular reflectance recieves and is an extension of the physics of this problem. Essentially, fewer photons polarized perpendicular to the x-axis reach each detector than photons polarized parallel to the x-axis, which results in larger variances for reflectance estimates at the baseline. Larger variances at the baseline optical properties for reflectance estimates then translate to even larger variances in dMC estimates for photons polarized perpendicular to the x-axis in each detector. The dMC and d-cMC comparison between sensitivity estimates for the number density are omitted here in the interest of brevity, but the results indicate similar findings about the nature of dMC.

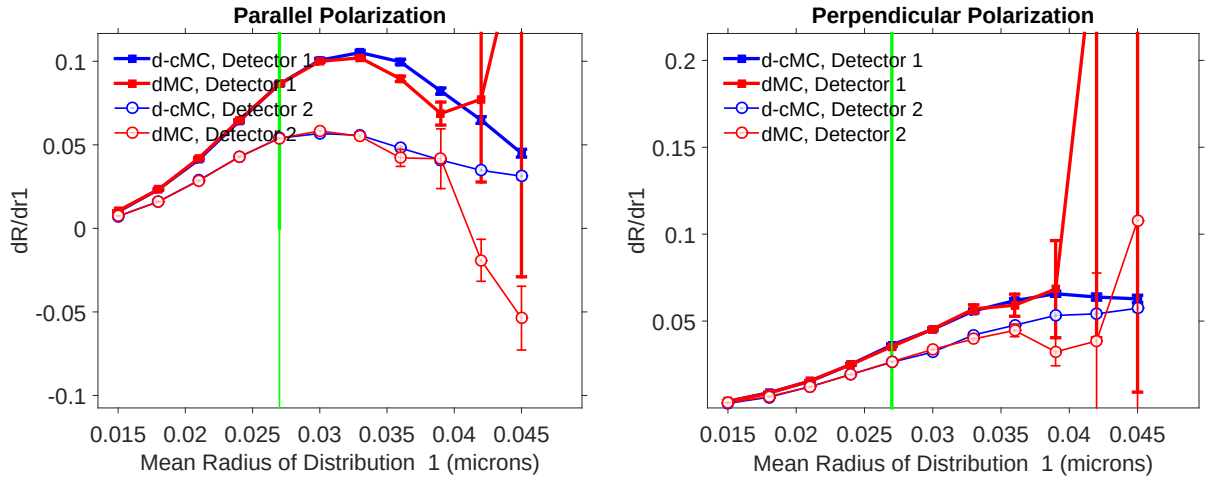

Figure 4.3: Comparisons of d-cMC and dMC estimates of reflectance across perturbations of the mean radius of the first distribution for polarized light propagation.

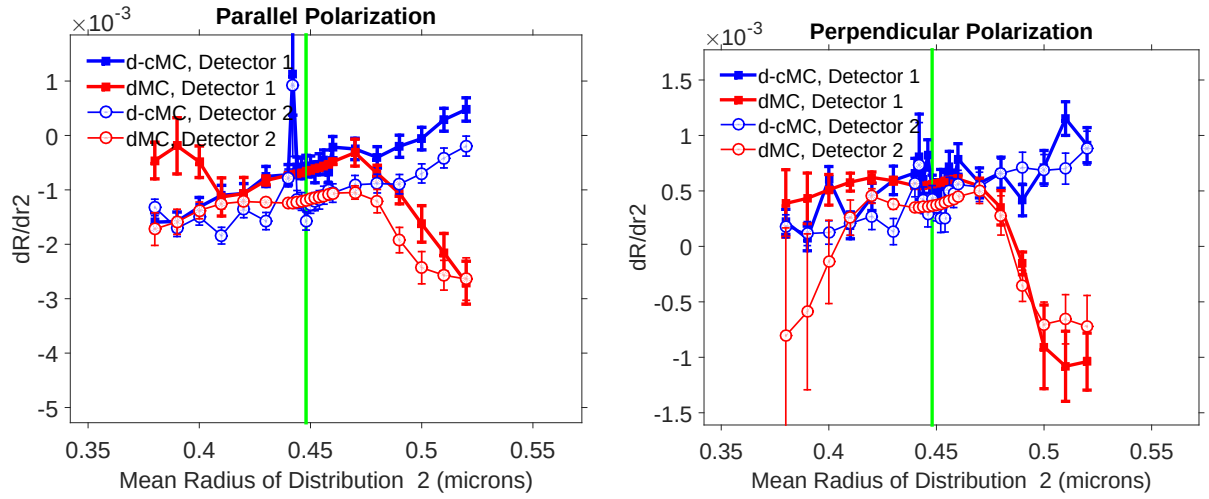

Figure 4.4: d-cMC and dMC estimates of reflectance across perturbations of the mean radius of the second distribution for polarized light propagation.

Chapter 5

Inverse Problem Solutions

In this chapter, we examine the potential to use our forward model as a means to recover the number density and size of tissue scatterers from a set of unpolarized or polarized reflectance measurements. Inverse problems are defined as the process of using a set of measurements and a pre-determined mathematical model to determine the quantity of each causal factor that a model accounts for. Generally, inverse problems are useful because they can quantify properties of a material that are necessary to predict an actual experimental measurement in a manner consistent with an assumed physical model. Inverse problems are also considered to be more difficult to resolve than forward problems for several reasons: 1) inverse problems can be ill-posed, meaning that different values of the model parameters may be consistent with the same measurements and 2) optimization of the model parameters can sometimes requires examination of a large parameter space. Furthermore, even if a problem is not ill-posed, small errors in measurement data can result in much larger errors in the estimates of the parameter values. There are a host of tools that help one overcome the difficulties of solving inverse problems. Discussion of various inverse problem solving techinques are outside the scope of this dissertation, but the author has found Engl's book and Sze Tan's website helpful starting points for learning about this topic [8].

This chapter is organized into several sections four separate sections. In the first section, we lay out the theoretical framework of the inverse problem in terms of an optimization problem. In the second section, we apply this framework to solve an inverse problem, considers using a set of unpolarized reflectance measurements to recover model parameters (mean radii and number densities of three scatterer populations). In the third section, we apply the same framework to examine the ability of polarized reflectance measurements to recover the same sets of model parameters. In these cases we attempted to recover two of six parameters simultaneously using measurements taken at five wavelengths. This examination focused on determining measurements that would be sensitive to changes in mean radii for the two smallest scatterer distributions, which are indicative of pre-tumorigenic changes. Finally, in the fourth section, we discuss the strengths and weaknesses of our method.

Briefly, I would like to explain the motivations for each chapter. Our initial test of pMC's inverse problem solving capabilities for unpolarized reflectance measurements were much simpler in nature than our tests of its inverse problem solving capabilities for polarized reflectance measurements and were motivated by "proof-of-concept" and code debugging. In the case of testing pMC's inverse problem solving capability using unpolarized reflectance measurements, only one parameter of the scattering model was recovered at a time, while the other five parameters were fixed. When pMC's inverse problem solving capability was tested with polarized reflectance measurements, we were motivated to solve problems similar to ones commonly encountered by clinicians [25]. We were particularly interested in answering this question: is it possible to use pMC in combination with reflectance measurements from fiber optic probes to determine micro-architectural changes in tissue? We were aware of previous research that has successfully used perturbation Monte Carlo to determine bulk optical properties such as the scattering coefficient μ_s, the anisotropy factor g, or the absorption coefficient μ_a. We are also aware of researchers using primarily instrumentation methods to efforts to obtain micro-architectural information; we were interested in developing a somewhat unique method that uses a primarily modeling-based approach to get at subcellular tissue information. Furthermore, we were also interested in seeing if

our algorithm could successfully recover changes in tissue micro-structure, a task which had never been done before with the pMC method.

5.1 Inverse Problem Equations

Let $R_{meas}(\lambda_i)$ be the measured reflectance at i = 1,...,M wavelengths. Suppose we wish to find the optimal values of the number densities andmean radii that best match the measured data, i.e., we have six optimization parameters: $\widehat{N}_{s,1}, \widehat{N}_{s,2}, \widehat{N}_{s,3}, \widehat{\bar{r}}_1, \widehat{\bar{r}}_2, \widehat{\bar{r}}_3$. Let $\widehat{R}(\lambda; N_{s,1}, N_{s,2}, N_{s,3}, \widehat{\bar{r}}_1, \widehat{\bar{r}}_2, \widehat{\bar{r}}_3)$ be the pMC approximation of reflectance. A least-squares minimization for finding the optimal parameter set $\widehat{N}^*_{s,1}, \widehat{N}^*_{s,2}, \widehat{N}^*_{s,3}, \widehat{\bar{r}}^*_1, \widehat{\bar{r}}^*_2, \widehat{\bar{r}}^*_3$ is equivalent to finding the minimum of the following function:

$$\chi^2(\widehat{N}_{s,1}, \widehat{N}_{s,2}, \widehat{N}_{s,3}, \widehat{\bar{r}}_1, \widehat{\bar{r}}_2, \widehat{\bar{r}}_3) = \sum_{i=1}^{M} \frac{\left[R_{meas}(\lambda_i) - \widehat{R}(\lambda; \widehat{N}_{s,1}, \widehat{N}_{s,2}, \widehat{N}_{s,3}, \widehat{\bar{r}}_1, \widehat{\bar{r}}_2, \widehat{\bar{r}}_3)\right]^2}{Var[R_{meas}]} \tag{5.1}$$

The problem of minimizing the value of this function is also known as a least-squares problem. There are many strategies that are employed to minimize the value of the χ^2 function, which include: gradient-descent methods, the singular value decomposition, QR decomposition, etc. For our problem, we chose the Levenberg-Marquardt Algorithm, a non-linear optimization method that combines the method of gradient descent and Gauss-Newton Algorithm, a modification of Newton's method for finding the minimum of a function.

5.1.1 Levenberg-Marquardt Algorithm

The Levenberg-Marquardt Algorithm is an iterative algorithm used to solve least squares problems such as the problem of minimizing the function in Eq. (5.1). Let $f(x_i, \beta + \delta)$ be the model function and y_i be the vector of measurement data. At each iteration, the parameter vector β is updated with a new estimate, $\beta + \delta$. To determine δ, the model function $f(x_i, \beta + \delta)$ is approximated by this

linearization:

$$f(x_i, \beta + \delta) \approx f(x_i, \beta) + J_i \delta, \tag{5.2}$$

where $J_i = \frac{\partial f(x_i, \beta)}{\partial \beta}$ is the gradient of f with respect to β. The sum $S(\beta)$ of square deviations has at its minimum a zero gradient with respect to β. The above first-order approximation of $f(x_i, \beta + \delta)$ gives

$$S(\beta + \delta) \approx \sum_{i=1}^{m} (y_i - f(x_i, \beta) - J_i \delta)^2 = \chi^2(\beta) \tag{5.3}$$

Taking the derivative of $S(\beta + \delta)$ with respect to δ and setting the result to zero then yields

$$(J^T J)\delta = J^T [y - f(\beta)] \tag{5.4}$$

where J is the Jacobian matrix whose i-th row equals J_i, and where f and y are vectors with i-th component $f(x_i, \beta)$ and y_i respectively. This is a set of linear equations, which can be solved for δ. Levenberg and Marquardt's contribution to this is the damping factor:

$$\left[J^T J + \lambda I(J^T J)\right] \delta = J^T [y - f(\beta)] \tag{5.5}$$

where I is the identity matrix, giving as the increment δ to the estimated parameter vector β. This damping factor adjusts behavior of the algorithm to react in ways that are more similar to the Gauss-Newton algorithm or more similar to gradient descent. Furthermore, this damping factor is scaled to the size of each component. This avoids the problem of slow convergence in the direction of small gradients; this problem can occur when parameters vary by several orders of magnitude.

5.2 Unpolarized Reflectance Measurements and Parameter Optimization Experiments

This section contains our first explorations with pMC's inverse problem solving capabilities using unpolarized light reflectance measurements. In a typical biomedical inverse problem solving scenario, a practitioner of a method would be aware of several things: the geometry and the characteristic output of the device used in optically probing a region of tissue. The value of certain tissue characteristics, which may or may not be dependent on the model chosen by the investigator, would be unknown before hand. The tests described in this section also abides by these constraints. First, we generated reflectance measurements using various values for our model parameters, mean radii and number density. Next, we then used those reflectance measurements as inputs to our pMC method in order to recover model parameter values. The efficacy of our pMC method's inverse problem solving capabilities are then evaluated by comparing the "actual" parameter values, which are taken from the parameter values used to generate the reflectance measurements in the first place, with the "optimized" parameter values, which is the output of the pMC method used in an inverse problem solving manner.

5.2.1 Generation of Unpolarized Reflectance Measurements

In order to test out our method's efficacy, we first had to generate data sets of unpolarized reflectance measurements, which would be used in inverse problem solving later. All reflectance measurements were obtained by running a Monte Carlo simulation, as described in Chapter 3, on a tissue in which there were 3 lognormally distributed groups of spherical Mie scatterers. The mean radii and number densities of the scatterers embedded in the tissue were varied from the baseline values in Table 2.1. The various combinations of mean radii and number density values for the sample unpolarized reflectance measurement sets are shown below in Table 5.1. These reflectance

measurements were generated for the probe geometry described in Figure 2.1 at a wavelength of 620 nm. We picked this probe configuration because it closely mirrored a probe design used in prior studies [22]. Recall that the center-to-center distance between Detector 1 and the source fiber is the same as the center-to-center distance between Detector 2 and the source fiber. This means that for unpolarized light, the reflectance at Detector 1 and Detector 2 should be statistically similar and that there is only one independent measurement for each wavelength of light emitted. Because of this, we elected to only recover one parameter at a time for each measurement. Now, in order to obtain the actual reflectance measurement for this probe geometry and specific tissue scattering model, we launched 20 million photons in a conventional Monte Carlo simulation for each set of parameter values in Table 5.1. These simulations were run on the cores of University of California, Irvine's High Performance Cluster and took between 13 - 82 minutes to run.

Table 5.1: Combinations of of parameter values used to generate unpolarized reflectance measurements

Floated	Fixed	Range for Floated Param.	Param. Increments
$\widehat{\bar{r}}_1$	$\widehat{\bar{r}}_2, \widehat{\bar{r}}_3, \widehat{N}_{s,1}, \widehat{N}_{s,2}, \widehat{N}_{s,3}$	0.015 – 0.045 μm	0.003 μm
$\widehat{\bar{r}}_2$	$\widehat{\bar{r}}_1, \widehat{\bar{r}}_3, \widehat{N}_{s,1}, \widehat{N}_{s,2}, \widehat{N}_{s,3}$	0.38 – 0.52 μm	0.01 μm
$\widehat{\bar{r}}_3$	$\widehat{\bar{r}}_1, \widehat{\bar{r}}_2, \widehat{N}_{s,1}, \widehat{N}_{s,2}, \widehat{N}_{s,3}$	3.9 – 5.7 μm	0.1 μm
$\widehat{N}_{s,1}$	$\widehat{\bar{r}}_1, \widehat{\bar{r}}_2, \widehat{\bar{r}}_3, \widehat{N}_{s,2}, \widehat{N}_{s,3}$	2×10^{13} – 6×10^{13} cm^{-3}	4×10^{12} cm^{-3}
$\widehat{N}_{s,2}$	$\widehat{\bar{r}}_1, \widehat{\bar{r}}_2, \widehat{\bar{r}}_3, \widehat{N}_{s,1}, \widehat{N}_{s,3}$	2.5×10^{10} – 7.5×10^{10} cm^{-3}	5×10^{9} cm^{-3}
$\widehat{N}_{s,3}$	$\widehat{\bar{r}}_1, \widehat{\bar{r}}_2, \widehat{\bar{r}}_3, \widehat{N}_{s,1}, \widehat{N}_{s,2}$	2.5×10^{7} – 7.5×10^{7} cm^{-3}	5×10^{6} cm^{-3}

5.2.2 Optimization

Proper utilization of the pMC and dMC method requires the user to generate a set of collected photon biographies by running a "mother" simulation. The mother simulation was run by launching 2 billion virtual photons through the probe configuration in Fig. 2.1 into a medium with the baseline optical properties in Table 2.1. We chose to launch a very high number of photons to obtain more accurate dMC estimates and to obtain better parameter optimizations. With optimization, only one

parameter was allowed to vary, while the other five parameters were fixed at proper values. The simulations used to generate the reflectance measurements can be separated into six categories: 1) simulations where the mean radius of the first scatterer population is allowed to vary from the baseline, 2) simulations where the mean radius of the second scatterer population is allowed to vary from the baseline, and so on for the other four parameters... In every instance of parameter optimization, the parameter that was floated was matched to the category in which the reflectance measurement came from. In other words, if the reflectance measurement was generated using a simulation in which the mean radius of the first distribution was different from the baseline, optimization was performed in such a way that the value for the first mean radius was floated and other parameter values were fixed. Figure 5.1 shows the results of this experiment.

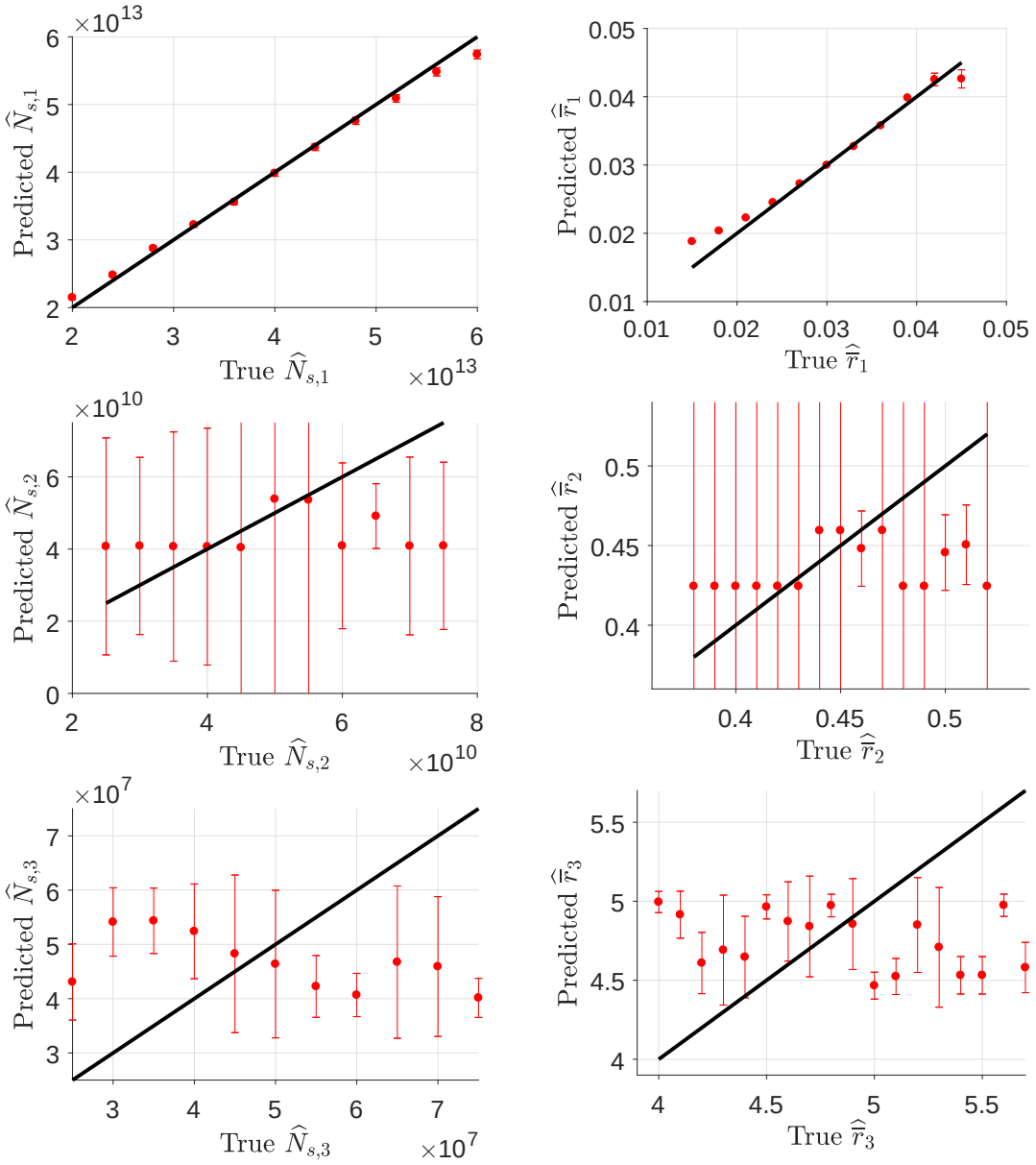

Figure 5.1: Comparison of parameter values used to generate virtual measurement data vs. optimized model parameer values obtained by inputting measurement data into optimization algorithm powered by pMC. Black sloped line indicates a perfect fit of the measurement data.

From Figure 5.1, we see that recovery of number density and mean radii of the first distribution are within 10% of actual parameter values for all parameter values tested. For the number density and mean radii of the second distribution, recovered parameter values are within 10% of actual parameter values between $N_{s,2} = 4 \times 10^{10} - 5.5 \times 10^{10}$ cm^{-3} and $\bar{r}_2 = 0.39 - 0.49$µm, but accuracy

of recovered parameter values break down outside of these ranges. This in part is due to the much larger changes in the scattering coefficient, $\overline{\mu}_s$ and the lower sensitivity to the second distribution, as described in our sensitivity analysis using dMC estimates. Finally for the third distribution, recovery of parameter values is poor for both mean radii and number density for any parameter value away from the baseline. This poor recovery is a result of the very low sensitivity to the third distribution, which agrees with previous dMC estimates of sensitivity. We conclude that accuracy of parameter optimization is affected by a) sensitivity to that parameter and b) change in scattering coefficient. Larger changes in scattering coefficient values will result in pMC estimates with larger variances and result in more difficult optimization and possibly poorer parameter recovery. Poor sensitivity (that is, if the dMC estimate of the sensitivity is very close to zero) to parameters will also result in poor parameter recovery.

5.2.3 Polarized Reflectance

In this section, we summarize exploration of with pMC's inverse problem solving capabilities using polarized reflectance measurements. We consider the same experimental arrangement as in Section 5.2.2 except that we use linearly polarized light to illuminate the tissue sample and detect both the co- and cross-polarized reflectance signals. For these experiments, we allowed two parameters of the six total model parameters to stray from the baseline values. The two model parameters that were allowed to stray from baseline values were then floated during optimization of parameter values while others were fixed at baseline values.

5.2.4 Generation of Polarized Reflectance Measurements

We first had to generate data sets of polarized reflectance measurements, which would be used in inverse problem solving later. All reflectance measurements were obtained by running a light transport simulation on a tissue in which there were 3 lognormally distributed groups of spherical

Mie scatterers. The mean radii and number densities of the scatterers embedded in the tissue were varied from the baseline values in Table 2.1. The various combinations of mean radii and number density polarized reflectance measurement sets are shown below in Table 5.2. These reflectance measurements were generated for the probe geometry described in Figure 2.1 at a wavelength of 500, 520, 560, 640, 720 nm. We picked these wavelengths because these wavelengths were the most sensitive to changes in the second distribution and are within the range of emitted wavelengths of our collaborator's actual probe. To generate the reflectance measurements we launched 800 million photons in a conventional Monte Carlo simulation for each wavelength for each set of parameter values in Table 5.1. These simulations were also run on the cores of University of California, Irvine's High Performance Cluster.

Table 5.2: Combinations of of parameter values used to generate unpolarized reflectance measurements

Floated Parameter	Floated Parameter Range	Increment
$\widehat{\bar{r}}_1$	0.015 – 0.045 μm	0.006 μm
$\widehat{\bar{r}}_2$,	0.38 – 0.52 μm	0.03 μm
$\widehat{N}_{s,1}$	$2 \times 10^{13} - 6 \times 10^{13}$ cm^{-3}	1.00×10^{13} cm^{-3}
$\widehat{N}_{s,2}$	$2.5 \times 10^{10} - 7.5 \times 10^{10}$ cm^{-3}	1.25×10^{10} cm^{-3}

5.2.5 Optimization

The mother simulation was run by launching 2 billion virtual photons through the probe configuration in Fig. 2.1 into a medium with the baseline optical properties in Table 2.1. We chose to launch a very high number of photons to help obtain more accurate dMC estimates and to help obtain better parameter optimizations. With optimization, only one parameter was allowed to vary, while the other five parameters were fixed at proper values. The simulations used to generate the reflectance measurements can be separated into six categories: 1) simulations where the mean radius of the first scatterer population, $\widehat{\bar{r}}_1$, is allowed to vary from the baseline, 2) simulations where the mean

radius of the second scatterer population, $\widehat{\bar{r}}_2$, is allowed to vary from the baseline, and so on for the other four parameters. For every instance of parameter optimization, the parameter that was floated was matched to the category in which the reflectance measurement came from. In other words, if the reflectance measurement was generated using a simulation in which the mean radius of the first distribution was different from the baseline, optimization was performed in such a way that the value for the first mean radius was floated and other parameter values were fixed. Figures 5.2–4 provide the results of this experiment. In this next section the results for parameter optimization given polarized reflectance measurements are shown. These results were obtained by generating measurement reflectance estimates using conventional Monte Carlo, in which 20 million photons were launched. The optical properties of the measurement set of cMCs was determined by setting four parameter values at the baseline values described in Table 2.1 and varying two parameter values. Reflectance estimates were obtained at wavelength values of 500, 520, 560, 640, and 720 nm. These wavelengths were picked because they the most sensitive to changes in the second distribution. For optimization, five sets Monte Carlo simulations were run at the baseline optical properties with incident photon wavelengths of 500, 520, 560, 640, 720 nm. In each simulation, we launched 800 million photons into the medium, resulting in a total of 4 billion photons that were launched to generate the collected photon biographies to be used for pMC and dMC calculations. There are several types of optimizations we performed which are summarized in the table below in Table 5.3.

Table 5.3: Types of polarized optimization

Figure Number	Floated Parameters	Fixed Parameters
Fig. 5.2	$\widehat{\bar{r}}_1, \widehat{\bar{r}}_2$	$\widehat{\bar{r}}_3, \widehat{N}_{s,1}, \widehat{N}_{s,2}, \widehat{N}_{s,3}$
Fig. 5.3	$\widehat{N}_{s,1}, \widehat{N}_{s,2}$	$\widehat{\bar{r}}_1, \widehat{\bar{r}}_2, \widehat{\bar{r}}_3, , \widehat{N}_{s,3}$
Fig. 5.5	$\widehat{\bar{r}}_1, \widehat{N}_{s,1}$	$\widehat{\bar{r}}_2, \widehat{\bar{r}}_3, \widehat{N}_{s,2}, \widehat{N}_{s,3}$
Fig. 5.6	$\widehat{\bar{r}}_2, \widehat{N}_{s,2}$	$\widehat{\bar{r}}_1, \widehat{\bar{r}}_3, \widehat{N}_{s,1}, \widehat{N}_{s,3}$
Fig. 5.7	$\widehat{\bar{r}}_1, \widehat{N}_{s,2}$	$\widehat{\bar{r}}_2, \widehat{\bar{r}}_3, \widehat{N}_{s,1}, \widehat{N}_{s,3}$
Fig. 5.8	$\widehat{\bar{r}}_2, \widehat{N}_{s,1}$	$\widehat{\bar{r}}_1, \widehat{\bar{r}}_3, \widehat{N}_{s,2}, \widehat{N}_{s,3}$

The figure below shows the results for optimizing the parameters $\widehat{\bar{r}}_1$ and $\widehat{\bar{r}}_2$. Reflectance measurements were generated by using baseline values for all other model parameters and using values of $\widehat{\bar{r}}_1$ between 0.015 μm and 0.045 μm with increments of 0.003 μm and values of $\widehat{\bar{r}}_2$ between 0.38 μm and 0.52 μm with increments of 0.03μm. Combining the five possible values for $\widehat{\bar{r}}_1$ and the five possible values for $\widehat{\bar{r}}_2$ resulted in a total of 25 sets of reflectance measurements that were used to test the optimization capabilities of our method. Each of the two plots in Fig. 5.2 has 25 plot points, which represent the same 25 optimizations that were performed. The first plot from the left in Fig. 5.2 shows information about optimization regarding the parameter $\widehat{\bar{r}}_1$ where as the second plot from the left in that same figure shows information about optimization regarding the parameter $\widehat{\bar{r}}_2$. As stated before, the optimizations were done in such a way that both parameters were simultaneously optimized; however, information about parameter optimization is shown in different plots due to the difficulty in showing optimization for the two parameters in the same plot. For these optimizations, the run time took between 15 - 36 hours. Each optimization took between 4-10 iterations of the Levenberg-Marquardt Algorithm, with a user set limit of a maximum of 10 iterations. Early optimization experiments on this set of reflectance measurements showed that for the most part, the step size for parameters were less than 1% of the previous parameter value after 10 iterations. (We had originally set the maximum number of LMA iterations to 25, which resulted in much longer run times for optimization problems.) It should also be noted that each iteration of the LMA did not necessarily correspond to one evaluation of the pMC and dMC functions. Oddly, certain iterations called for multiple evaluations of pMC and dMC functions and other iterations did not call for evaluations of dMC functions at all. Correlation between $\widehat{\bar{r}}_1$ and $\widehat{\bar{r}}_2$ were evaluated using the elements of the covariance matrix as shown below.

$$cor_{i,j} = \frac{C_{i,j}}{\sqrt{C_{i,i}}\sqrt{C_{j,j}}} \tag{5.6}$$

where $cor_{i,j}$ is the correlation between the ith and jth parameter and $C_{i,j}$ is an element in the covariance matrix in the ith row and jth column which describes covariance between a total of n

parameters:

$$C = \begin{bmatrix} C_{1,1} & C_{1,2} & \dots & C_{1,n} \\ C_{2,1} & C_{2,2} & \dots & C_{2,n} \\ \vdots & \vdots & & \vdots \\ C_{n,1} & C_{n,2} & \dots & C_{n,n} \end{bmatrix}. \tag{5.7}$$

Correlation between the parameters $\widehat{\bar{r}}_1$ and $\widehat{\bar{r}}_2$ ranged between -0.843 and 0.606, with the closest value to zero at 0.014. Correlation values equal zero indicate that parameter values are independent of one another and correlation values equal to -1 (negative correlation) or 1 (positive correlation) indicate that the two parameters are not independent of one another. Correlation values close to 1 or -1 mean that the two parameters are closely related and the user may experience some difficulty optimizing for those parameters simultaneously. To measure the efficacy of parameter optimizations, we utilized relative errors:

$$rel.err. = \frac{|\alpha^{\star} - \alpha|}{\alpha} \times 100\% \tag{5.8}$$

where $\alpha\star$ is the value of the parameter output by the optimization process and α is the true value of the parameter used to generate the reflectance measurement. The relative errors of optimizations of $\widehat{\bar{r}}_1$ were between 0.0281% and 18.7% with an average relative error of 3.35% across all 25 optimizations and the relative errors for optimizations of $\widehat{\bar{r}}_2$ were between 0.101% and 27.9% with an average relative error of 6.01% across all 25 optimizations. In general, optimizations for $\widehat{\bar{r}}_1$ recovered values closer to true values than $\widehat{\bar{r}}_2$. We attribute the reason for this to the higher sensitivity to the first mean radius.

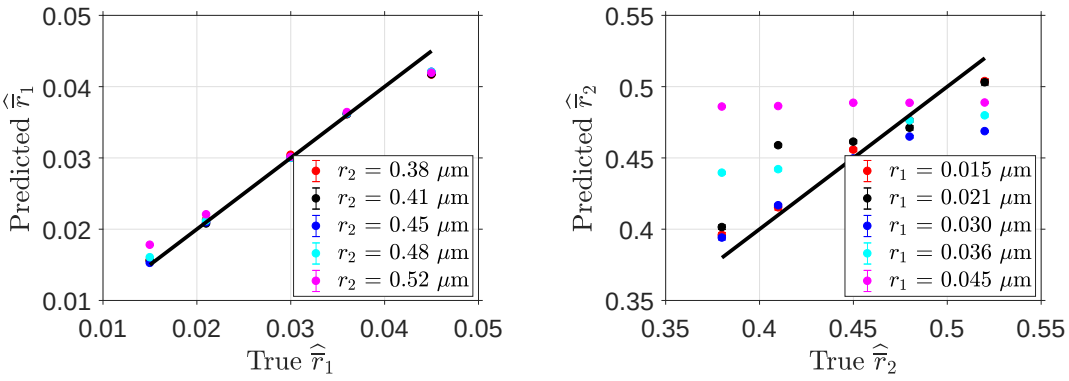

Figure 5.2: Plots of optimized parameter values vs. actual parameter values. The black lines in each plot are $y = x$; plot points that are closer to the black line represent more accurate optimizations that plot points that are further from the black line. Each plot point in this figure represents an optimization where $\widehat{\bar{r}}_1$ and $\widehat{\bar{r}}_2$ were varied and other parameters were fixed.

In Fig. 5.3, we show the results of simultaneous optimizations for the parameters $\widehat{N}_{s,1}$ and $\widehat{N}_{s,2}$. In these optimizations, the phase function is not perturbed; changes in reflectance are the result in perturbations in the scattering coefficient from the baseline scattering coefficient values. Across all 25 optimizations, average relative error in recovering $\widehat{N}_{s,1}$ was 2.38% and the average relative error in recovering $\widehat{N}_{s,2}$ was 6.9%. These optimizations took between 8.84 – 21.8 hours and took between 4 – 10 iterations of the LMA algorithm to complete. The relative error in recovering $\widehat{N}_{s,1}$ and $\widehat{N}_{s,2}$ is lower on average than recovering $\widehat{\bar{r}}_1$ and $\widehat{\bar{r}}_2$. This can be explained by the lower range in scattering coefficient perturbations when perturbing $\widehat{N}_{s,1}$ and $\widehat{N}_{s,2}$ as opposed to perturbing $\widehat{\bar{r}}_1$ and $\widehat{\bar{r}}_2$ as well as the perturbation in phase function that occurs when mean radii is perturbed. Fig. 5.4 shows the comparison between the most extreme perturbations for these two sets of perturbations; the most extreme perturbations of $\widehat{\bar{r}}_1$ and $\widehat{\bar{r}}_2$ result in further perturbations from the baseline in $\widehat{\bar{\mu}_s}$. Since reflectance measurements obtained by perturbing $\widehat{\bar{r}}_1$ and $\widehat{\bar{r}}_2$ represent a more extreme perturbation in the scattering coefficient, the pMC method obtains reflectance estimates with higher variance; this in turn, translates to poorer recovery of model parameters for optimizations in $\widehat{\bar{r}}_1$ and $\widehat{\bar{r}}_2$. Furthermore, perturbations in $\widehat{\bar{r}}_1$ and $\widehat{\bar{r}}_2$ also perturb the phase function where as perturbations in $\widehat{N}_{s,1}$ and $\widehat{N}_{s,2}$ leave the phase function unchanged. This also contributes to the lower relative error in recovery of the parameters $\widehat{N}_{s,1}$ and $\widehat{N}_{s,2}$.

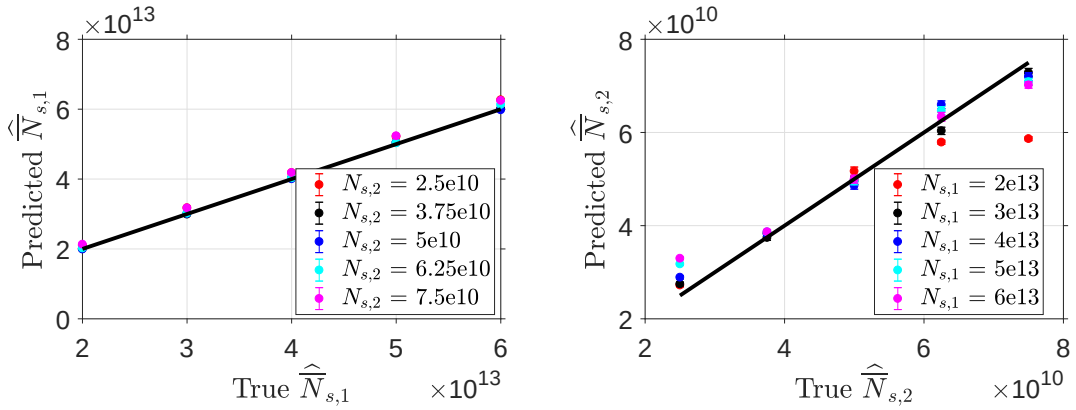

Figure 5.3: Plots of optimized parameter values vs. actual parameter values. The black lines in each plot are $y = x$; plot points that are closer to the black line represent more accurate optimizations that plot points that are further from the black line. Each plot point in the figure represents an optimization where $\widehat{N}_{s,1}$ and $\widehat{N}_{s,2}$ values were varied and other parameters were fixed at the correct values.

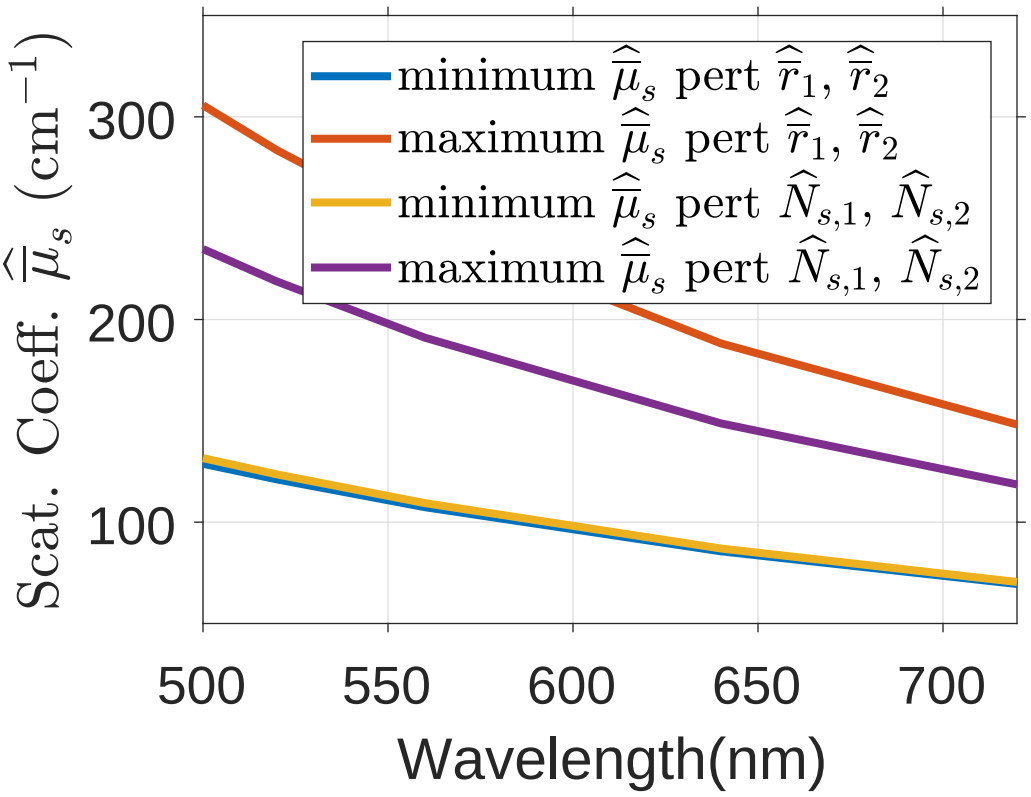

Figure 5.4: Comparison of $\widehat{\overline{\mu}}_s$ values for the most extreme perturbations of $\widehat{\overline{r}}_1$, $\widehat{\overline{r}}_2$ and $\widehat{N}_{s,1}$, $\widehat{N}_{s,2}$.

In Fig. 5.5, we show plot the results of a simultaneous optimization of the parameters $\widehat{N}_{s,1}$ and $\widehat{\overline{r}}_1$. For this set of 25 optimizations, the relative error in recovering $\widehat{\overline{r}}_1$ was 43.7% and the relative error in recovering $\widehat{N}_{s,1}$ was 76.1%. These are poor average relative errors for parameter recoveries. The run time for these optimizations ran from 21 – 33.3 hours with 7 – 10 iterations of the Levenberg-Marquardt Algorithm. The LMA failed to return the correlation between $\widehat{N}_{s,1}$ and $\widehat{\overline{r}}_1$ because of numerical problems. Furthermore, the variance of the parameters were also not returned.

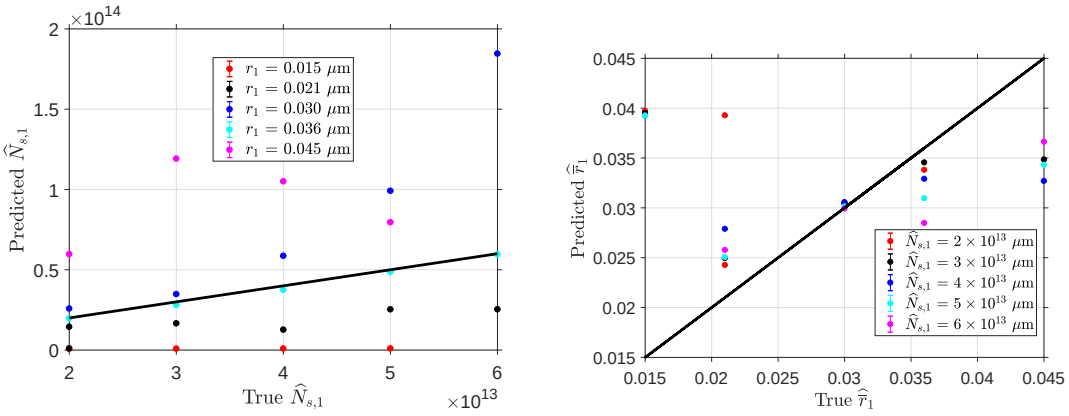

Figure 5.5: Each plot point in this figure represents an optimization where $\widehat{N}_{s,1}$ and $\widehat{\overline{r}}_1$ were varied and other parameters were fixed at their correct values.

In Fig. 5.6, we show results for simultaneous optimization of the parameters $\widehat{N}_{s,2}$ and $\widehat{\overline{r}}_2$. For this set of 25 optimizations, the average relative error in recovering $\widehat{\overline{r}}_2$ was 8.96% and the average relative error in recovering $\widehat{N}_{s,2}$ was 32.2%. The run time for these optimizations 12.5 – 28.7 hours with 2 – 10 iterations of the LMA. The average correlation between $\widehat{N}_{s,2}$ and $\widehat{\overline{r}}_2$ was -0.999. Figure 5.7 shows the results of simultaneously optimizing $\widehat{N}_{s,2}$ and $\widehat{\overline{r}}_1$. On average, the relative error of optimizing $\widehat{\overline{r}}_1$ is 3.00% and the average relative error of optimizing$\widehat{N}_{s,2}$ is 15.3%. The run time for these optimizations was 17.9– 32.8 hours with 6 – 10 iterations of the LMA. The correlation between these two variables on average was -0.281.

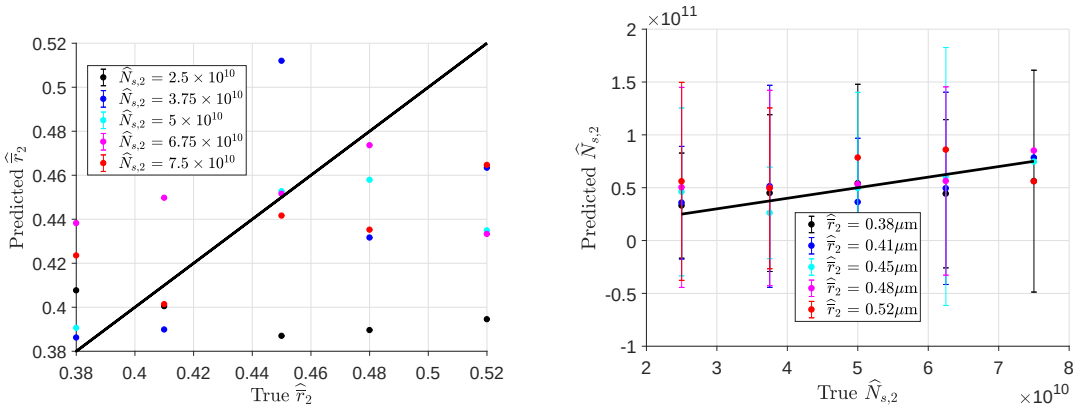

Figure 5.6: Each plot point in this figure represents an optimization where $\widehat{N}_{s,2}$ and $\widehat{\bar{r}}_2$ were varied and other parameters were fixed at their correct values. Plot points closer to the black line represent optimizations where optimized values were closer to actual values.

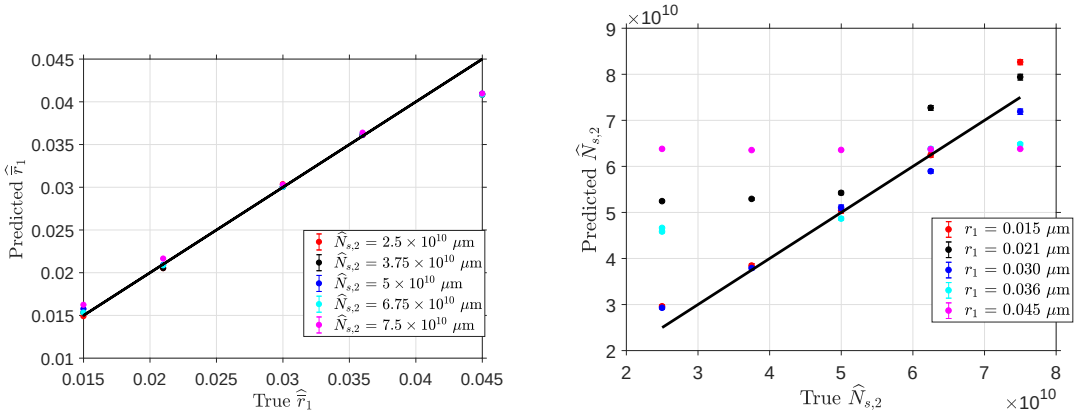

Figure 5.7: Each plot point in this figure represents an optimization where $\widehat{N}_{s,2}$ and $\widehat{\bar{r}}_1$ were varied and other parameters were fixed at their correct values. Plot points closer to the black line represent optimizations where optimized values were closer to actual values.

Figure 5.8 shows the results of simultaneously optimizing $\widehat{N}_{s,1}$ and $\widehat{\bar{r}}_2$. On average, the relative error of optimizing $\widehat{\bar{r}}_1$ is 3.14% and the average relative error of optimizing $\widehat{N}_{s,2}$ is 31.3%. The run time for these optimizations was between 14.4 – 28.6 hours with 4 – 10 iterations of the LMA. The correlation between these two variables on average was -0.0974.

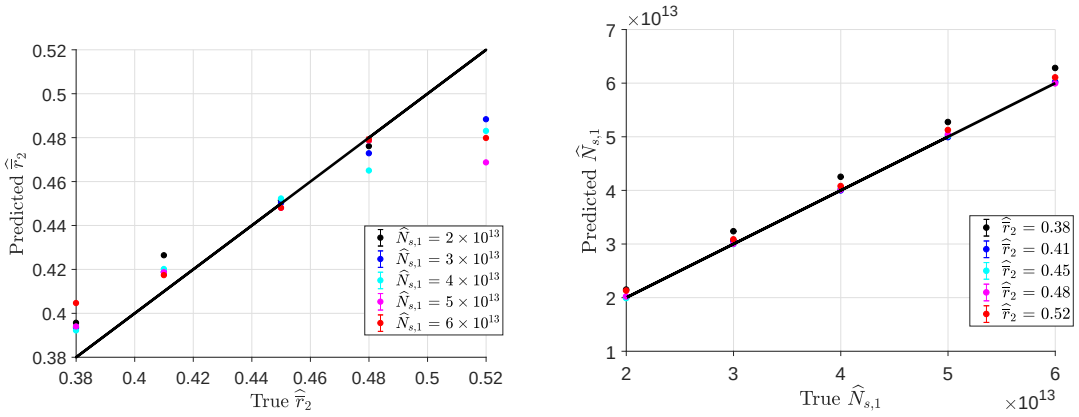

Figure 5.8: Each plot point in this figure represents an optimization where $\widehat{N}_{s,1}$ and $\widehat{\bar{r}}_2$ were varied and other parameters were fixed at their correct values. Plot points closer to the black line represent optimizations where optimized values were closer to actual values.

5.2.6 Discussion

We found that several important factors affect whether or not pMC is able to successfully obtain parameter values. These factors are: the model's sensitivity to its parameters, correlation between other model parameters, changes in scattering coefficient and phase functions.

In Fig. 5.1, we showed results for parameter optimizations for unpolarized reflectance measurements for our probe taken at 620 nm. We know from results in Chapter 4 that unpolarized reflectance measurements at 620 nm are not sensitive to changes in value for parameters involving the second or third scattering populations. This insensitivity to the second and third distribution resulted in very poor results in recovering $\widehat{N}_{s,2}$ and $\widehat{\bar{r}}_2$, $\widehat{N}_{s,3}$ and $\widehat{\bar{r}}_3$ when our method was only given unpolarized reflectance measurements at a wavelength of 620 nm. Relative errors in recovery of $\widehat{N}_{s,3}$ averaged around 38%, with a maximum value of 80% relative error. Similar values were obtained for optimizations of $\widehat{N}_{s,2}$ (maximum relative error of 63% and average relative error of 25.5%), $\widehat{\bar{r}}_2$(maximum relative error of 18.4% and average relative error of 7.31%), $\widehat{\bar{r}}_3$ (maximum relative error of 24.9%, and average relative error of 11.7%). The differences in relative error ranges are different since for these optimizations, the LMA produced parameter values that did not stray far from initial guesses, but the ranges for parameter values used to produce the reflectance

measurements were very different across parameters. For example, both of the number densities were perturbed $\pm$ 50% while $\widehat{\overline{r}}_3$ was perturbed $\pm$18.75% and $\widehat{\overline{r}}_2$ was perturbed $\pm$ 15.6%. We then concluded that low sensitivity was a contributor to the failure to accurately optimized parameter values. Due to this conclusion, we then decided against attempting to optimize for the third parameter value in our optimization experiments with polarized reflectance measurements.

Another conclusion we reached in numerical experiments with optimization was that high correlation between multiple parameters can significantly increase the difficulty in optimizing for those parameters simultaneously. We saw evidence of this when we tried to simultaneously optimize for $\widehat{\overline{r}}_2$, $\widehat{N}_{s,2}$ or when we tried to simultaneously optimize for $\widehat{\overline{r}}_1$ and $\widehat{N}_{s,1}$. In both of these cases relative errors for optimization of these parameters was high (Simultaneous optimization of $\widehat{\overline{r}}_1$ and $\widehat{N}_{s,1}$ resulted in relative errors of 43.7% and 76.1%, respectively. Optimizations of $\widehat{\overline{r}}_2$ and $\widehat{N}_{s,2}$ resulted in relative errors of was 8.96% and 32.2%, respectively.). High correlation between two parameters means that changes in the those two parameters produces changes in reflectance that are similar. If two or more parameters produces similar changes in the model's output, it may be difficult if not impossible to tease apart the effects of the individual parameters that share high correlation. Thus, high correlation between two or more parameters is a contraindicator towards a successful optimization.

One last conclusion we can draw from these results is that extreme changes in scattering coefficient and phase function away from the baseline values will negatively effect the accuracy of the optimization of the parameter values. This makes sense; previous chapters have established that more extreme changes in the optical properties on the medium produce poorer estimates of reflectance from pMC. It stands to reason that poorer pMC reflectance estimates will negatively affect an inverse problem solution powered by pMC estimates. We can see evidence of this effect by closely examining the Figs. 5.8 and 5.7. The set of optimizations performed in both figures represent similar changes in scattering coefficient; the ranges of scattering coefficient values for all these optimizations are shown below in Fig. 5.9; the maximum values for the medium's scattering

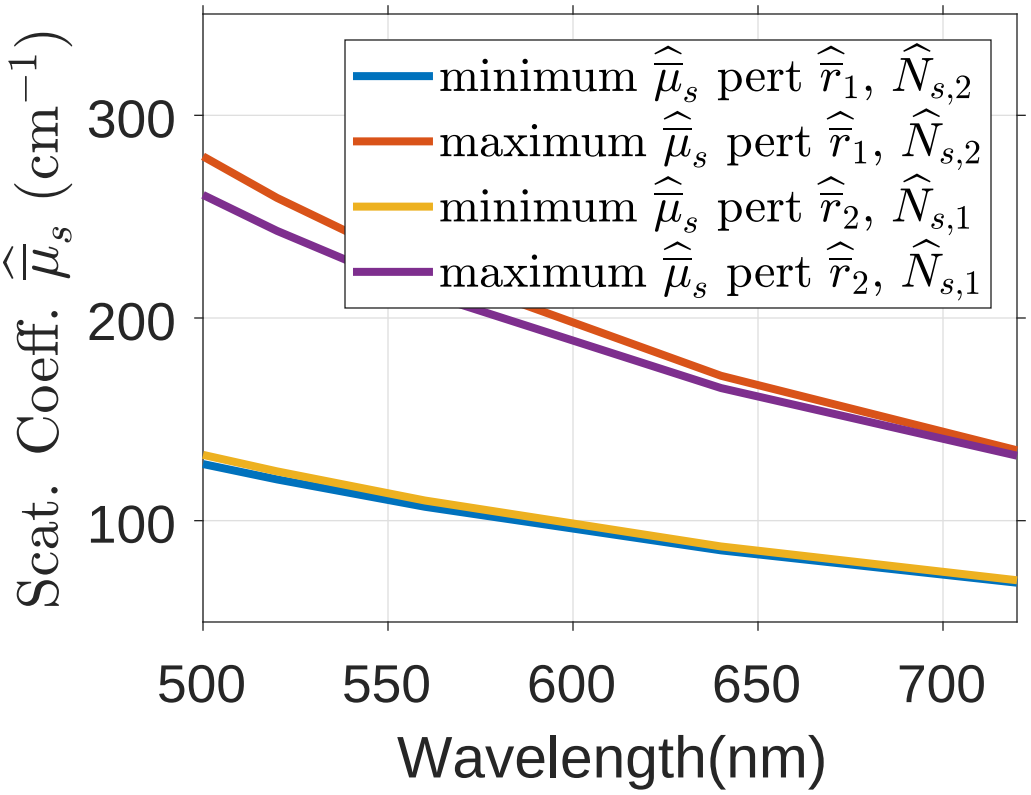

Figure 5.9: Comparison of $\widehat{\bar{\mu}}_s$ values for the most extreme perturbations of $\widehat{\bar{r}}_1$, $\widehat{N}_{s,2}$ and $\widehat{\bar{r}}_2$, $\widehat{N}_{s,1}$.

coefficient values for perturbations involving $\widehat{\bar{r}}_1$ and $\widehat{N}_{s,2}$ always stay within the maximum scattering coefficient values for perturbations involving $\widehat{\bar{r}}_2$ and $\widehat{N}_{s,1}$. Despite having similar ranges in scattering coefficient values, the average relative errors for recovering $\widehat{\bar{r}}_1$ and $\widehat{N}_{s,2}$ are significantly worse than recovering $\widehat{\bar{r}}_2$ and $\widehat{N}_{s,1}$. This is due to the extreme changes in the phase function when perturbing $\widehat{\bar{r}}_1$. From Figure 5.10, we can see that perturbations involving both $\widehat{\bar{r}}_1$ and $\widehat{N}_{s,2}$ span a larger range in the anisotropy factor of the phase function, indicating that phase function changes are more extreme. This more extreme change in phase function then translates to poorer pMC reflectance estimates with and ultimately to poorer recovery of parameter values. For two optimizations involving equal bulk optical properties but different changes in phase function, one can expect that the optimization with smaller changes in phase function will result in more accurate parameter optimization.

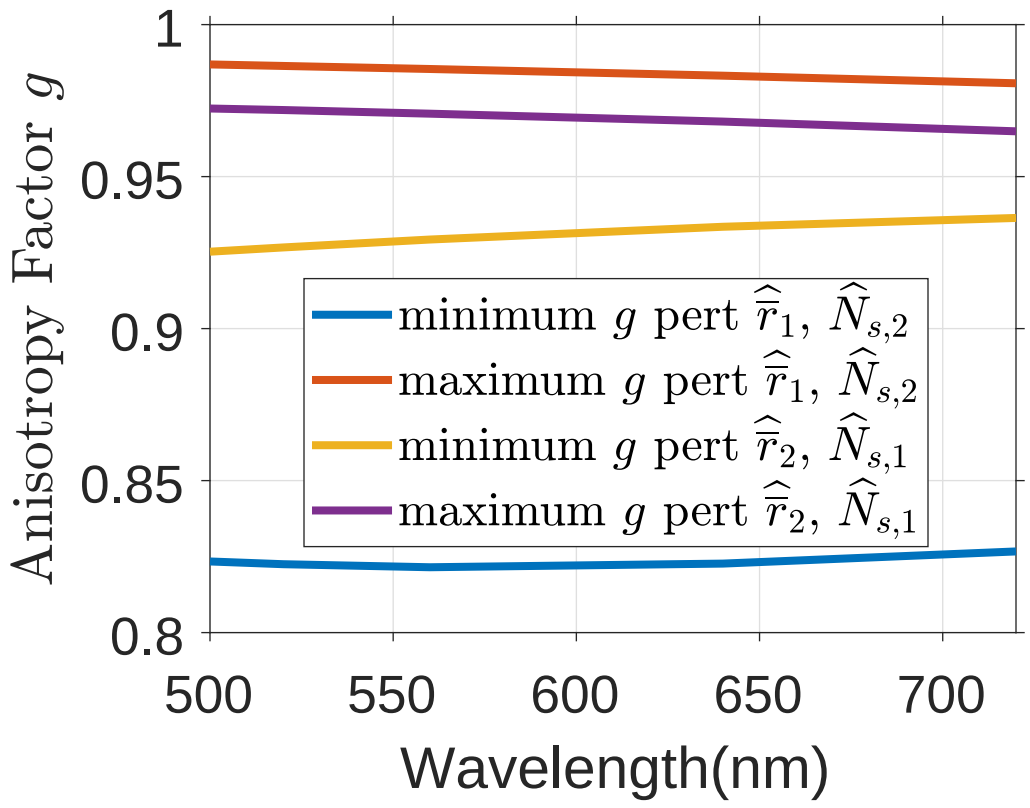

Figure 5.10: Comparison of anistropy factor values for most extreme perturbations of $\widehat{\overline{r}}_1$, $\widehat{N}_{s,2}$ and $\widehat{\overline{r}}_2$, $\widehat{N}_{s,1}$.

5.2.7 Summary

In this chapter, we showed several key results involving our experiments with the pMC method applied to inverse problem solving. We were able to show that the pMC method was sensitive to the parameters involving the first scatterer distribution when utilizing only unpolarized light. We were also able to recover parameters related to the smallest scattering distribution and the second smallest scattering distribution, which relates to protein complexes and organelles. Recovering parameters related to the second scattering distribution is of particular importance since changes in this second distribution are related to dysplastic changes in tissue. While it is possible to recover parameters individually, there are several conditions that must be met for a successful recovery. First, it may be difficult to recover parameters that relate to the same scatterer population simultaneously due to high correlation. This may be alleviated in the future by applying pMC to a realistic, yet simpler model of scattering in tissue. Second, successful recovery is highly dependent on the model's sensitivity to the parameter. Finally, extreme changes in the scattering coefficient and/or the phase function will degrade the quality of reflectance estimates.

Chapter 6

Summary and conclusion

This dissertation shows the author's exploration of the perturbation Monte Carlo method and differential Monte Carlo method. In the third chapter of this dissertation, an implementation of the pMC method was applied to several problems. One problem involved a single sized distribution of Mie scatterers and another problem involved a scattering model composed of three lognormal distributions of Mie scatterers that approximates cervical tissue optical properties. This application of the pMC method is the very first application of a perturbation Monte Carlo method that accounts for changes in phase function. Previous implementations of pMC only accounted for changes in bulk optical properties (the scattering coefficient of the medium μ_s or the absorption coefficient μ_a) but not changes in phase function. This implementation of the pMC method was also unique because it gave the user access to parameters associated with specific scatterers present in tissue. The pMC method was able to yield reflectance estimates within 1% of of conventional Monte Carlo reflectance estimates for changes in parameters that resulted in a 15% change in the bulk scattering coefficient. Later sections of the chapter then expanded on this previous work and tested the first application of polarization tracking to a pMC implementation. This chapter also addressed the gains in computational efficiency, which are three orders of magnitude close to the baseline optical properties, as well as the different factors that affect computational efficiency of

pMC, the changes in scattering coefficient and the changes in the phase function.

In fourth chapter, the author explores the application of the differential Monte Carlo method to the tissue scattering model. First, the dMC model's derivative estimates are compared to finite difference method estimates. Next, the author compares dMC derivative estimates with those of d-cMC estimates to help characterize the nature of the dMC estimates away from baseline optical properties. The relative error of dMC derivative estimates was found to be at least one order of magnitude higher than the relative error of pMC reflectance estimates. This can be explained in the following manner: one would expect that taking the derivative of a noisy signal would create an even noisier signal. The other important implication is that if it takes launching N photons to obtain a minimum acceptable level of variance for reflectance estimates in this particular scattering model, then to obtain that same acceptable level of variance for dMC derivative estimates requires on the order of $100N$ photons to be launched. The author also found that dMC relative errors are also affected by changes in phase function and scattering coefficient. Finally, the author also found that dMC derivative estimates also supported the idea that unpolarized reflectance measurements did not have sensitivity to parameters involving the second distribution, but polarized reflectance measurements were indeed sensitive to those parameters.

The fifth chapter uses findings from previous chapters in an attempt to address the inverse problem: the problem of finding optimal parameter values given reflectance measurements. The first presented results involve simulated unpolarized reflectance measurements and optimization of the six parameters. The pMC method used in conjunction with a Levenberg-Marquardt algorithm was able to recover only the parameter that related to the first scatterer population, a result supported by both pMC and dMC results in Chapters 3 and 4. Next, polarized light at several different wavelengths were used to obtain two parameter values simultaneously. The attempts to recover parameter values successful in several cases with the following restrictions in common: 1) the optimized parameters did not have high correlation with one another, 2) that the model was sensitive to the parameters being optimized. With those restrictions in place, one could expect an

optimization that yielded accurate values for optimized parameters. However, large changes in scattering coefficients and phase functions could negative affect pMC reflectance estimates and, in turn, negatively affect parameter optimizations.

The previous paragraphs summarize the key findings of the various chapters in this dissertation. Together, these findings are this author's contribution to the field, the implementation and testing of a pMC algorithm with several unique features:

(1) This pMC implementation provides estimates of linearly polarized reflectance resulting from linearly polarized incident light.

(2) That pMC implementation accounts for phase function perturbations.

(3) This pMC implementation integrates a model that connects scattering interactions with specific scatterer groups to reflectance estimates.

Researchers have shown interest in recent years in utilizing polarized light sources in early detection of dysplasia or tissue changes and other researchers have also explored using phase function other than the Henyey-Greenstein phase function in order to more accurately model light-tissue interactions. Researchers interested in detecting dysplasia also lack models that explain how changes in subcellular structures affect reflectance spectra. It is the author's hope that these unique features are attractive and useful to other researchers in the field and will facilitate interesting findings regarding dysplasia or cancer detection.

Bibliography

[1] S. Bartel and A. Hielscher. Monte carlo simulations of the diffuse backscattering mueller matrix for highly scattering media. *Appl. Opt.*, 39(10):1580–1588, 2000.

[2] M. Bartlett, G. Huang, L. Larcom, and H. Jiang. Measurement of particle size distribution in mammalian cells in vitro by use of polarized light spectroscopy. *Appl. Opt.*, 43(6):1296–1307, 2004.

[3] C. F. Bohren and D. R. Huffman. *Absorption and scattering of light by small particles*. John Wiley & Sons, 2008.

[4] F. B. Brown, R. Barrett, T. Booth, J. Bull, L. Cox, R. Forster, T. Goorley, R. Mosteller, S. Post, R. Prael, et al. *MCNP version 5*, 2002.

[5] M. Canpolat and J. Mourant. Particle size analysis of turbid media with a single optical fiber in contact with the medium to deliver and detect white light. *Appl. Opt.*, 40(22):3792–3799, 2001.

[6] J. Chen and X. Intes. Time-gated perturbation monte carlo for whole body functional imaging in small animals. *Opt. Express*, 17(22):19566–19579, 2009.

[7] J. Chen and X. Intes. Comparison of monte carlo methods for fluorescence molecular tomography - computational efficiency. *Med. Phys.*, 38(10):5788–5798, 2011.

[8] H. W. Engl, M. Hanke, and A. Neubauer. *Regularization of inverse problems*, volume 375. Springer Science & Business Media, 1996.

[9] A. Gomes, S. Ruderman, M. DelaCruz, R. Wali, H. Roy, and V. Backman. In vivo measurement of the shape of the Tissue-Refractive-Index correlation function and its application to detection of colorectal field carcinogenesis. *J. Biomed. Opt.*, 17(4), 2012.

[10] A. Gomes, V. Turzhitsky, S. Ruderman, and V. Backman. Monte carlo model of the penetration depth for polarization gating spectroscopy: Influence of Illumination-Collection geometry and sample optical properties. *Appl. Opt.*, 51(20), 2012.

[11] C. Hayakawa, J. Spanier, F. Bevilacqua, A. Dunn, J. You, B. Tromberg, and V. Venugopalan. Perturbation monte carlo methods to solve inverse photon migration problems in heterogeneous tissues. *Opt. Lett.*, 26(17):1335–1337, 2001.

[12] C. K. Hayakawa. *Perturbation Monte Carlo Methods for the Solution of Inverse Problems*. PhD thesis, Claremont Graduate University, 2002.

[13] C. K. Hayakawa, V. Sankaran, F. Bevilacqua, J. Spanier, and V. Venugopalan. Use of perturbation and differential monte carlo methods to solve inverse problems in heterogeneous media. In *Biomedical Topical Meeting*, page FH24, 2004.

[14] C. K. Hayakawa, J. Spanier, and V. Venugopalan. Comparative analysis of discrete and continuous absorption weighting estimators used in monte carlo simulations of radiative transport in turbid media. *JOSA A*, 31(2):301–311, 2014.

[15] J. Heiskala, K. Kotilahti, L. Lipiäinen, P. Hiltunen, P. E. Grant, and I. Nissilä. Optical tomographic imaging of activation of the infant auditory cortex using perturbation monte carlo with anatomical a priori information. In *Diffuse Optical Imaging of Tissue*. Optical Society of America, 2007.

[16] T. Johnson and J. Mourant. Polarized wavelength-dependent measurements of turbid media. *Optics express*, 4(6):200–216, 1999.

[17] L. Kudryavtsev. Fubini theorem. *Encyclopedia of Mathematics, Springer*, 2001.

[18] J. Mourant, T. Johnson, S. Carpenter, A. Guerra, T. Aida, and J. Freyer. Polarized angular dependent spectroscopy of epithelial cells and epithelial cell nuclei to determine the size scale of scattering structures. *J. Biomed. Opt.*, 7(3), 2002.

[19] J. R. Mourant, T. J. Bocklage, T. M. Powers, H. M. Greene, K. L. Bullock, L. R. Marr-Lyon, M. H. Dorin, A. G. Waxman, M. M. Zsemlye, and H. O. Smith. In vivo light scattering measurements for detection of precancerous conditions of the cervix. *Gynecologic oncology*, 105(2):439–445, 2007.

[20] J. R. Mourant, J. P. Freyer, A. H. Hielscher, A. A. Eick, D. Shen, and T. M. Johnson. Mechanisms of light scattering from biological cells relevant to noninvasive optical-tissue diagnostics. *Appl. Opt.*, 37(16):3586–3593, 1 June 1998.

[21] J. R. Mourant, T. M. Johnson, and J. P. Freyer. Characterizing mammalian cells and cell phantoms by polarized backscattering fiber-optic measurements. *Applied Optics*, 40(28):5114–5123, 2001.

[22] J. R. Mourant, T. M. Powers, T. J. Bocklage, H. M. Greene, M. H. Dorin, A. G. Waxman, M. M. Zsemlye, and H. O. Smith. In vivo light scattering for the detection of cancerous and precancerous lesions of the cervix. *Applied optics*, 48(10):D26–D35, 2009.

[23] J. Nguyen, C. K. Hayakawa, J. R. Mourant, and J. Spanier. Perturbation monte carlo methods for tissue structure alterations. *Biomed. Opt. Express*, 4(10):1946–1963, 2013.

[24] L. Nieman, A. Myakov, J. Aaron, and K. Sokolov. Optical sectioning using a fiber probe with an angled Illumination-Collection geometry: Evaluation in engineered tissue phantoms. *Appl. Opt.*, 43(6):550–555, 2004.

[25] J. Ramachandran, T. Powers, S. Carpenter, A. Garcia-Lopez, J. Freyer, and J. Mourant. Light scattering and microarchitectural differences between tumorigenic and Non-Tumorigenic cell models of tissue. *Opt. Express*, 15(7), 2007.

[26] J. Ramella-Roman, S. Prahl, and S. Jacques. Three monte carlo programs of polarized light transport into scattering media: part I. *Opt. Express*, 13(12):4420–4438, 2005.

[27] J. M. Schmitt and G. Kumar. Turbulent nature of refractive-index variations in biological tissue. *Opt. Lett.*, 21(16):1310–1312, 1996.

[28] J. M. Schmitt and G. Kumar. Optical scattering properties of soft tissue: a discrete particle model. *Appl. Opt.*, 37(13):2788–2797, 1 May 1998.

[29] I. Seo, J. You, C. Hayakawa, and V. Venugopalan. Perturbation and differential monte carlo methods for measurement of optical properties in a layered epithelial tissue model. *J. Biomed. Opt.*, 12(1), 2007.

[30] J. Spanier. Some results on transport theory and their application to monte carlo methods. *Journal of Mathematical Analysis and Applications*, 17(3):549–559, 1967.

[31] J. Spanier and E. Gelbard. *Monte Carlo Principles and Neutron Transport Problems*. Addison-Wesley, 1969.

[32] H. Subramanian, P. Pradhan, Y. Liu, I. Capoglu, X. Li, J. Rogers, A. Heifetz, D. Kunte, H. Roy, A. Taflove, and V. Backman. Optical methodology for detecting histologically unapparent nanoscale consequences of genetic alterations in biological cells. *Proceedings of the National Academy of Sciences*, 105(51), 2008.

[33] H. Subramanian, H. Roy, P. Pradhan, M. Goldberg, J. Muldoon, R. Brand, C. Sturgis, T. Hensing, D. Ray, A. Bogojevic, J. Mohammed, J. Chang, and V. Backman. Nanoscale cellular changes in field carcinogenesis detected by partial wave spectroscopy. *Cancer Res.*, 69(1):5357–5363, 2009.

[34] N. Terry, Y. Zhu, J. K. M. Thacker, J. Migaly, C. Guy, C. R. Mantyh, and A. Wax. Detection of intestinal dysplasia using angle-resolved low coherence interferometry. *J. Biomed. Opt.*, 16(10):106002, Oct. 2011.

[35] P. Yalavarthy, K. Karlekar, H. Patel, R. Vasu, M. Pramanik, P. Mathias, B. Jain, and P. Gupta. Experimental investigation of perturbation Monte-Carlo based derivative estimation for imaging Low-Scattering tissue. *Opt. Express*, 13(3):985–997, 2005.

[36] Y. Zhu, N. Terry, J. Woosley, N. Shaheen, and A. Wax. Design and validation of an Angle-Resolved Low-Coherence interferometry fiber probe for for in vivo clinical measurements of Depth-Resolved nuclear morphology. *J. Biomed. Opt.*, 16(1), 2011.

Appendix A

Proofs

A.1 Equivalence Proof for Scattering Algorithms

A.1.1 Scattering algorithms

Two distinct scattering algorithms were considered for this study: the Composite Phase Function Scattering Method and the Distribution Selection Scattering Method. We will briefly explain the algorithm behind each of these methods and show that these algorithms produce equivalent distributions of scattering angles. We chose DSSM in this paper because the derivative of the resulting estimator is computationally simple to obtain. The Composite Phase Function Scattering Method used in [23] constructs a composite phase function by calculating the weighted average of the phase functions of each distribution of scatterers, where the weights are based on each distribution's contribution to the scattering coefficient

$$\overline{f} = \sum_{i=1}^{m} \frac{\mu_{s,i}}{\overline{\mu}_s} f_i \tag{A.1}$$

where $\overline{f}$ is the composite phase function, f_i is the phase function of the ith distribution, $\mu_{s,i}$ is ith scatterer distribution's contribution to the scattering coefficient and $\overline{\mu}_s$ is the scattering coefficient of the entire medium and is the sum of the scattering coefficient contributions of all distributions.

The Distribution Selection Scattering Method used in this study, calculates the probability of interacting separately with each of the scatterer distributions. The probability of interacting with the ith scattering distribution is proportional to that distribution's contribution to the scattering coefficient, i.e., $P(Y = i) = \mu_{s,i}/\overline{\mu}_s$, where Y is a random variable that selects the population for the scattering event. Given that the photon must interact with the ith scattering distribution, the phase function of the ith scattering distribution, f_i, is then sampled for a scattering angle. The composite scattering phase function is not constructed in this method.

A.1.2 Proof of scattering algorithm equivalence

We will demonstrate equivalence between the Composite Phase Function Scattering Method and the Distribution Selection Scattering method by showing that both methods ultimately produce the same cumulative distribution function (CDF).

Consider a medium that has m groups of scatterers that each contribute to the medium's scattering coefficient. Recall that in the Distribution Selection Scattering Method, a distribution is randomly selected according to the percentage population of that scatterer to the total scatterer population. The variable Y is defined as a random discrete variable that selects the population for some scattering event and can take on integer values between 1 and m. The CDF of Y is

$$F_Y(y) = \begin{cases} 0, & y < 1 \\ \sum_{k=1}^{floor(y)} \frac{\mu_{s,k}}{\overline{\mu}_s}, & 1 \leq y \leq m \end{cases}. \tag{A.2}$$

Given that Y selects the ith distribution, its phase function will be used to select a polar scattering

angle θ. The conditional CDF of θ, given some value of Y is the CDF of that distribution's phase function

$$F_{\Theta Y}(\theta|Y=i) = \int f_i \sin\theta \mathrm{d}\theta. \tag{A.3}$$

Since the events that $Y=1$, $Y=2$, ..., $Y=m$ are disjoint, we can obtain the CDF for θ for DSSM through an application of Bayes' Theorem using the probabilities in Eq. (A.2) and the conditional CDF in Eq. (A.3)

$$F_{new}(\theta) = \sum_{i=1}^{m} F_{\Theta Y}(\theta|Y=i)P(Y=i) = \sum_{i=1}^{m} \int f_i \sin\theta \mathrm{d}\theta \left\{\frac{\mu_{s,i}}{\overline{\mu}_s}\right\} = \int \sum_{i=1}^{m} f_i \sin\theta \mathrm{d}\theta \left\{\frac{\mu_{s,i}}{\overline{\mu}_s}\right\}. \tag{A.4}$$

In the last step above, we reverse the order of the summation and the integral so that Eq. (A.4) will more closely resemble Eq. (A.5). We invoke Tonelli's theorem, which states that if $f_n(x) \geq 0$ then $\sum \int f_n(x)\mathrm{d}x = \int \sum f_n(x)\mathrm{d}x$ [17]. In our case, the expressions inside of the summation and the integral in Eq. (A.4) involve a probability density function and the sine of the scattering angle, both of which may take on values greater than or equal to zero, so reversal of integration and summation operations are valid. In the Composite Phase Function Scattering Method, each distribution's phase function is calculated, and then the phase functions are weighted according to that distribution's scattering coefficient and a composite phase function is then created. This was mentioned previously in Eq. (A.1). Next, a CDF is then constructed from the composite phase function. Substituting in Eq. (A.1), yields:

$$F(\theta) = \int \overline{f} \sin\theta \mathrm{d}\theta = \int \sum_{i=1}^{m} \frac{\mu_{s,i}}{\overline{\mu}_s} f_i \sin\theta \mathrm{d}\theta. \tag{A.5}$$

This demonstrates that the Composite Phase Function Scattering Method and the Distribution Selection Scattering Method both produce the same CDF since Eq. (A.4) and Eq. (A.5) are equivalent to one another.

Bibliography

[1] S. Bartel and A. Hielscher. Monte carlo simulations of the diffuse backscattering mueller matrix for highly scattering media. *Appl. Opt.*, 39(10):1580–1588, 2000.

[2] M. Bartlett, G. Huang, L. Larcom, and H. Jiang. Measurement of particle size distribution in mammalian cells in vitro by use of polarized light spectroscopy. *Appl. Opt.*, 43(6):1296–1307, 2004.

[3] C. F. Bohren and D. R. Huffman. *Absorption and scattering of light by small particles*. John Wiley & Sons, 2008.

[4] F. B. Brown, R. Barrett, T. Booth, J. Bull, L. Cox, R. Forster, T. Goorley, R. Mosteller, S. Post, R. Prael, et al. *MCNP version 5*, 2002.

[5] M. Canpolat and J. Mourant. Particle size analysis of turbid media with a single optical fiber in contact with the medium to deliver and detect white light. *Appl. Opt.*, 40(22):3792–3799, 2001.

[6] J. Chen and X. Intes. Time-gated perturbation monte carlo for whole body functional imaging in small animals. *Opt. Express*, 17(22):19566–19579, 2009.

[7] J. Chen and X. Intes. Comparison of monte carlo methods for fluorescence molecular tomography - computational efficiency. *Med. Phys.*, 38(10):5788–5798, 2011.

[8] H. W. Engl, M. Hanke, and A. Neubauer. *Regularization of inverse problems*, volume 375. Springer Science & Business Media, 1996.

[9] A. Gomes, S. Ruderman, M. DelaCruz, R. Wali, H. Roy, and V. Backman. In vivo measurement of the shape of the Tissue-Refractive-Index correlation function and its application to detection of colorectal field carcinogenesis. *J. Biomed. Opt.*, 17(4), 2012.

[10] A. Gomes, V. Turzhitsky, S. Ruderman, and V. Backman. Monte carlo model of the penetration depth for polarization gating spectroscopy: Influence of Illumination-Collection geometry and sample optical properties. *Appl. Opt.*, 51(20), 2012.

[11] C. Hayakawa, J. Spanier, F. Bevilacqua, A. Dunn, J. You, B. Tromberg, and V. Venugopalan. Perturbation monte carlo methods to solve inverse photon migration problems in heterogeneous tissues. *Opt. Lett.*, 26(17):1335–1337, 2001.

[12] C. K. Hayakawa. *Perturbation Monte Carlo Methods for the Solution of Inverse Problems*. PhD thesis, Claremont Graduate University, 2002.

[13] C. K. Hayakawa, V. Sankaran, F. Bevilacqua, J. Spanier, and V. Venugopalan. Use of perturbation and differential monte carlo methods to solve inverse problems in heterogeneous media. In *Biomedical Topical Meeting*, page FH24, 2004.

[14] C. K. Hayakawa, J. Spanier, and V. Venugopalan. Comparative analysis of discrete and continuous absorption weighting estimators used in monte carlo simulations of radiative transport in turbid media. *JOSA A*, 31(2):301–311, 2014.

[15] J. Heiskala, K. Kotilahti, L. Lipiäinen, P. Hiltunen, P. E. Grant, and I. Nissilä. Optical tomographic imaging of activation of the infant auditory cortex using perturbation monte carlo with anatomical a priori information. In *Diffuse Optical Imaging of Tissue*. Optical Society of America, 2007.

[16] T. Johnson and J. Mourant. Polarized wavelength-dependent measurements of turbid media. *Optics express*, 4(6):200–216, 1999.

[17] L. Kudryavtsev. Fubini theorem. *Encyclopedia of Mathematics, Springer*, 2001.

[18] J. Mourant, T. Johnson, S. Carpenter, A. Guerra, T. Aida, and J. Freyer. Polarized angular dependent spectroscopy of epithelial cells and epithelial cell nuclei to determine the size scale of scattering structures. *J. Biomed. Opt.*, 7(3), 2002.

[19] J. R. Mourant, T. J. Bocklage, T. M. Powers, H. M. Greene, K. L. Bullock, L. R. Marr-Lyon, M. H. Dorin, A. G. Waxman, M. M. Zsemlye, and H. O. Smith. In vivo light scattering measurements for detection of precancerous conditions of the cervix. *Gynecologic oncology*, 105(2):439–445, 2007.

[20] J. R. Mourant, J. P. Freyer, A. H. Hielscher, A. A. Eick, D. Shen, and T. M. Johnson. Mechanisms of light scattering from biological cells relevant to noninvasive optical-tissue diagnostics. *Appl. Opt.*, 37(16):3586–3593, 1 June 1998.

[21] J. R. Mourant, T. M. Johnson, and J. P. Freyer. Characterizing mammalian cells and cell phantoms by polarized backscattering fiber-optic measurements. *Applied Optics*, 40(28):5114–5123, 2001.

[22] J. R. Mourant, T. M. Powers, T. J. Bocklage, H. M. Greene, M. H. Dorin, A. G. Waxman, M. M. Zsemlye, and H. O. Smith. In vivo light scattering for the detection of cancerous and precancerous lesions of the cervix. *Applied optics*, 48(10):D26–D35, 2009.

[23] J. Nguyen, C. K. Hayakawa, J. R. Mourant, and J. Spanier. Perturbation monte carlo methods for tissue structure alterations. *Biomed. Opt. Express*, 4(10):1946–1963, 2013.

[24] L. Nieman, A. Myakov, J. Aaron, and K. Sokolov. Optical sectioning using a fiber probe with an angled Illumination-Collection geometry: Evaluation in engineered tissue phantoms. *Appl. Opt.*, 43(6):550–555, 2004.

[25] J. Ramachandran, T. Powers, S. Carpenter, A. Garcia-Lopez, J. Freyer, and J. Mourant. Light scattering and microarchitectural differences between tumorigenic and Non-Tumorigenic cell models of tissue. *Opt. Express*, 15(7), 2007.

[26] J. Ramella-Roman, S. Prahl, and S. Jacques. Three monte carlo programs of polarized light transport into scattering media: part I. *Opt. Express*, 13(12):4420–4438, 2005.

[27] J. M. Schmitt and G. Kumar. Turbulent nature of refractive-index variations in biological tissue. *Opt. Lett.*, 21(16):1310–1312, 1996.

[28] J. M. Schmitt and G. Kumar. Optical scattering properties of soft tissue: a discrete particle model. *Appl. Opt.*, 37(13):2788–2797, 1 May 1998.

[29] I. Seo, J. You, C. Hayakawa, and V. Venugopalan. Perturbation and differential monte carlo methods for measurement of optical properties in a layered epithelial tissue model. *J. Biomed. Opt.*, 12(1), 2007.

[30] J. Spanier. Some results on transport theory and their application to monte carlo methods. *Journal of Mathematical Analysis and Applications*, 17(3):549–559, 1967.

[31] J. Spanier and E. Gelbard. *Monte Carlo Principles and Neutron Transport Problems*. Addison-Wesley, 1969.

[32] H. Subramanian, P. Pradhan, Y. Liu, I. Capoglu, X. Li, J. Rogers, A. Heifetz, D. Kunte, H. Roy, A. Taflove, and V. Backman. Optical methodology for detecting histologically unapparent nanoscale consequences of genetic alterations in biological cells. *Proceedings of the National Academy of Sciences*, 105(51), 2008.

[33] H. Subramanian, H. Roy, P. Pradhan, M. Goldberg, J. Muldoon, R. Brand, C. Sturgis, T. Hensing, D. Ray, A. Bogojevic, J. Mohammed, J. Chang, and V. Backman. Nanoscale cellular changes in field carcinogenesis detected by partial wave spectroscopy. *Cancer Res.*, 69(1):5357–5363, 2009.

[34] N. Terry, Y. Zhu, J. K. M. Thacker, J. Migaly, C. Guy, C. R. Mantyh, and A. Wax. Detection of intestinal dysplasia using angle-resolved low coherence interferometry. *J. Biomed. Opt.*, 16(10):106002, Oct. 2011.

[35] P. Yalavarthy, K. Karlekar, H. Patel, R. Vasu, M. Pramanik, P. Mathias, B. Jain, and P. Gupta. Experimental investigation of perturbation Monte-Carlo based derivative estimation for imaging Low-Scattering tissue. *Opt. Express*, 13(3):985–997, 2005.

[36] Y. Zhu, N. Terry, J. Woosley, N. Shaheen, and A. Wax. Design and validation of an Angle-Resolved Low-Coherence interferometry fiber probe for for in vivo clinical measurements of Depth-Resolved nuclear morphology. *J. Biomed. Opt.*, 16(1), 2011.